INVESTIGATION OF TRANSITION FLOW OVER S809 AIRFOIL USING INFRARED THERMOGRAPHY AND NUMERICAL METHODS

S809 KANAT KESİTİ ÜZERİNDEKİ GEÇİŞ AKIŞININ KIZILÖTESİ TERMOGRAFİ VE SAYISAL YÖNTEMLERLE İNCELENMESİ

NECLA ECENAZ AYKUT

PROF. DR. MURAT KÖKSAL

Supervisor

Submitted to

Graduate School of Science and Engineering of Hacettepe University

As a Partial Fulfillment to the Requirements for the Award of the Degree of Master of Science in Mechanical Engineering

June 2023

To my great aunt Nüket Solmaz AYKUT

ABSTRACT

INVESTIGATION OF TRANSITION FLOW OVER S809 AIRFOIL USING INFRARED THERMOGRAPHY AND NUMERICAL METHODS

Necla Ecenaz AYKUT

Master of Science, Mechanical Engineering
Supervisor: Prof. Dr. Murat KÖKSAL

June 2023, 97 pages

This thesis presents the results of an experimental and numerical study that investigates the detection of boundary layer transitional flow using infrared thermography and Computational Fluid Dynamics analysis.

The experimental part of this thesis involves wind tunnel experiments conducted in METUWIND large-scale multi-purpose wind tunnel. S809 laminar airfoil was used as a test object and experiments were conducted in the boundary layer test section (TS2) of METUWIND. Experiments were performed for different Reynolds numbers at 0° angle of attack and different angles of attack at a Reynolds number of 5×10^5. Thus, separate effects of Reynolds number and angle of attack on the variation of the separation, transition onset, and reattachment points on the chordwise position of the airfoil were

examined. In addition, the effect transition strip was observed experimentally using a vortex generator.

In the numerical part of the thesis, CFD simulations of the experimental cases were carried out. Effects of different turbulence transition models ($k-\omega-\gamma$ transition model, transition $k-kl-\omega$ model and transition SST model) were examined and implemented to the cases of the thesis using a commercial software. Afterwards, transition models were compared among themselves and with the standard $k-\varepsilon$ turbulence model to highlight the difference.

The experimental process and results were compared and discussed with the results of numerical methods. The chordwise positions of the separation, transition, and reattachment points were successfully determined using the IR thermography method and CFD analyses, and the results were consistent. As the Reynolds number changes within the range of 5×10^5, 6×10^5 and 7×10^5 for 0° angle of attack, the chordwise position of the transition onset point did not show significant variations because of the low variation of the Reynolds number. As the angle of attach changes within the range of 0°, 3°, 6° and 9° for 5×10^5 Reynolds number, the chordwise position of the transition onset point approached the leading edge of the airfoil.

Keywords: Boundary Layer Transition Flow, Separation Bubble, Infrared Thermography, Wind Tunnel Testing, Laminar Airfoil, Computational Fluid Dynamics

ÖZET

S809 KANAT KESİTİ ÜZERİNDEKİ GEÇİŞ AKIŞININ KIZILÖTESİ TERMOGRAFİ VE SAYISAL YÖNTEMLERLE İNCELENMESİ

Necla Ecenaz AYKUT

Yüksek Lisans, Makina Mühendisliği
Danışman: Prof. Dr. Murat KÖKSAL

Haziran 2023, 97 sayfa

Bu tez, kızılötesi termografi ve hesaplamalı akışkanlar dinamiği (HAD) analizi kullanarak sınır tabaka geçiş akışının tespitini inceleyen deneysel ve sayısal bir çalışmanın sonuçlarını sunmaktadır.

Tezin deneysel bölümü, RÜZGEM büyük ölçekli çok amaçlı rüzgar tünelinde gerçekleştirilen rüzgar tüneli testlerini içermektedir. Test objesi olarak S809 laminar kanadı kullanılmış ve deneyler RÜZGEM sınır tabaka test kesiti (TK2) içinde gerçekleştirilmiştir. Deneyler, sabit 0° hücum açısında farklı Reynolds sayıları ve sabit 5×10^5 Reynolds sayısında farklı hücum açıları için yapılmıştır. Böylece Reynolds sayısı ve hücum açısının sınır tabaka ayrılması, geşiç akışı başlangıcı ve akışın yeniden bağlanma noktalarının kanat kirişi üzerindeki konumunun değişimine etkisi

incelenmiştir. Ayrıca, kanat modeline geçiş şeridi eklenerek deneysel olarak etkisi gözlemlenmiştir.

Tezin sayısal bölümünde, deneysel durumların HAD simulasyonları gerçekleştirilmiştir. Farklı türbülansa geçiş modellerinin ($k-\omega-\gamma$ geçiş modeli, geçiş $k-kl-\omega$ modeli ve geçiş SST modeli) etkileri incelenmiş ve ticari bir yazılım kullanılarak deney koşullarna uygulanmıştır. Ardından, geçiş modelleri birbirleriyle ve $k-\varepsilon$ türbülans modeliyle karşılaştırılmış ve farklar vurgulanmıştır.

Deneysel süreç ve sonuçlar, sayısal yöntemlerin sonuçlarıyla karşılaştırılarak tartışılmıştır. Ayrılma, geçiş akışı başlangıcı ve yeniden bağlanma noktalarının kanat kirişi boyunca konumları, IR termografi yöntemi ve CFD analizleri kullanılarak başarılı bir şekilde belirlenmiş ve sonuçlar tutarlı çıkmıştır. Reynolds sayısı 5×10^5, 6×10^5, 7×10^5 aralığında değiştiğinde 0° hücum açısı için, geçiş akışı başlangıç noktasının kanat kirişi boyunca konumu önemli bir değişim göstermemiştir, çünkü Reynolds sayısının mertebesi çok yüksek değildi. Hücum açısı 0°, 3°, 6°, 9° aralığında değiştiğinde 5×10^5 Reynolds sayısı için, geçiş başlangıç noktasının kanat kirişi boyunca konumu kanadın ön kenarına yaklaşmıştır.

Anahtar Kelimeler: Sınır Tabaka Geçiş Akışı, Ayrılma Kabarcığı, Kızılötesi Termografi, Rüzgar Tüneli Testi, Laminer Kanat Profili, Hesaplamalı Akışkanlar Dinamiği

ACKNOWLEDGEMENT

I would like to express my deepest gratitude my supervisor Prof. Dr. Murat Köksal for his guidance, advice, criticism, encouragements and insight throughout the research. Having chance to work with him gave me better perspective and improved me academically.

The research is supported by METUWIND (Middle East Technical University, Center for Wind Energy Research). I want to emphasize my special thanks to Prof. Dr. Oğuz Uzol, director of METUWIND for allowing me perform the thesis study and providing resources. I would also like to thank all my colleagues at METUWIND for their valuable ideas, help and support.

My endless thanks go to my beloved love and best friend Remzi Erdem Barış, his support and sensible suggestions encouraged me to continue this study.

Last but not least, I am eternally indebted to my dear parents Şehnaz and Seylap Aykut for their endless love, faith, patience and support throughout my life. I would also express my love to my dear sister Selay Aykut.

TABLE OF CONTENTS

LIST OF FIGURES

LIST OF TABLES

LIST OF SYMBOLS

V_∞	Free-stream velocity [m/s]
ρ_∞	Free-stream density [kg/m^3]
T_∞	Tunnel temperature [°C]
P_{Static}	Tunnel static pressure [Pa]
μ	Dynamic viscosity [Pa.s]
ν	Kinematic viscosity [m^2/s]
α	Angle of attack [deg]
c	Chord length of airfoil (Characteristic length) [m]
x	Chordwise position of airfoil [m]
s	Span of airfoil [m]
d	Perpendicular distance between airfoil and infrared camera [m]
T	Chordwise temperature of airfoil [°C]
dT/dx	First derivative of chordwise temperature
C_f	Skin friction coefficient
Y+	Yplus value
γ	Gamma

LIST OF ABREVIATIONS

METUWIND	Middle East Technical University – Center for Wind Energy Research
LSWT	Large Scale Wind Tunnel
WT	Wind Tunnel
ATS	Aeronautical Test Section
BLTS	Boundary Layer Test Section
OJTS	Open Jet Test Section
TS	Test Section
IR	Infrared
LE	Leading Edge
TE	Trailing Edge
PIV	Particle Image Velocimetry
rpm	Revolutions per Minute
Re	Reynolds number based on tunnel inlet velocity and chord length of airfoil
Ma	Mach number
AoA	Angle of Attack
BL	Boundary Layer
BC	Boundary Condition
Tu	Turbulence Intensity
TKE	Turbulent Kinetic Energy
CFD	Computational Fluid Dynamics
2D	Two Dimension
NS	Navier-Stokes
RANS	Reynolds-avaraged Navier-Stokes

1. INTRODUCTION

1.1. Problem Definition

Transition is a complicated phenomenon, that includes the complete process of transitioning from laminar to turbulent flow. In other words, transitional flow is a mixture of laminar and turbulent flow. The transition from laminar to turbulent boundary layers has significant effects on viscous drag, heat transfer, and the onset of separation in aerodynamic flows. Consequently, the transition process holds great importance in the design and performance of various applications involving external flow applications.

Since separation can also occur in velocity regimes where transition flow occurs, examining this phenomenon have high importance for applications operated at low Reynolds number such as lightweight aircrafts, small scale wind turbines, small scale munitions and unmanned aerial vehicles.

Transition modelling is used to predict the transition from laminar to turbulent flows in fluids and to comprehend their impact on the overall solution. Simulating the interaction between laminar and turbulent flow is challenging due to the intricate nature and limited understanding of transitional flows.

This thesis was conducted to understand how the transition phenomenon occurs on a laminar separation bubble, and most importantly, to determine the separation, transition and reattachment points both experimentally and numerically.

1.2. Literature Survey

1.2.1. Fundamentals

In this section, first, the fundamental concepts of fluid mechanics, namely the boundary layer and shear stress, were discussed. Then, a detailed definition of boundary layer transition was provided.

Boundary Layer

The boundary layer refers to the thin layer of fluid that forms adjacent to a solid surface when a fluid flow over it. In aerodynamics, the boundary layer refers to the region of the flow where the fluid velocity changes from zero at the surface to the velocity of the free-

stream flow away from the surface. Boundary layer thickness can be affected by friction forces, heat transfer, separation, stall and turbulence. When the flow reaches a fully turbulent state, the complex nature of turbulence increases momentum, energy transport and mixing causing the boundary layer to expand perpendicular to the surface and the velocity distribution becomes more uniform as you move away from the wall. Besides, as the wall is approached, flow has steeper velocity gradients.

To compare laminar and turbulent boundary layers the presentation shown in Figure 1.1 can be used. The graph is obtained by normalizing the velocity profile by the boundary layer thickness δ and the outer or edge velocity of the external flow, V_e, i.e., by plotting u/V_e as a function of y/δ.

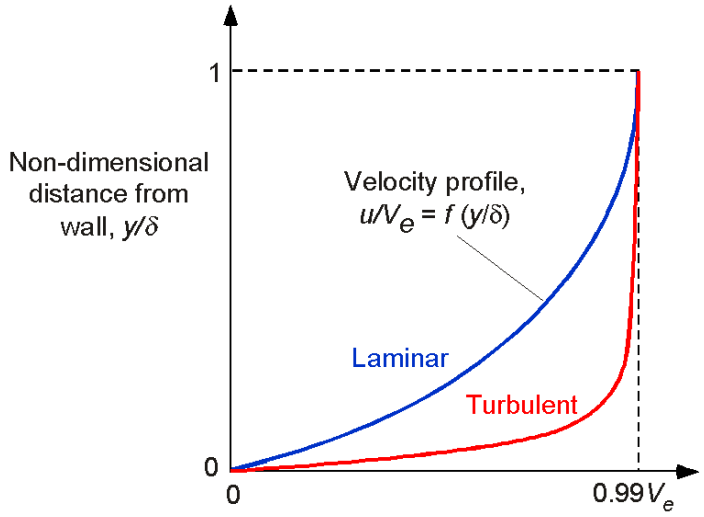

Figure 1.1. Normalized velocity profiles for laminar and turbulent boundary layers [52]

Shear Stress

Shear stress refers to the force per unit area that acts parallel to a surface, resulting from the sliding or deformation of adjacent layers of a fluid or material.

Viscous stresses are generated by the relative motion between neighboring fluid elements, resulting in a resistance that acts against the fluid's movement. The shear stress equation is shown below.

$$\tau = \mu\left(\frac{\partial u}{\partial y}\right) \tag{1.1}$$

The viscous shear stress, τ , is related to the absolute viscosity, μ , where ∂y is the rate at which the flow velocity increases (in the y direction) and is equivalent to a strain rate as shown Figure 1.2.

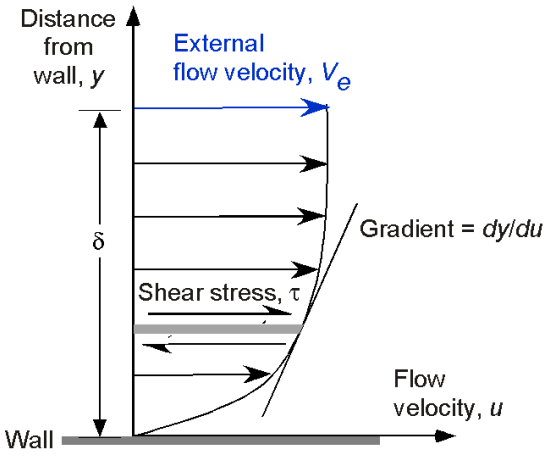

Figure 1.2. Boundary layer and shear stress [52]

If this equation is considered for a wall, the equation will be as below,

$$\tau_w = \mu \left(\frac{\partial u}{\partial y}\right) \quad \text{as} \quad y \to 0 \tag{1.2}$$

When shear stress is particularly interested for the wall, skin friction drag generated by the boundary layer on the surface can be computed. As described in the boundary layer section and shown in figure below, the turbulent boundary layer has high velocity gradient $\left(\frac{\partial u}{\partial y}\right)$. The higher gradients of velocity cause higher magnitude of wall shear stress of turbulent boundary layer will be greater compared to laminar boundary layer. This crucial phenomenon is starting point of this thesis.

Shear stress and skin friction are closely related concepts. The skin friction coefficient is a dimensionless parameter used to quantify the amount of drag or resistance experienced by a fluid flowing over a solid surface. It is defined as the ratio of the shear stress exerted on the surface to the dynamic pressure of the fluid.

The skin friction coefficient in aerodynamics is denoted as C_f and is defined as:

$$C_f = \frac{\tau_w}{0.5\rho V_\infty^2} \tag{1.3}$$

Transition Definition

In the 1880s, Osborne Reynolds discovered a criterion to distinguish between laminar and turbulent flow [6]. The dominant factor in this phenomenon is the balance between inertial and viscous forces in the fluid. This value is called the Reynolds Number. Inertial forces are reasons for motion in fluid and viscous forces are friction forces due to fluid viscosity.

$$\mathrm{Re} = \frac{\text{Inertial Forces}}{\text{Viscous Forces}} = \frac{\rho V c}{\mu} = \frac{V c}{\nu} \tag{1.4}$$

where ρ is the density of the fluid, V is the flow speed, c is a characteristic linear dimension, μ is the dynamic viscosity of the fluid, ν is the kinematic viscosity of the fluid.

Transition from laminar flow to turbulent flow can simply be defined as the process that transform from a regular (laminar) to a completely complex (turbulent) flow. Flow over a surface can be separated into two parts: the thin zone near the wall where viscous effects are high and the free flow zone away from the wall where viscous effects are less. The part with high viscous effects was defined by Ludwig Prandtl in 1904 and named as the boundary layer. The formation and growth of the boundary layer on a flat plate is shown schematically in Figure 1.3. The boundary layer initiates at the stagnation point located at the leading edge where the fluid initially contacts the surface. The fluid initially moves in a laminar state in the boundary layer. Then, instabilities begin to occur in the laminar boundary layer due to external effects such as free flow zone turbulence density, back pressure difference, surface curvature, surface roughness. These instabilities cause the regular flow to become turbulent, and this process is called transition.

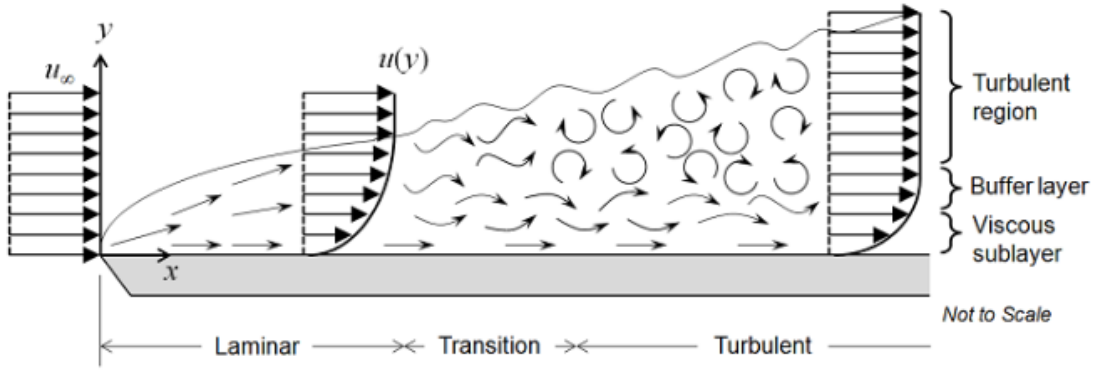

Figure 1.3. Transition of the laminar boundary layer into a fully turbulent boundary layer on a flat plate [17]

As seen in Figure 1.3, in the case of a smooth flat plate exposed to a uniform free stream, the transition process initiates at a critical Reynolds number, $Re_{x,critical}$ is approximately 5×10^5 for external flow [1]. Reynolds number is also used to obtain similar flows in order to perform experiment with the scaled down model in the wind tunnel.

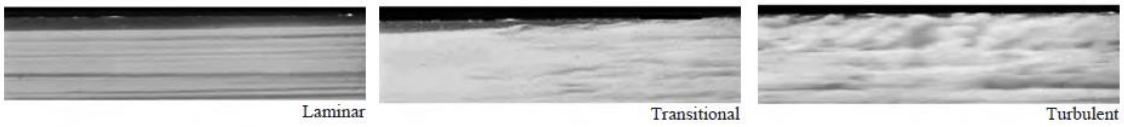

Figure 1.4. Laminar, transitional and turbulent flows [1]

In Figure 1.4, initially, the flow regime is laminar, characterized by smooth streamlines and highly organized motion. Then, it becomes turbulent with velocity fluctuations and chaotic motion. The transition from laminar to turbulent flow is not abrupt but happens gradually within a region where the flow changes between laminar and turbulent before reaching fully turbulent [1].

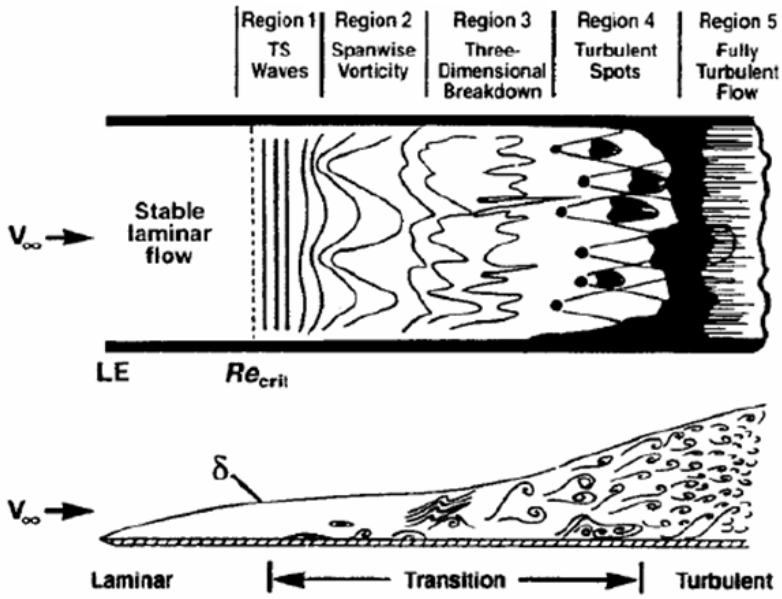

Figure 1.5. The natural transition process [8]

In this thesis, two fundamental transition processes have been discussed, namely natural and separation-induced transition processes. In Figure 1.5, natural transition process represented. The natural transition is one of the transition mechanisms This mode occurs when there is no adverse pressure gradient in flow and the transition occurs only because

of instabilities in the boundary layer. In region 1, Tollmien–Schlichting waves begin to form. T-S wave is a streamwise unstable wave which appears in a bounded shear flow such as boundary layer and channel flow. In region 2, spanwise vorticity begins to form and in region 3 three-dimensional vortex breakdown starts. In region 4, turbulent spots and edge contamination start. Finally, in region 5 flow becomes fully turbulent.

Another transition mechanism is separation induced transition. In this mode, if reattachment occurs, it is named as laminar separation bubble with transition. In this phenomenon, the adverse pressure gradient causes laminar flow to separate from the surface and because of instabilities in the boundary layer, the transition occurs. In this point, with the enough momentum against to adverse pressure gradient, flow can reattach. Figure 1.6 is a representation of separation, transition and reattachment points with streamlines.

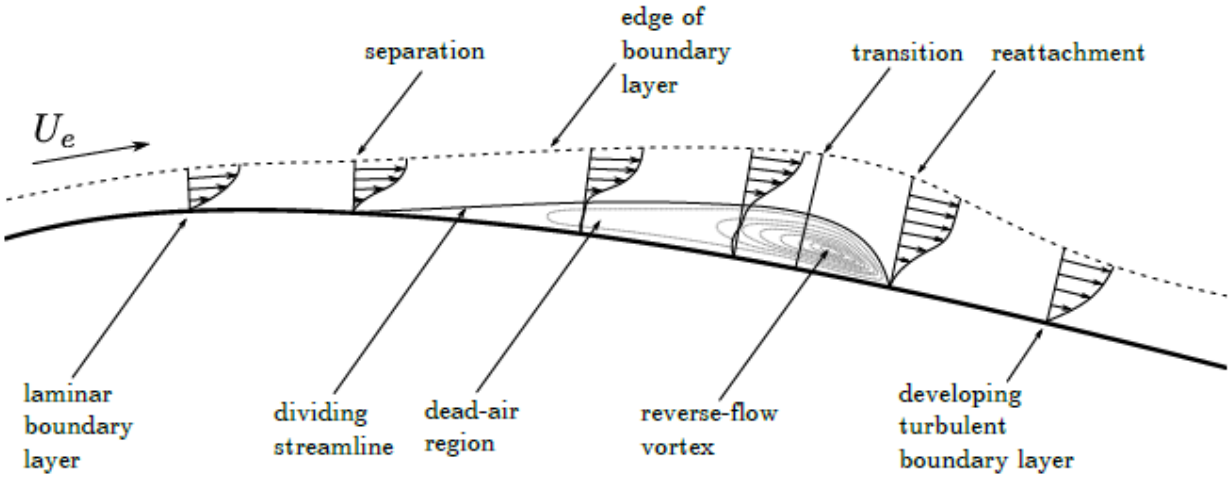

Figure 1.6. General characteristics of a laminar separation bubble and transition induced by separation [18]

As shown in Figure 1.7, a laminar separation bubble can be formed on the surface, resulting in the flow reattachment. If the flow does not reattach to the wing surface, it will remain in a stall state, which is not desirable because it significantly reduces aerodynamic performance by decreasing the lift and increasing the drag. For this reason, it is important to be able to specify the separation bubble and transition location for certain conditions.

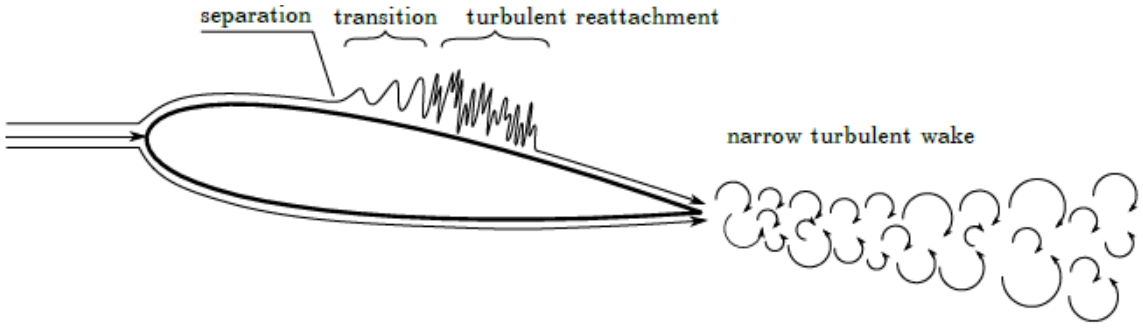

Figure 1.7. Separated shear layer forming separation bubble [18]

1.2.2. Experimental Studies on Boundary Layer Transition

Boundary layer transition flow can be detected experimentally by using different methods. Particle image velocimetry [9], force measurements, oil visualizations [5], high-frequency microphone measurements [7], hot-wire anemometry and infrared thermography [4] are some of these experimental methods.

The principle of identifying the character of the boundary layer using high-resolution infrared thermography is a technique widely used in many fields of research and has been used since the 1960s [19]. The following IR image examples show the capabilities of the IR imaging technique, views of the transition flow pattern on the airfoil, under certain test conditions. In Figure 1.8, the effect of the turbulent wedge which is a kind of surface roughness, provides early turbulent flow on the wing, is clearly seen. In Figure 1.9, the transition flow is shown due to laminar separation, where the bubble is represented by the colder (darker) straight strip between the laminar (dark) and turbulent (light) areas.

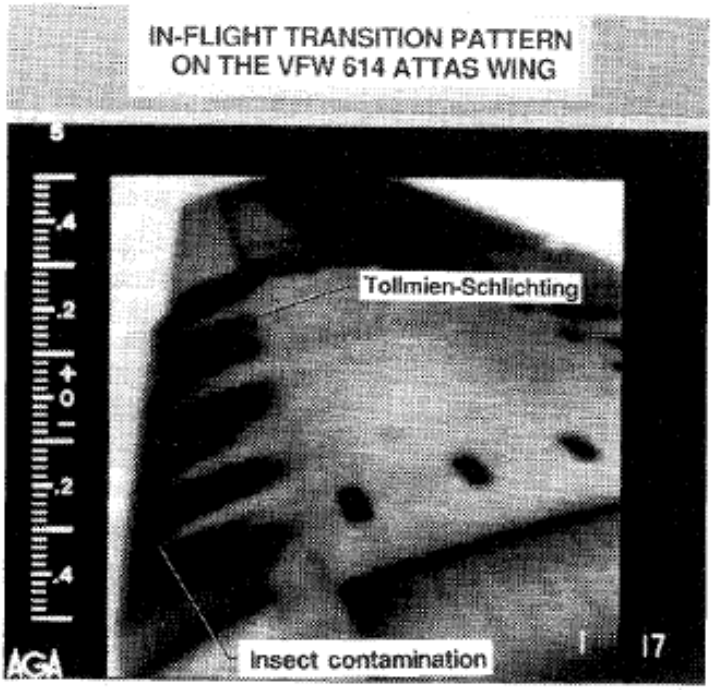

Figure 1.8. Tollmien-Schlichting waves and turbulent wedges [19]

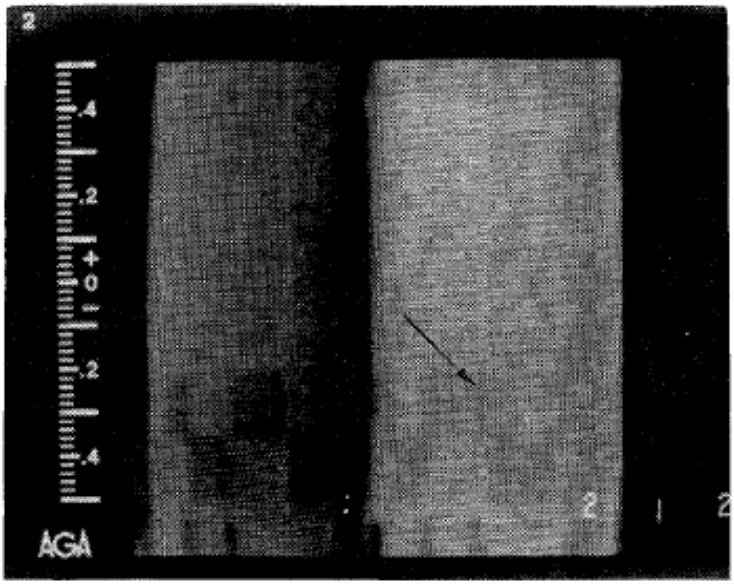

Figure 1.9. Transition via laminar separation bubble [19]

Jelinek examined the detectability of both turbulent transition and boundary layer separation by scanning infrared radiation [4]. The increased heat transfer in turbulent flow compared to laminar flow results in a change in the surface temperature of the model. This requires that the fluid and the surface of the model have different temperatures.

The underlying principle of using infrared thermography to detect the transition from laminar to turbulent boundary layer is based on the disparity in convection coefficient of heat transfer between these two flow regimes, leading to temperature difference.

The laminar boundary layer allows relatively less heat transfer between the ambient air and the surface of the model. In addition to this, in the turbulent boundary layer, the vorticity of the flow increases and so does the heat transfer between the ambient flow and the surface of the model. This causes the temperature of the model surface to change. The surface temperature approaches the temperature of the flow. Because of this phenomenon, the transition region can be recognized as an area of steep temperature change between two areas with different temperatures. The direction of the temperature change depends on whether the model is warmer than the ambient air or vice versa. The greater the difference between the temperature of the model and the flow, the more distinct the area of transition.

Infrared thermography for detecting turbulent boundary layers is a temperature measurement technique that relies on forced thermal convection occurring on the surface of the model under investigation.

In the literature, temperature and derivative of temperature with respect to the position in the streamwise direction were used to obtain numerical data from IR images. Skin friction is an important value for finding transition, separation and reattachment regions. Skin friction coefficient cannot be obtained in infrared tests directly. However, a relationship between local skin friction coefficient, $C_{f,x}$ and local Nusselt number, Nu_x can be obtained using the well-known Reynolds analogy [16]:

$$C_{f,x}\frac{Re_x}{2} = Nu_x = \frac{h_x x}{k} \tag{1.5}$$

The Nusselt number is a dimensionless number used in heat transfer analysis to determine the convective heat transfer coefficient. It relates the convective heat transfer rate to the conductive heat transfer rate across a solid boundary.

The following assumptions are made in Reynolds analogy; for a flat plate parallel to the incoming flow, $dp/dx = 0$ and there is no change in the free stream velocity outside the

boundary layer [16]. However, the Reynolds analogy approach can also be applied to airfoil geometries.

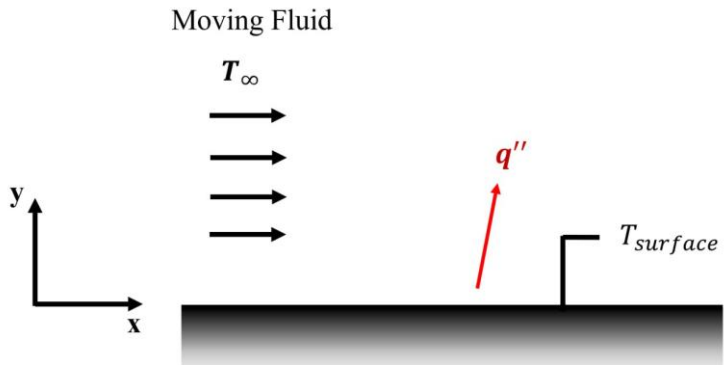

Figure 1.10. Convection from a surface to a moving fluid

As seen in Figure 1.10, for a given isothermal surface, the heat flux, q, can be calculated using the heat transfer coefficient h, the free stream temperature of the flow T_∞ and the model surface temperature $T_{surface}$:

$$q = h\left(T_{surface} - T_\infty\right) \tag{1.6}$$

where h is closely related to the friction coefficient C_f, the velocity of the flow V, thermal conductivity of fluid k and kinematic viscosity ν. For the heat transfer coefficient at any distance x the dependence is given by:

$$h(x) = {}^{1}/_{2} \,.\, C_f(x).V(x).{}^{k}/_{\nu} \tag{1.7}$$

Equation 1.6 is often referred to as Newton's cooling law, Equation 1.7 results from Reynolds analogy, which refers to heat transfer in the boundary layer when the value of the Prandtl number is close to one and without pressure gradient [16].

Based on the Reynolds analogy, a change in local skin friction coefficient when separation, transition or reattachment occur will also change the local convection heat transfer coefficient and hence the surface temperature.

$$q'' = h_x(T_x - T_\infty) = -k\frac{\partial T}{\partial y}(y = 0) \tag{1.8}$$

$$h_x = \frac{-k\frac{\partial T}{\partial y}(y=0)}{(T_x - T_\infty)} \tag{1.9}$$

Due to the reverse pressure gradient at the separation point, the velocity and hence the local Reynolds number suddenly decreases. There is a direct correlation between the Reynolds number and the Nusselt number which is the ratio between convective and conductive heat transfer at a fluid boundary. Since the dominant heat transfer mode is convection, there is a direct correlation between the Reynolds number and the convection heat transfer coefficient. According to Newton's law of cooling, the temperature gradient must rise in order to decrease the convection heat transfer coefficient. In other words, skin friction coefficient is inversely proportional to temperature gradient.

In general, C_f in a turbulent case is one order higher than in a laminar case. If the heat transfer from the model to the flow (in the case of a cooler flow and a warmer model surface) remains constant (e.g., through constant heating), the surface temperature of the model T_w will decrease with an increase in the skin friction coefficient (transition from laminar to turbulent flow). The resulting change in the model's surface temperature can then be quatified, for example, using an infrared camera and related to skin friction change using Reynolds analogy.

Table 1.1 provides a summary of experimental studies that detected transition using infrared thermography, followed by a detailed description of these studies.

Table 1.1. Experimental studies detecting transition using IR thermography

References / Specifications	Jelínek, 2018 [4]	Wynnychuk & Yarusevych, 2020 [9]	Marinus *et al.*, 2020 [5]
Airfoil	NACA 16-012	NACA 0018	NACA 16-409
Mach number	0.37, 0.58, 0.74, 0.82	-	0.1
Reynolds number	1000000 - 1400000	80000, 120000	330000
Angle of attack	0°	4°	0°,1°,2°,3°,4°, 5°,6°,7°,8°,9°

Transition strip	Thicknesses = 0.04, 0.08, 0.11 mm Ma = 0.4, 0.8	-	-
IR Camera	FLIR A655sc	Optris PI640	FLUKE Ti50
Validation method	CFD	PIV	CFD, XFOIL

Jelínek [4] used infrared thermography to observe boundary layer transition flow on a laminar airfoil (NACA 16-012). Since infrared thermography method does not cause any physical change or damage on test object, was preferred in this study. In aerodynamic wind tunnel experiments, triggering turbulence artificially becomes necessary by using roughness elements. In this study, the transition in the boundary layer was evoked with transition generator strips of various thicknesses at 0.4 and 0.8 Mach numbers. The ratio between the thickness of the transition generator and the thickness of the boundary layer displacement ranged from 0.42 to 1.25. The six cases with different thickness ratios of the transition generators were compared.

Five distinct regimes were observed for the gradually increasing Mach number: 0.37, 0.58, 0.74, 0.82 without a transition generator strip. From the results, it is obvious that the transition region of the boundary layer shifts toward the leading edge with increasing Mach number. With a transition generator strip (in the 35% of the chord); at low thicknesses, it was observed that the transition area gets shorter as the thickness increases. In high thicknesses, boundary layer separation occurs and following the separation bubble, there is a rapid transition to turbulence. When comparing the temperature profiles along the chord for each of the studied cases, there is a gradual increase in temperature observed from the leading edge up to the location of the transition generator strip. This corresponds to an increase in the laminar boundary layer thickness, which acts like an insulator and allows the surface to maintain its original temperature. The subsequent drop in temperature indicates the presence of the transition region within the boundary layer.

In this study [4], it is shown how the height of the transition generator can affect the boundary layer transition. The infrared thermography was used for such experiments at high subsonic and supersonic Mach numbers. The technique visualizes the transition region very well without surface influence.

Wynnychuk and Yarusevych [9] identified the laminar separation bubble for NACA 0018 airfoil using infrared thermography and PIV. Experiments were conducted for chord-based Reynolds numbers of 80000 and 120000 and at different angles of attack.

The analysis of surface temperature characteristics was employed to establish a methodology for diagnosing laminar separation bubbles based on surface temperature. In the case of convection-dominated surface cooling, the gradients of surface temperature in the flow direction indicate the mean detachment and transition points, which correspond to the maximum and minimum values, respectively. The mean reattachment point coincides with the location of the minimum surface temperature. The study shows that infrared thermography produces accurate and reliable results for boundary layer separation, transition and reattachment.

Marinus [5] investigated the characteristics of the cambered NACA 16-409 airfoil at low speeds by infrared thermography, oil visualization and force measurements. In the study, for subsonic airflow (Prandtl number is $Pr \approx 1$), heat and momentum transfer in the boundary layer was investigated in relation to Reynold's analogy.

As mentioned earlier, the skin friction coefficient and the heat transfer rate are directly linked through the convective heat transfer coefficient. As the boundary layer transitions to a more turbulent state, there is an increase in heat transfer, resulting in a lower wall temperature.

Experimental results were compared with RANS simulations with transitional SST, k-omega and gamma intermittency turbulence models. Three different flow patterns were identified varying on the angle of attack (AoA);

For 0° to 3° AoA, in laminar flow that separates early (between 75% and 80% of the chord), the dissociated shear layer becomes turbulent without reattaching to the surface.

For 3° to 5° AoA, the separated shear layer is transitional at 84%-chord, the reattached turbulent flow separates again 2% upstream of the trailing edge, while a laminar separation bubble covers roughly 73%- to 93%-chord.

For 5° to 9° AoA, the turbulent boundary layer would separate by about 90% of its chord, while a leading edge separation bubble didn't exist.

1.2.3. Numeric Modelling of Boundary Layer Transition

Besides experimental methods, there are several numerical transition models in engineering applications. Direct numerical simulations (DNS) provide highly accurate simulations of the transition to fully turbulent flow. DNS method is based on solving Navier-Stokes equations explicitly, but it is computationally expensive. Large eddy simulations (LES) involve the resolution of large-scale eddies while modeling the effects of small-scale eddies using an eddy viscosity approach. LES method has also large computational requirements [2].

The other method is based on the Reynolds Averaged Navier Stokes (RANS) equations. It is widely used for the last few decades due to its less computing requirement [11]. There are number of works shows that RANS-based models can predict transition with reasonable accuracy [12]. For turbulence modelling, several RANS based models can be used to detect transition phenomena. The Transition SST, Transition $k-kl-\omega$, $k-\omega-\gamma$ transition models are effective tools for simulating the transition of a boundary layer from a laminar to a turbulent regime [13], [14], [15]. More information about these models will be given in Section 3.

1.2. Objectives of the Thesis

In this thesis, it is aimed to investigate the boundary layer transition flow numerically and experimentally. The main goal of the study is to investigate the capability of infrared thermography as a means for accurate determination of the transition onset point in flows where boundary layer transition flow is important.

The specific objectives of the study are:

- To use the infrared thermography technique to determine the transition onset point on S809 laminar airfoil and investigate its performance,
- To carry out a CFD analysis of the transitional flow over S809 laminar airfoil using different transition turbulence models, and compare the results with the infrared measurements.

This study focuses on the investigation of transition flow occurring in the separation and reattachment regions of the boundary layer over the suction surface of a 2D model wing that has a S809 airfoil profile.

1.3. Thesis Outline

In this section, the problem statement of the thesis, fundamental concepts in fluid mechanics, experimental solutions using infrared thermography in the literature, and the objective of the thesis are provided.

Section 2 includes information about the wind tunnel, wing model, IR camera, experimental setup, pre-processing, conducting of the experiment, and post-processing, infrared thermography methodology, experimental uncertainty calculation, and repeatability analysis.

Section 3 provides the governing equations, assumptions, equations of the transition models, numerical methodology and mesh generation process in the CFD solution.

Section 4 consists of two main sections, which are the experimental and numerical results. In the experimental results, in addition to the outcomes of the test matrix cases, the results of the transition strip tests are also presented. Furthermore, the numerical results include the study of the turbulence and transition models, among other analyses.

Section 5 presents the conclusion of the thesis, including the final remarks and future recommendations.

2. EXPERIMENTAL STUDIES

2.1. Wind Tunnel

Wind tunnels describe the experimental setup used to test the interaction of objects with airflow. For example, performing flight testing in aircraft design can be complex and expensive, while wind tunnel testing can yield a lot of data necessary for design.

Wind tunnels are important institutions that contribute to the technology development of a country, especially in the field of aviation. The two most important wind tunnels are operating in Turkey, the Ankara Wind Tunnel and METUWIND.

Experiments were conducted in METUWIND large scale multi-purpose wind tunnel located in Middle East Technical University Ankara campus. The construction of METUWIND LSWT was completed in 2020, the purpose of the tunnel is to serve different fields such as defense industry, automotive, city planning and environment, civil sector and university. Figure 2.1 provides a general schematic of the METUWIND LSWT.

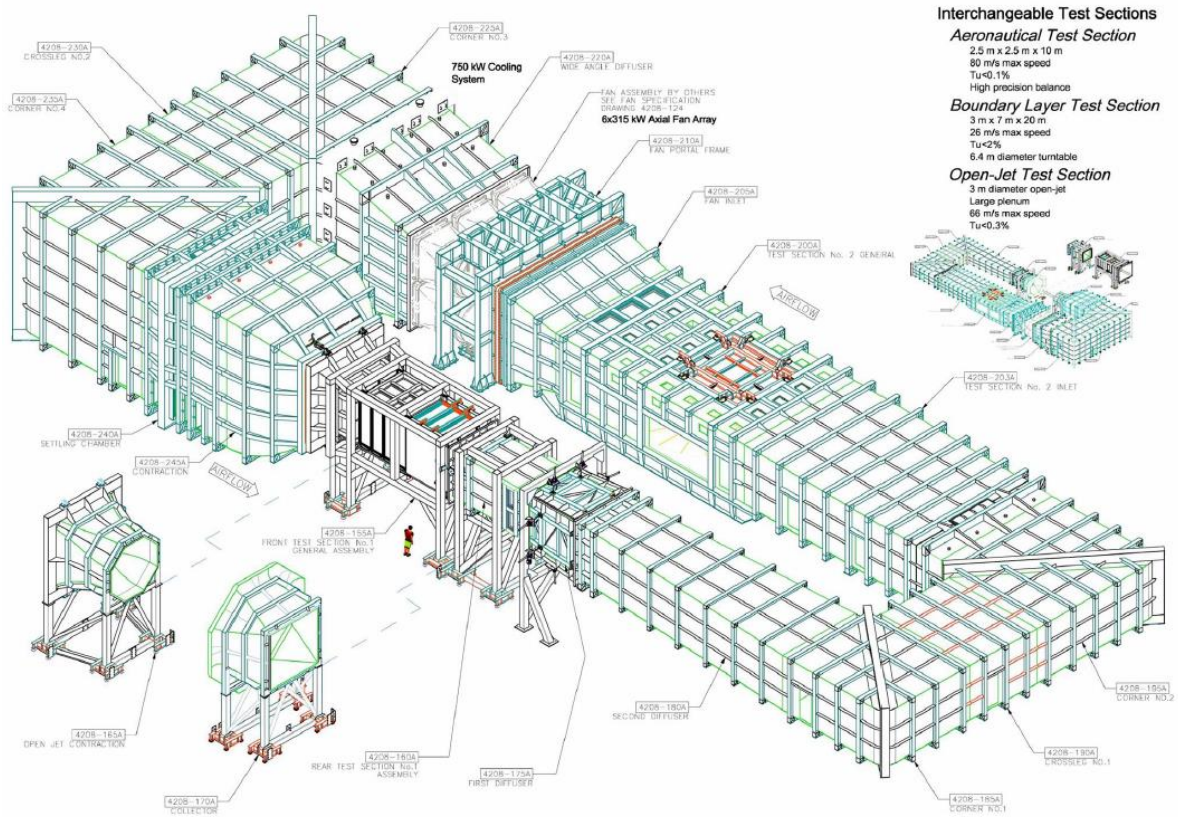

Figure 2.1. METUWIND Large Scale Wind Tunnel [20]

METUWIND LSWT is closed loop, horizontal axis, low subsonic wind tunnel with three interchangeable test sections and 54 m by 18 m footprint. Hangar has 60 m by 20 m by 15 m dimensions with large access doors and a 10-ton overhead crane. There is air bearing system to change aeronautical and open jet test sections. There are 2 honeycombs and 5 screens to regulate the airflow.

The tunnel is driven by 6 axial 2m diameter fans with 1.89 MW total power. Main structure of the tunnel is steel and test sections are mainly wood and plexi-glass situated on steel frames. To reduce the effect of vibrations, these motors are placed on an isolated concrete floor. A 750-kW heat exchanger is also included to keep the air at a consistent temperature throughout the prolonged tests.

As shown in Figure 2.2, tunnel has a LabVIEW based automated control system and speed control for preferred test section can be achieved by manually changing the fan speed or by entering the fixed speed and Reynolds number value. In addition, velocity or Reynolds number information of the test sections can be followed in detail from this screen. In Figure 2.3, the tunnel information screen was shared during the 0° AoA & 5×10^5 Re case experiment. On this screen, critical fan temperatures and vibration rates during the test; open/close information of the doors in the tunnel; air temperature, air density etc. information; flow direction and instantaneous velocity information of test sections on the general diagram of the tunnel are shown.

Test section 1 is aeronautical test section and has 2.5 m by 2.5 m by 10 m dimensions and maximum speed approximately 80 m/s. The turbulence intensity is nearly 0.1% and contraction ratio is 7.84:1. ATS is suitable for force, moment and pressure measurements of scaled aircraft and missile models.

Test section 2 is boundary layer test section and has 3 m by 7 m by 20 m dimensions and the maximum speed approximately is 26 m/s. The turbulence intensity is nearly 2%. BLTS has a 6.4 diameter turntable with approximately 1° sensitivity. Since BLTS has a relatively large cross-section, it is generally suitable for full-scale automotive and aerospace models or bridge and building models exposed to atmospheric flows.

Third section is open jet test section and has 3 m diameter and maximum speed approximately 66 m/s. The turbulence intensity is nearly 0.3% and contraction ratio is 6.93:1. OJTS is generally used for models that do not fit AST and whose structural strength is desired to be measured [21].

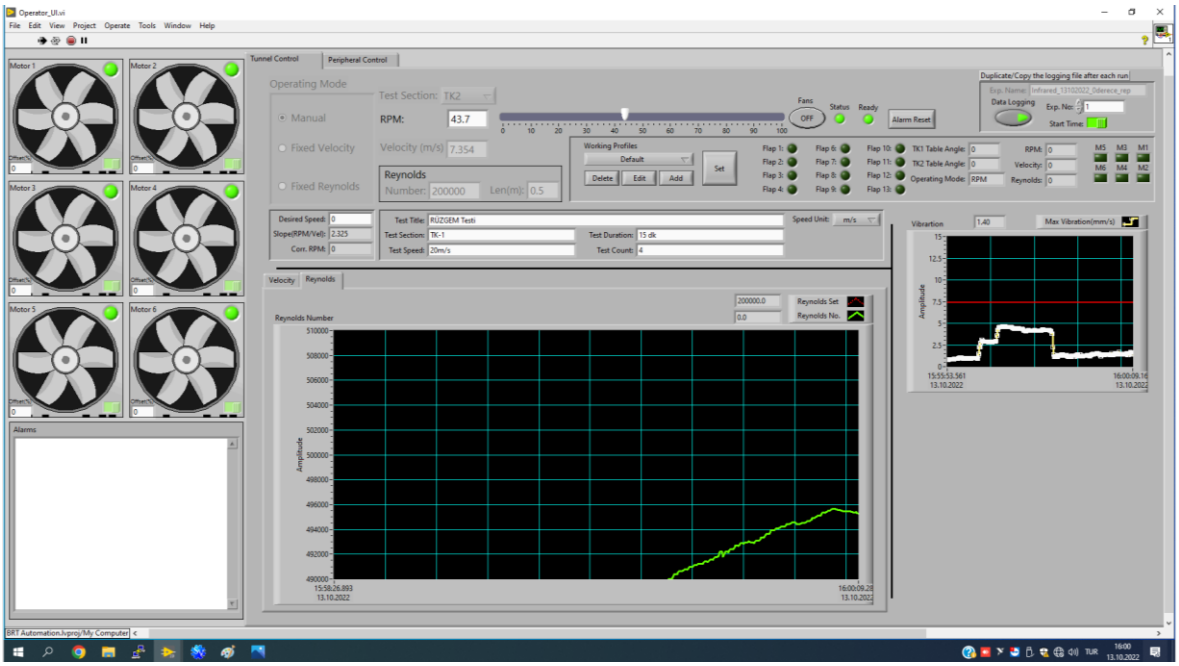

Figure 2.2. METUWIND LSWT Control screen (during AoA = 0° & Re = 5×10^5 case)

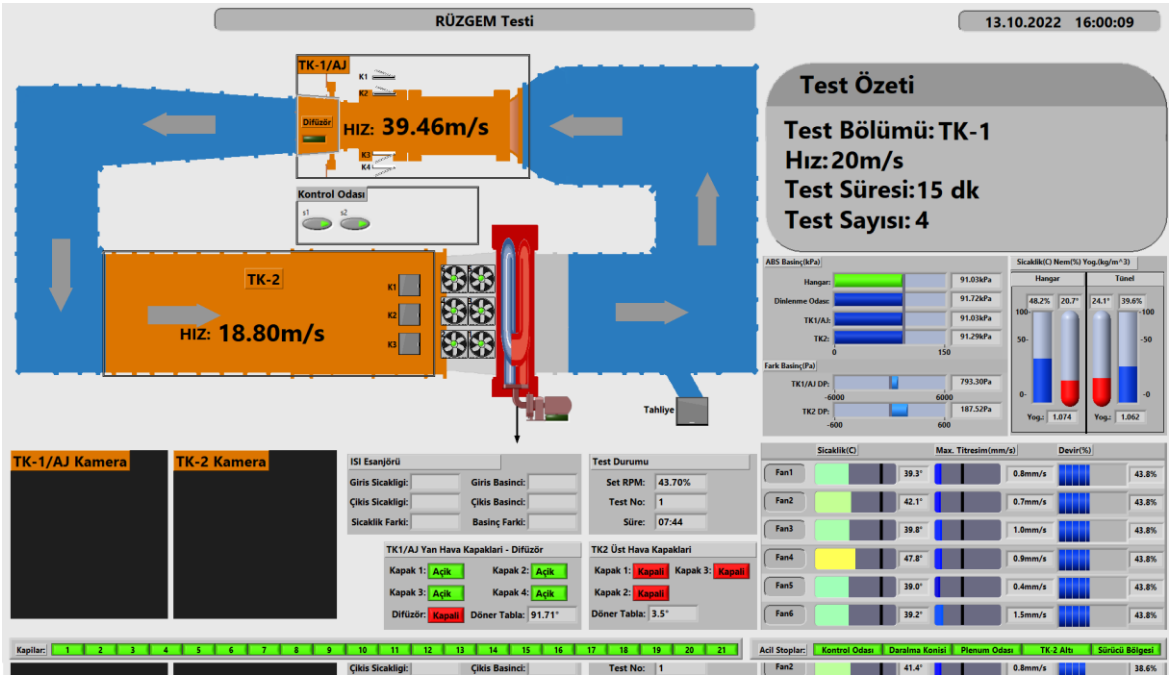

Figure 2.3. METUWIND LSWT Information screen (during AoA = 0° & Re = 5×10^5 case)

2.2. Wing Model

The wing model to be used during the experiments has the NREL (National Renewable Energy Laboratory) S809 airfoil profile. The airfoil having a wingspan of 0.99 m and a chord length of 0.455 m [3]. Following figures demonstrates pictures of the airfoil installed in BLTS.

Figure 2.4. S809 wing model

Here, chord length is used as characteristic length for Reynolds number calculations. The S809 airfoil, which is suitable for laminar flow, is commonly utilized as horizontal axis wind turbine blades [10].

Sanei and Razaghi [57] defined separation-induced transition numerically at a Reynolds number of 5×10^5 using the Spalart-Allmaras turbulence, $k-\omega-\gamma$ transition, and transition SST models. Ramsey and Hoffman [58] observed separation-induced transition experimentally at a Reynolds number of 7.5×10^5 using pressure taps. Thus, it was expected that a laminar separation bubble would occur at approximately half of the chord length of the S809 airfoil within these Reynolds number regimes. Additionally, Jonkman's study [59] demonstrated that stall occurred at approximately 12° angle of attack for a Reynolds number of 5×10^5. This thesis includes both numerical and experimental studies under similar conditions.

2.3. Infrared Camera

As seen in the Figure 2.5, FLIR C2 thermo-camera was used for infrared imaging during the experiment. The IR resolution of the camera is 80 x 60 and image frequency is 9 Hz. The camera's thermal sensitivity is less than 0.10 °C. The spectral range is between 7.5-14 μm. For the data post-processing the Teledyne FLIR Tools+6.4 and FLIR Thermal Studio software and MATLAB were used [22]. Further specifications of the IR camera are given in Appendix A3.

Figure 2.5. FLIR C2 infrared camera

The infrared thermography method does not pollute the setup environment like the filament and oil methods or create additional installation costs and difficulties such as PIV, load cell, pressure scanivalve methods. For the infrared thermography method, fixing the IR camera at the right distance and angle to view the test object is sufficient most of the time.

2.4. Experimental Setup

The experiment procedure was started by fixing the airfoil model to a chipboard to obtain a surface to fix the wing to the test section floor. As provided in the Figure 2.6, the model was fixed perpendicular to the floor and aligned at 0° attack angle according to the incoming flow direction.

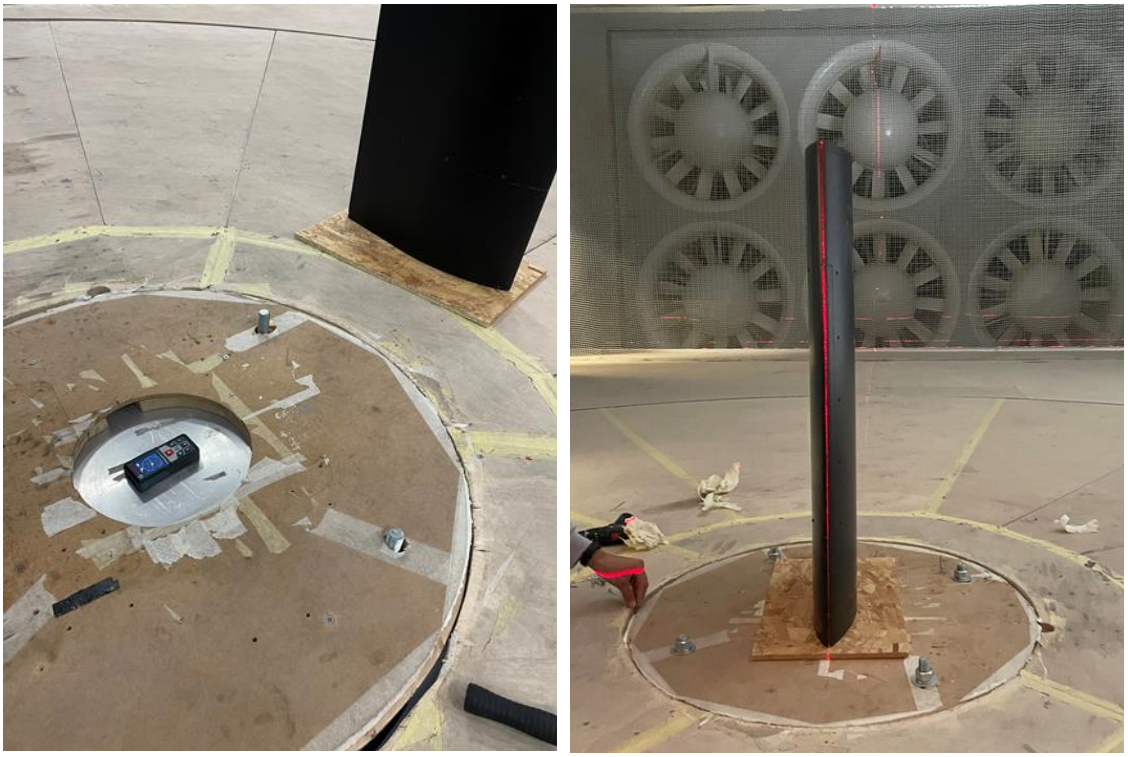

Figure 2.6. Placement of the airfoil in the TS2

Then, the IR camera was fixed to a traverse system so that the entire wing model was viewed perpendicularly, and this traverse system was fixed to the test section floor so that it would not move during the test. The wing model and the positions of the camera relative to each other are given in the Figure 2.7.

In the Figure 2.8, the flow direction, LE, TE, chord length, span etc. information are shown on the photograph after the airfoil model was fixed to the center of the TS2 floor.

Figure 2.7. Positions of the airfoil and IR camera in the TS2

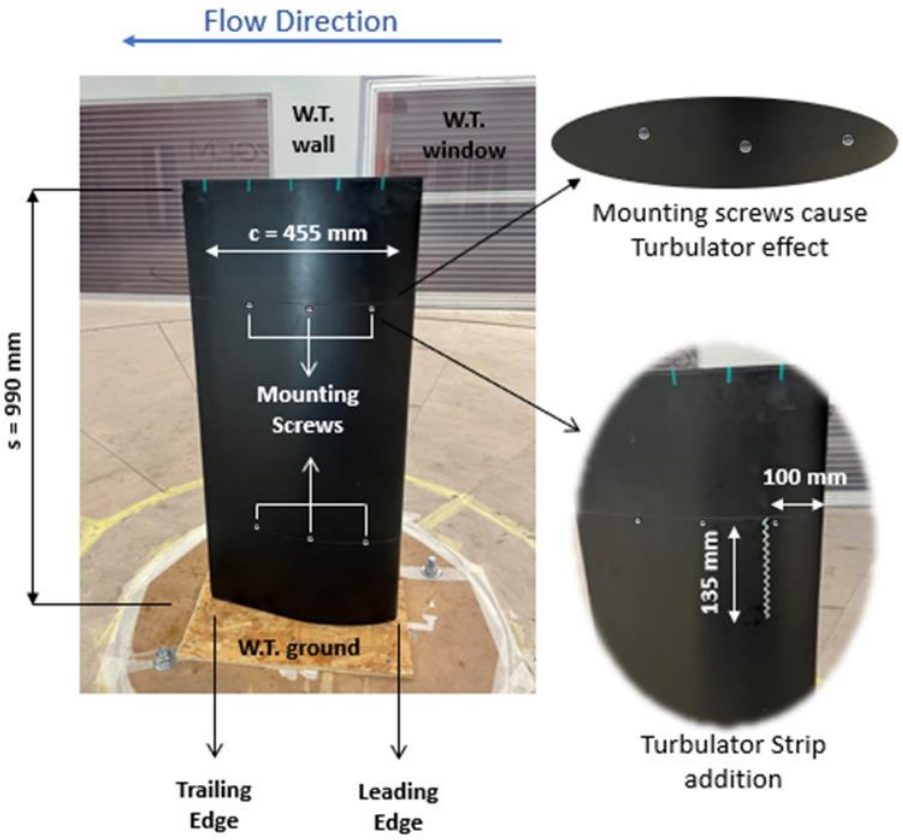

Figure 2.8. Detailed view of the airfoil model in the center of the TS2

In Figure 2.9, general view of experimental setup is given from the point of view of the upstream flow. In this photo taken on TS2, the placement of the airfoil and IR camera traverse system, axial fan array and turntable are clearly shown. The Teledyne FLIR Tools+6.4 software of the camera was installed on one of the computers in the control room. This computer was connected to the IR camera with a cable, and during the test, the camera was triggered via the software to capture images.

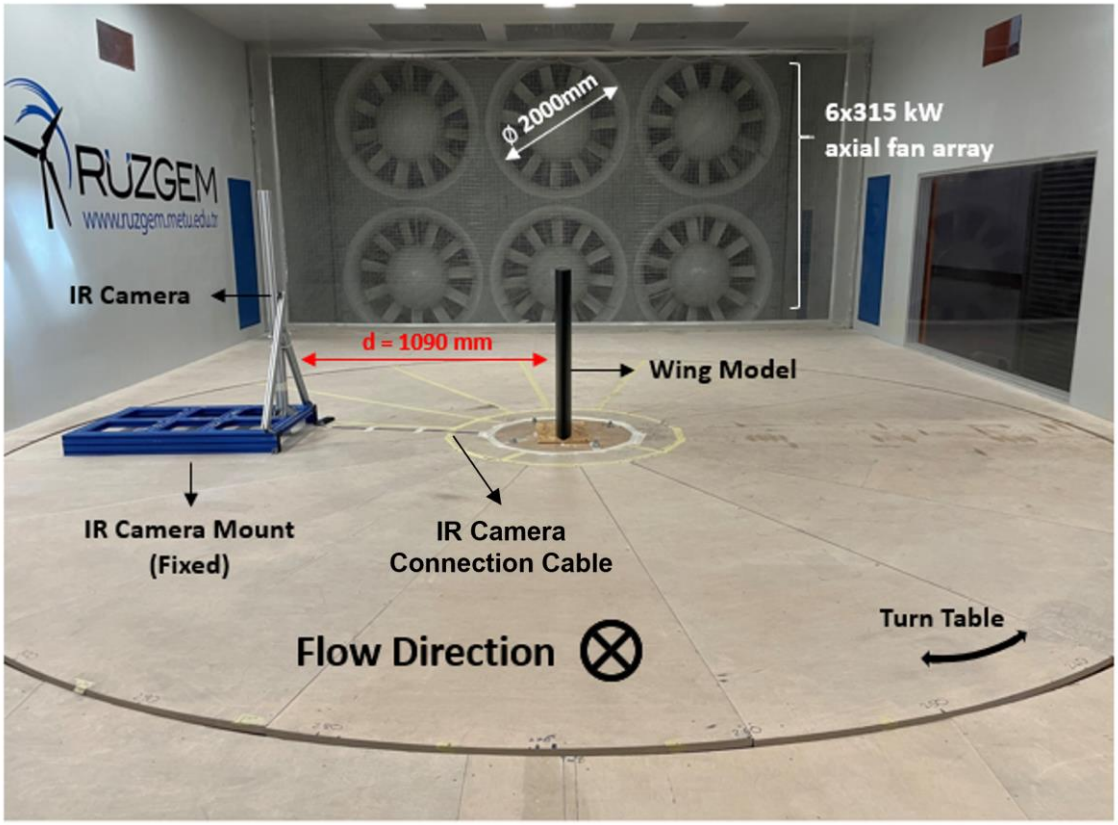

Figure 2.9. General view of the experimental setup

To view the transition flow clearly with the IR camera, basically there must be a temperature difference between the incoming flow and the airfoil surface. Different techniques can be used to create a temperature difference between the object and the flow. For instance, Wynnychuk and Yarusevych, heated the surface of test object throughout their experiments using halogen lamps to create a temperature difference. In their case, the airfoil was warm (heated), the incoming air was relatively cold [9].

In METUWIND LSWT, shortly after the tunnel fans are started, the flow heats up and there is a temperature difference between the airfoil model and the incoming flow. Therefore, in this thesis, during the experiments, the incoming air was warm (heated), the airfoil was relatively cold.

2.5. Experimental Procedure and Test Matrix

While creating the test matrix, the experimental studies in the literature and the capabilities of METUWIND LSWT were considered and some initial trial tests were carried out. Table 2.1 presents the test matrix of the experiments conducted at METUWIND LWST TS2 on October 12 – 14, 2022. All the tests performed in the test campaign are given in Appendix A2. As seen from Table 2.1, experiments were performed between 0° – 12° angle of attack and for a Reynolds number range of 4×10^5 – 7.5×10^5. During the experiment, the tunnel velocity is controlled by the fan speed. However, the measured Reynolds number can vary due to transient effects at a constant fan speed. The desired Reynolds number is the targeted Reynolds number based on chord length in the test matrix. As a result, infrared measurements were at the actual Reynolds number, which is the closest value to the desired Reynolds number.

Table 2.1. Test matrix

Case	AoA	Re_desired
1	0°	400000
2	0°	450000
3	0°	500000
4	0°	550000
5	0°	600000
6	0°	650000
7	0°	700000
8	0°	750000
9	0°	500000
10	3°	500000
11	6°	500000
12	9°	500000
13	12°	500000

First of all, initial tests were carried out at different camera-wing vertical distances (*d*) 1.73 m, 1.09 m and 0.78 m in order to have the most accurate imaging. Since the IR camera views the entire chord of the airfoil and it is optimal in terms of the focusing ability of the IR camera, studies were carried out with a distance of 1.09 m in experimental and numerical post-processing.

Another constraint that was considered was the Reynolds number. Due to the capacity of the tunnel, the upper limit of the Reynolds number was determined as 7.5×10^5. Since no visual change could be observed in the IR camera imaging at very low Reynolds numbers, the lower limit was determined as 4×10^5 for the experiments. Therefore, tests were carried out for a Re range of 4×10^5 – 7.5×10^5. Apart from these tests, experiments were also carried out by attaching zigzag tape to the airfoil in order to observe the effect of the turbulator strip.

For this thesis, a test case is expressed by two variables; Reynolds number and angle of attack. The test procedure is summarized below:

- First, the turntable is set at the desired angle before the tunnel was run.
- Tunnel was operated and data was saved continuously during test.
- The fan speed was increased at a fixed attack angle to achieve the desired Reynolds number.
- After getting as close as possible to the desired Reynolds number, the Reynolds number values were checked on the control screen until they became stable.
- At this point, the IR camera was triggered with FLIR software and an instant IR image of the airfoil was captured. While capturing the image, the time data at the moment the image was taken was also recorded into the image data.
- At the end of these operations, a Reynolds number sweep at constant angle of attack was completed, and log files were created throughout the time from the beginning to the end of the sweep. The naming of these log files was done according to date, *d* value, angle of attack and strip condition. An example of log naming is as follows.

13102022_d=1.09m_AOA0_strip

In test campaign, a total of 20 tests were conducted, including tests for different angle of attack values, different *d* values, and whether the strip was attached or not, along with trial-and-repeat tests, resulting in the creation of 20 different log files accordingly. Due to the resolution of the camera and temporal variation of the flow speed some cases were repeated to make sure that reliable results are obtained. Cases for experimental post process and numeric preprocess were selected from the clearest images from many repeated tests for the same case.

2.6. Post Process Analysis of Experiments

In this section, the post-processing of the experimental results is explained. All cases mentioned in test matrix are discussed in detail in Section 4.1. However, it is important to determine and analyze critical cases for numerical analysis. Case eliminations are also explained in this part.

In experimental post-processing, it was revealed that there is very little chordwise temperature variation on the airfoil surface at low speeds. For this reason, test cases with Reynolds numbers 500000 and above were analyzed only. In the experiments, Re = 50000 interval was used for velocity sweep. However, since there is no marginal change in speed in this range, it has been shown by post-processing that there is also no significant change in the separation and transition onset points on the airfoil. Therefore, the velocity sweep interval for CFD analyzes was determined as Re = 100000.

Another case where no temperature change could be observed was the cases at high angles, as it caused a direct turbulence transition very close to the leading edge. Then, it was decided that the angle change would be between 0 and 9 degrees with 3 degrees intervals. Furthermore, since it directly started turbulence and a transition flow could not be observed, cases with turbulator zigzag tape attached to the airfoil were also not included in the CFD analysis.

Both by visual inspection of the IR images and as a result of experimental post-processing, cases for CFD analysis were determined as follows;

I. Constant Angle of Attack, Varying Reynolds Number Cases (3 Cases)

For AoA = 0°; Re = 5×10^5, 6×10^5 and 7×10^5 cases were simulated.

II. Varying Angle of Attack, Constant Reynolds Number Cases (4 Cases)

For Re = 5×10^5; AoA = 0°, 3°, 6° and 9° cases were simulated.

The experimental procedure and Section 2.5 explain how a sweep was carried out and how datalog files were created. To understand the structure of a datalog file, the Reynolds number and temperature values plotted over time for 0° angle of attack, *d* value of 1.09 m and 'not mounted strip condition' as shown Figure 2.10.

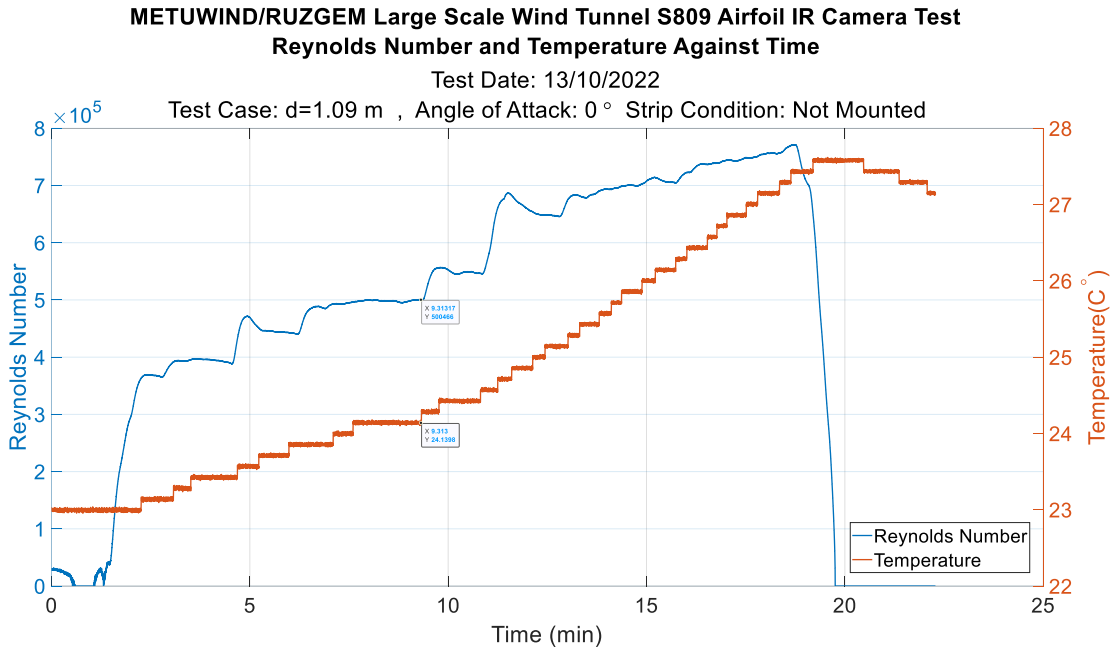

Figure 2.10. Reynolds number and temperature changes for AoA = 0°, *d* = 1.09 m and not mounted strip condition

As can be seen in Figure 2.10, during the sweep, as the fan speed was increased, the tunnel Reynolds numbers increased, leading to an increase in the tunnel air temperature. It can be seen that a period of time was waited for the flow to stabilize at the desired Reynolds numbers and for the wing temperature values to settle. For example, in the figure above, it is clearly observed that it takes time for the velocity to stabilize from the 7th minute to the 9th minute in order to reach a Reynolds number of 5×10^5. Although not as long as for this specific Reynolds number, a short waiting period was observed for each velocity setting for other Reynolds numbers as well. At the end of the sweep, the fan speed was gradually reduced and as a result, the Reynolds number decreased and the sweep was completed.

In the written MATLAB script, the flow temperature and Reynolds number change with respect to time, the exact values of the actual Reynolds number, kinematic and dynamic

viscosities, air velocity, temperature, pressure and density at the time of the infrared image time stamp were obtained from the corresponding data files (logs). For the dynamic viscosity, the temperature based correlation obtained from [40] is used. The inputs of the scripts are the name of the experimental case, the exact time of the infrared image, and the chord length of the airfoil. The MATLAB script also calculates the first cell height (Δy_1) to be used in the CFD mesh corresponding to y+ = 1. For this calculation, a function is used in the main script that takes tunnel density, tunnel air viscosity, tunnel velocity, chord length, and desired y+ value as input and calculates the first layer thickness with y+ equation in Equation 2.4. The code uses skin friction correlation to calculate wall shear stress and friction velocity which described in Schlichting [8] as shown Equation 2.1-2.2-2.3.

$$C_f = (2 \log Re_x - 0.65)^{-2.3} \tag{2.1}$$

$$\tau_w = 0.5\, C_f\, \rho\, {U_\infty}^2 \tag{2.2}$$

$$u_\tau = \sqrt{\frac{\tau_w}{\rho}} \tag{2.3}$$

$$y+ = \frac{u_\tau \Delta y_1 \rho}{\mu} \tag{2.4}$$

The aim at this stage of the study is to obtain tunnel values at the time the photograph was taken and to conduct CFD analyses with these values. Therefore, a Matlab code was written that outputs the tunnel values at the time the photograph was taken and the values required during CFD analysis. The inputs required for the written code are listed below.

This Matlab code takes the following values as an input:

- name of the experimental case
- the date, hour, minute and second to be examined
- the length of the airfoil chord as characteristic length (*c*)
- desired y+ = 1

With the inputs stated above, the code can find the data corresponding to the date the photo was taken from among different test data. After receiving these inputs, the code can extract the following data from the datalog.

Following values taken from tunnel datalog:

- Tunnel TS2 velocity – air velocity in the tunnel
- Tunnel contraction temperature – air temperature in the tunnel
- Tunnel contraction pressure – air pressure in the tunnel
- Tunnel contraction density – air density in the tunnel

The data calculated in the code is as follows:

- Actual Reynolds number
- Kinematic and dynamic viscosity
- First cell height

The main code utilizes a function to compute the tunnel air viscosity, which takes the temperature of the tunnel as input. The actual Reynolds number at the time the IR photo was taken is then determined by utilizing the characteristic length and the velocity derived from the tunnel datalog.

It should be noted that the temperature value obtained from the tunnel datalog is measured by a system located before TS1. In other words, the tunnel air temperature is measured first, and then it passes through the air contraction, bends, and honeycomb screens. It can be inferred that the air temperature may have slightly increased at TS2 due to these components.

In the following table, a sample output of code is shown for 0° angle of attack and Re_desired = 5×10^5. As can be seen from the information here, during the experiment, an image was taken from the IR camera in conditions where Reynolds number is as close to the desired Reynolds number of 500000 as possible (actual Re = 500207.71). However, since there is a small difference and this difference affects other variables and calculations, the actual values in the experiment were used in CFD analysis.

Table 2.2. Conditions for AoA = 0° & Re = 5×10^5 case

```
Test case: 13102022_d=1.09m_derece0
Specified time: 13-Oct-2022 16:01:45
----------------------------------------
Experimental Outputs
----------------------------------------
Reynolds Number: 500207.71
TK2 Velocity: 18.82 m/s
Tunnel Contraction Temperature: 24.14 degree
Tunnel Contraction Pressure: 91741.29 Pa
Tunnel Contraction Density: 1.06 kg/s
Tunnel Kinematic Viscosity: 1.711918e-05 m^2/s
Tunnel Dynamic Viscosity: 1.817237e-05 Pa.s
----------------------------------------
Numerical Outputs
----------------------------------------
Desired Y+ Value: 1
First cell height (Fluent input) is: 3.719788e-05
```

The parameters outlined in Table 2.2 were carried out for all CFD cases and the necessary information for CFD analysis is summarized in Table 2.3 for all cases.

Table 2.3. Conditions for CFD cases

Case	AoA (°)	Re_desired	Re_actual	Velocity (m/s)	Pressure (Pa)	Density (kg/m^3)	Dynamic Viscosity (Pa.s)	First Cell Height (m)
3	0	500000	500208	18.8	91741	1.06	1.82E-05	3.71979E-05
5	0	600000	594042	22.3	92134	1.06	1.81E-05	3.18571E-05
7	0	700000	714120	26.9	92392	1.05	1.81E-05	2.70883E-05
9	0	500000	500207	18.8	91741	1.06	1.82E-05	3.71979E-05
10	3	500000	499401	18.3	91863	1.08	1.80E-05	3.66766E-05
11	6	500000	501544	18.5	91763	1.07	1.80E-05	3.66981E-05
12	9	500000	497443	18.6	91741	1.07	1.81E-05	3.72544E-05

2.7. Experimental Determination of Separation, Transition and Reattachment Points

In this particular section of the thesis, it will be explained how the separation, transition, and reattachment points in the laminar separation bubble are determined experimentally. Before sharing the methodology used to identify these points based on experimental data, the physical logic will be discussed.

When a laminar separation bubble forms on an airfoil, an air mass will form on the airfoil except where the bubble formed. Considering that there will less heat transfer by convective and conduction in the absence of matter, it can be said that it would be quite reasonable to conduct an experimental study over heat transfer to determine the bubble. Moreover, the turbulent boundary layer has higher convective heat transfer coefficients compared to the laminar boundary layer, and if transition occurs, there will be higher heat transfer in the turbulent region. In this case, an aerothermal phenomenon will need to be examined in the experimental study to be carried out. By creating a temperature difference between the air and the wing surface to facilitate heat transfer, the wing surface will have a temperature distribution due to the separation bubble and transitional flow. As a result, if this temperature distribution can be observed, bubble and transition points can be determined.

In the experiments, the IR camera gives this distribution as visual results, but it is important to analyze these results quantitatively in order to compare the experimental data both among themselves and with CFD analyses.

In Section 2.3, it was mentioned that the camera used in the experiments had an IR resolution of 80 x 60. For each IR image taken, according to the position of the camera in this experiment, the horizontal axis of the image is divided by 60 and the vertical axis by 80. Thus, each image consists of 4800 elements and the temperature value is recorded for each element and it is named as raw data. The raw data were used in the experimental part of the thesis for each IR photograph. The visual representation of raw data for 0° angle of attack and 5×10^5 Reynolds number case is shown in Figure 2.11a. The image is

created on written MATLAB code for 4800 data points according to temperature magnitudes. However, when IR cameras generate images, they use interpolation methods called color interpolation using the raw measurement data. Interpolated values during image creation ensure smoother images. In Figure 2.11b., the same raw data is subjected to linear interpolation five times using the written code, and the image is created based on the interpolated data. As can be seen, the interpolated data has a smoother appearance, making it easier to examine visually.

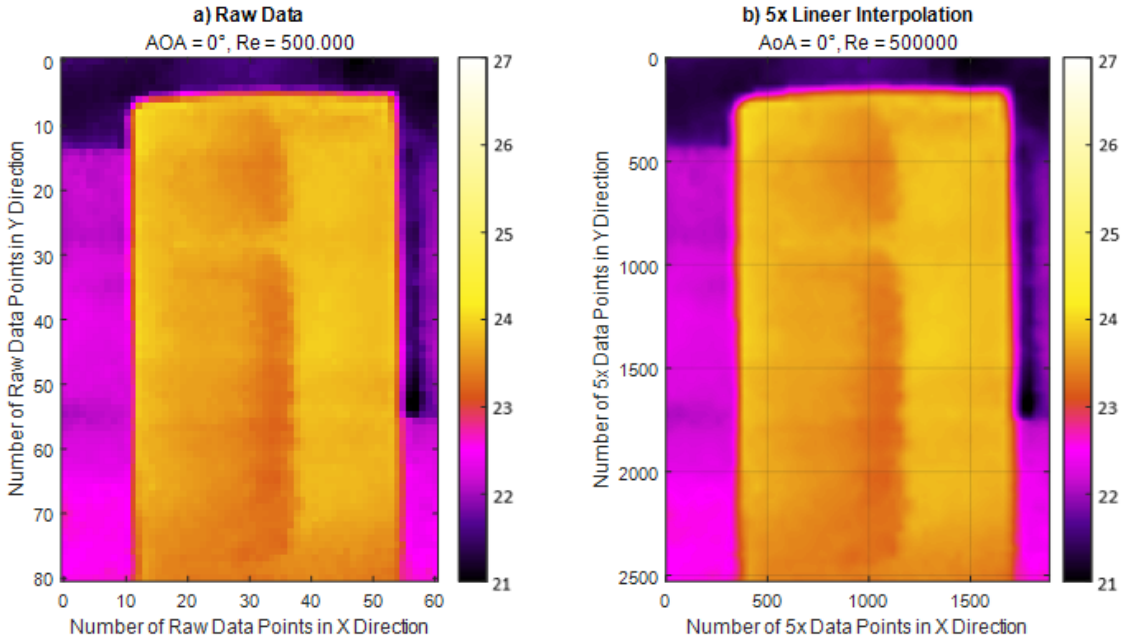

Figure 2.11. Raw data and linearly interpolated data images for AoA = 0° & Re_desired = 5×10^5 case

Similarly, to the above, in this thesis, images obtained from the FLIR C2 camera, which utilizes interpolation techniques when generating IR images, will be shared. However, the data to be processed in this section will be the raw data mentioned above.

It is possible to predict how this temperature distribution will occur. Here, the incoming air can be either warmer or colder than the wing to induce heat transfer. Assuming that the air is initially hot and moving along the wing surface from the leading edge to the trailing edge above a certain value on the wing span, the temperature distribution will be similar as below, as demonstrated by a sample from the conducted tests.

Since it is away from ground, tip, and turbulator screw effect, the surface temperature data along the chordwise direction was obtained from the mid-span of the airfoil, as shown in Figure 2.12.

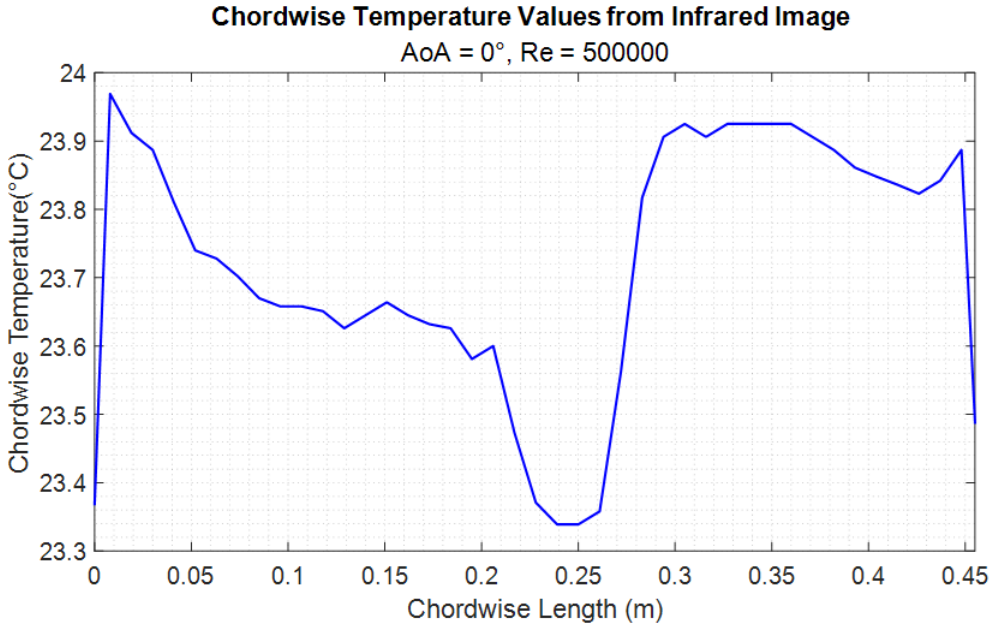

Figure 2.12. Sample temperature distribution of the airfoil surface for hot incoming air

Moving in the direction of flow, the temperatures will be high in the leading edge due to the stagnation point. Subsequently, as the boundary layer develops and shear stresses decrease, heat transfer and temperature will begin to decrease. Then, when separation occurs, the hot air will no longer be able to heat the wing, and wall temperatures will drastically drop. At this point, the wing temperature will reach a minimum value, and with reattachment, the temperature will rise suddenly. If it is considered that the flow is turbulent for reattachment and beyond, it is known that turbulent boundary layers have higher heat transfer coefficients. Therefore, the temperature values will be higher in the turbulent region than the laminar region, and depending on the amount of turbulence and the development of the boundary layer, the temperatures will either slightly decrease or remain constant towards the trailing edge. If the air temperature is lower, the direction of heat transfer will change and the temperatures will change in the opposite direction at the points mentioned above.

At this point, a methodology is needed to determine the laminar, transition, and reattachment points exactly. In the literature, it is observed that the derivative of temperature along the chord length is utilized to identify the separation and transition points [9].

According to Wynnychuk & Yarusevych [9], the flow direction temperature gradient providing the minimum convection coefficient represents the start of separation. Heat flux is positive when the test object is hot compared to the incoming air flow, and in this case, the minimum convection heat transfer coefficient is provided at the maximum chordwise temperature gradient.

In the separated shear layer, the transition process results in a sharp increase in near-wall velocity fluctuations and consistently growing magnitudes of mean reverse flow velocity toward the region of maximum bubble height. This causes a rapid decrease after maximum temperature on the airfoil surface. Numerical results show that [42], mean transition position approximately coincides with the maximum separation bubble height, corresponds to the maximum gradient downstream of convective heat transfer coefficient. In addition, with similar approach, studies involving near-wall transition estimates [43], [44], [45], [46], [47], [48], [49] the position of the mean transition can be predicted at the position minimum temperature gradient in the flow direction.

After transition point, the surface temperature continues to drop until it reaches a local minimum. This is followed by a slower temperature recovery expected for the turbulent boundary layer that is re-forming. Reattachment of the flow to the airfoil surface and high levels of near-wall fluctuations induced by shear layer vortices. In other words, the flow becomes fully turbulent and the impinges to the airfoil surface increases the interaction between the surface and the incoming air, and the convective heat transfer coefficient reaches its maximum. Wynnychuk & Yarusevych [9] experiments, the location of minimum temperature or zero streamwise temperature gradient represents the maximum convective heat transfer coefficient.

In the case Wynnychuk & Yarusevych [9] where the air temperature is lower, the separation, transition, and reattachment points are determined as follows:

- When dT/dx is MAX value corresponding chord length → Separation point
- When dT/dx is MIN value corresponding chord length → Transition onset point
- When T is local MIN value corresponding chord length → Reattachment point

In this thesis, the incoming air is warm (heated), the airfoil is relatively cold. Thus, the heat flux is reversed compared to the Wynnychuk & Yarusevych [9] case. In the light of the information described above, the minimum convection heat transfer coefficient is provided by the minimum chordwise temperature gradient and it can be used for separation point. For position of the mean transition can be predicted at the position maximum temperature gradient in the flow direction. Lastly, because the convective heat transfer coefficient reaches its maximum at reattachment point, location of maximum can be used as reattachment point. As a result, separation, transition and reattachment points were found as follows:

- ✓ When dT/dx is MIN value corresponding chord length → Separation point
- ✓ When dT/dx is MAX value corresponding chord length → Transition onset point
- ✓ When T is local MAX value corresponding chord length → Reattachment point

Where T is chordwise temperature and dT/dx first derivative of chordwise temperature. Derivative of temperature values are calculated using first order finite difference approximation; forward difference is used for the first value, central difference is used for the values in between, backward difference is used for the last value.

When calculations are performed based on the previously shared example of temperature distribution, the separation, transition, and reattachment points are found as shown in following Figure 2.13.

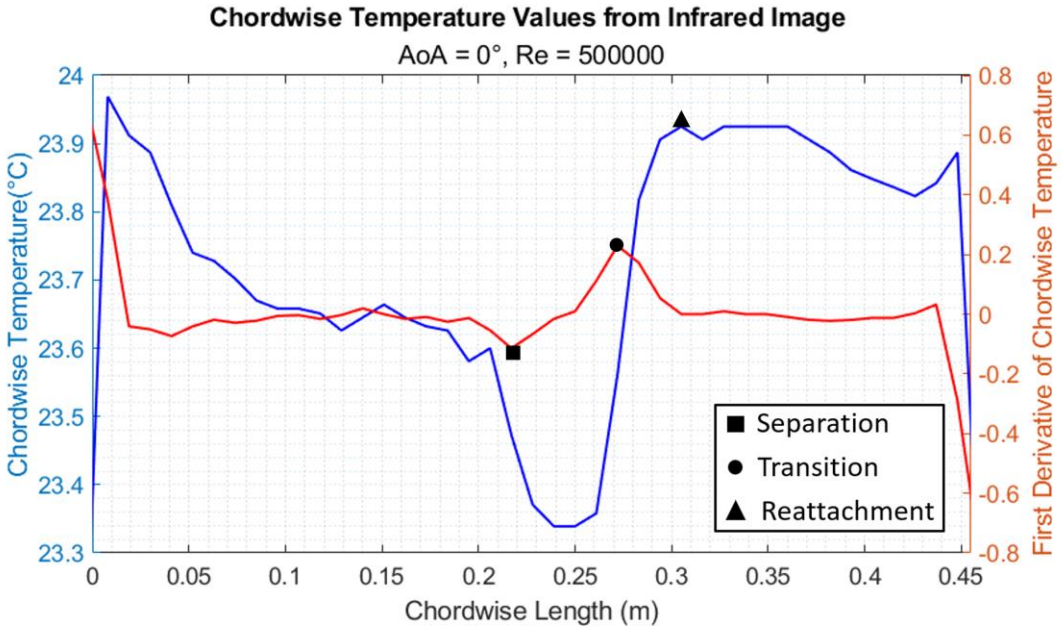

Figure 2.13. An example of the determination of separation, transition, and reattachment points

In the thesis, similar to the example mentioned above, all cases were analyzed to determine these points.

2.8. Uncertainty Estimates of Experiments

Uncertainty analysis involves evaluating and quantifying the uncertainties associated with measurements and observations made during the experiment.

The most significant uncertainty in these experiments arises from the measurements of the infrared camera. During the experiment, the camera was used in a vertical orientation, with 80 pixels in the vertical axis and 60 pixels in the horizontal axis. Since the separation, transition, and reattachment points are crucial with respect to the chordwise position of the airfoil, the horizontal resolution of the IR camera is important for this experiment. The horizontal length seen by the IR camera was measured to be 0.66 meters. When divided by 60 pixels, the horizontal length of one pixel was found to be 0.011 meter. As a result, it was inferred that the locations of the separation, transition, and reattachment points were measured with an approximate accuracy of 0.011 m. Another uncertainty is the sensitivity of the IR camera, which is less than 0.10°C.

2.9. Repeatability Analysis of Experiments

Repeatability analysis refers to the process of evaluating the consistency and reproducibility of experimental measurements or observations. It involves conducting multiple repetitions of the same experiment under similar conditions to assess the level of agreement among the results.

To observe the consistency of the results, repeat tests were conducted for some of the cases mentioned in this thesis. In Figure 2.14 and Figure 2.15, repeatability plots are provided for Reynolds numbers of 5×10^5 and 7×10^5, respectively, for the 0° angle of attack.

In the graphs, the solid lines represent the primary tests, while the dashed lines represent the repeat tests conducted for the same Reynolds number and angle of attack.

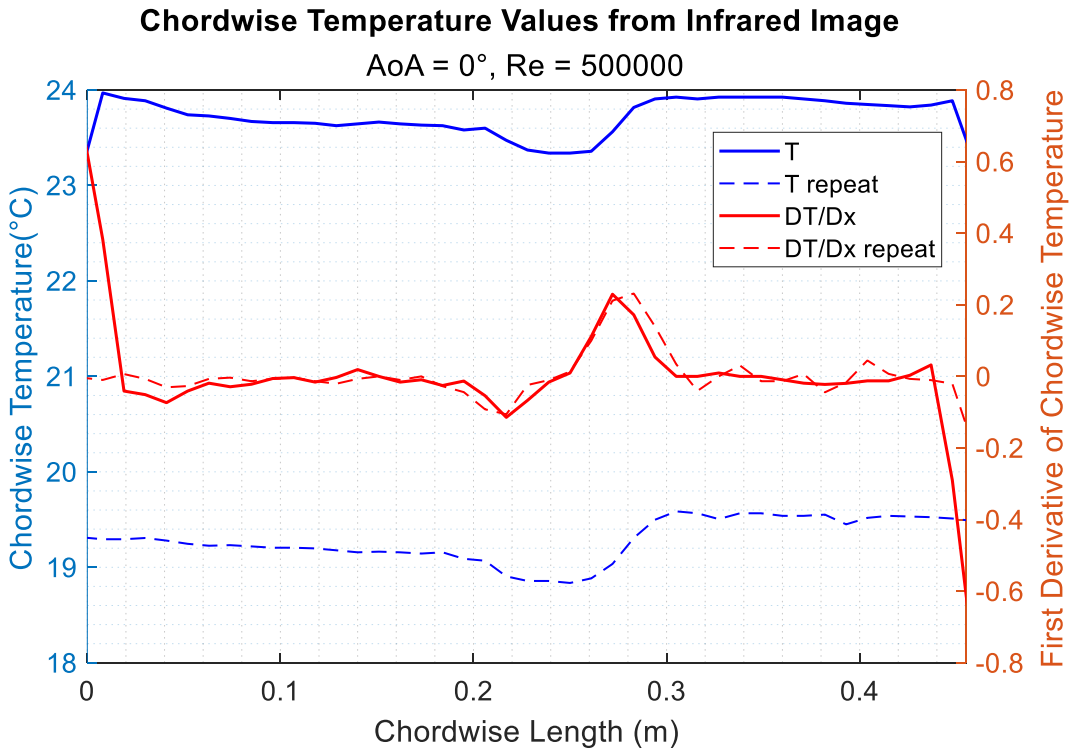

Figure 2.14. Repeatability analysis for AoA = 0° & Re = 5×10^5 case

Due to the primary test and repeat test being conducted at different times, such as a few hours later, the surface temperatures of the airfoil are different. However, the temperature plots shown in blue color have followed the same trend, and as a result, temperature derivatives have also been very similar.

The locations of the separation, transition and reattachment points are very close for both the primary and repeat tests because the position of the local maximum temperature and the derivative values of the temperature are important factors in determining these points.

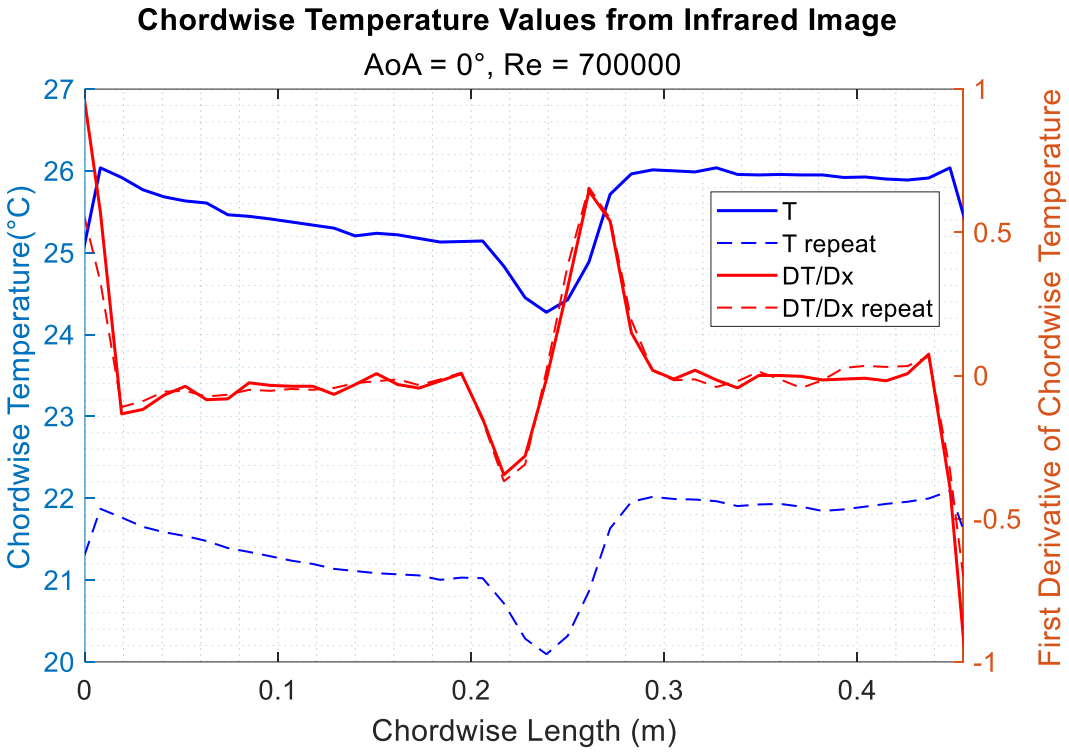

Figure 2.15. Repeatability analysis for AoA = 0° & Re = 7×10^5 case

As seen from the above figures, repeat tests for different conditions have yielded very close results to the primary tests. This indicates that the experiments mentioned in this thesis are repeatable, meaning they can be replicated with consistent and similar outcomes.

3. NUMERICAL STUDIES

In this section, the numerical part of the thesis, which is the computational fluid dynamics analysis, is shared. Theoretical background which includes governing equations and turbulence models, pre-process of CFD and CFD studies are given.

3.1. Theorical Background of Computational Fluid Dynamics

Turbulent flow can basically be defined as many eddy populations consisting of constantly changing, swirling flow structures of varying size and strength, giving the flow a random appearance. Turbulence modeling involves the utilization of mathematical models to predict the impact of turbulence.

In turbulence models, it is generally accepted that the flow is fully turbulent and there is no transition flow. As a result, turbulence models mostly overlook the transition flow, and in cases where transition flow is important, these models can give results that are far from the exact solution. This thesis focused on transition flow models.

The basic equation of fluid mechanics, assumptions and mathematical modeling of turbulence will be discussed within the context of the theory of CFD.

3.1.1. Governing Equations

Computational fluid dynamics (CFD) is a field within fluid mechanics that employs numerical techniques to analyze and solve problems related to fluid flows. As a computational tool, computers are used to simulate fluid flow and interaction with surfaces defined by boundary conditions. The Navier-Stokes equations provide a basis for practically most of the CFD problems.

In this part, the governing equations of fluid modeling are shared. The equations are given in cartesian coordinates.

Firstly, the continuity equation specified in Equation 3.1. In this equation, ρ, t, x_i and u_i represent density, time, position in the i direction and velocity in the i direction respectively.

$$\frac{\partial \rho}{\partial t} + \frac{\partial (\rho u_i)}{\partial x_i} = 0 \tag{3.1}$$

Secondly, the momentum equation explained by Newton's second law specified in Equation (3.2). In a control volume, the total momentum is always conserved, it changes only with the effect of force. Pressure is on the right side of the equation is expressed with p, while τ_{ij} represents the viscous stress tensor.

$$\frac{\partial (\rho u_i)}{\partial t} + \frac{\partial (\rho u_j u_i)}{\partial x_i} = -\frac{\partial p}{\partial x_i} + \frac{\partial \tau_{ij}}{\partial x_i} \tag{3.2}$$

The expression for the viscous stress tensor is given in Equation 3.3, denoted by the symbol μ dynamic viscosity associated with linear deformations represents stresses while λ represents stresses associated with volumetric deformations. Volumetric viscosity is also known as "bulk viscosity" and this secondary viscosity has little effect in practice.

$$\tau_{ij} = \mu \left(\frac{\partial u_i}{\partial x_j} + \frac{\partial u_j}{\partial x_i} \right) + \lambda \delta_{ij} \frac{\partial u_k}{\partial x_k} \tag{3.3}$$

For gases, usually $\lambda = -\frac{2}{3\mu}$ [8]. In this thesis, since the flow investigated is at low subsonic speeds, the flow can be considered as incompressible as a result $\nabla . u = 0$ and the viscous stress tensor can be expressed as in Equation 3.4.

$$\tau_{ij} = \mu \left(\frac{\partial u_i}{\partial x_j} + \frac{\partial u_j}{\partial x_i} \right) \tag{3.4}$$

No heat transfer or chemical reaction was considered in this study. Incompressible, isothermal, steady CFD simulations were carried out. Therefore, the above mass and momentum conservation equations can be simplified to:

$$\frac{\partial (u_i)}{\partial x_i} = 0 \tag{3.5}$$

$$\rho u_j \frac{\partial(u_i)}{\partial x_i} = -\frac{\partial p}{\partial x_i} + \mu \left(\frac{\partial^2 u_i}{\partial x_i x_j}\right) \tag{3.6}$$

3.1.2. Turbulence Models

Turbulence is one of the problems of classical physics which are not fully solved. The governing equations of fluid flows, known as the Navier-Stokes equations, can be directly solved without the need for any modeling assumptions. Direct Numerical Simulation (DNS) involves solving for a wide range of spatial and temporal scales, spanning from large to small, down to the Kolmogorov length scale. Kolmogorov length scale is the smallest dimension of an eddy that can be encountered in a turbulent flow [23]. Due to immense computational expenses, using the DNS technique in engineering applications is still difficult. In practice, DNS is primarily utilized within academic and research settings for modeling relatively straightforward flow scenarios. It is used in conjunction with experiments to comprehend turbulence better and to provide simplified turbulence models that are less expensive to calculate but still useful to predict the main contribution of turbulence to the flow [24].

The Large Eddy Simulation (LES), which is time-dependent technique, based on solving large eddies of turbulence while small-scale eddies are modeled [26]. In Figure 3.1, channel flow sketch illustrates how LES resolution and DNS resolution differ from each other. As can be demonstrated, large eddies are resolved with LES and smaller ones modeled. The effects of the minor fluctuations cannot be detected in the results because they are not fully resolved.

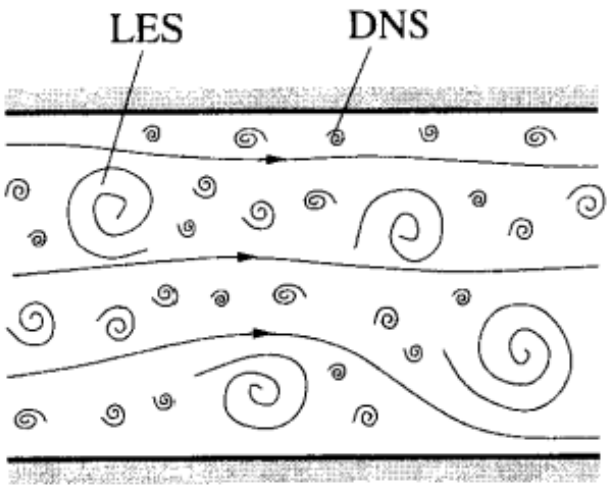

Figure 3.1. A symbolic view of comparison between LES and DNS [25]

LES provides a wider variety of applications and a higher level of solution accuracy than the RANS methods. However, for steady, one- or two-dimensional flows, large-eddy simulation is significantly more expensive than RANS methods, shown in Figure 3.2. For this reason, it should be used to solve issues where the cost is comparable to solving the RANS equations or when lower-level turbulence models do not work.

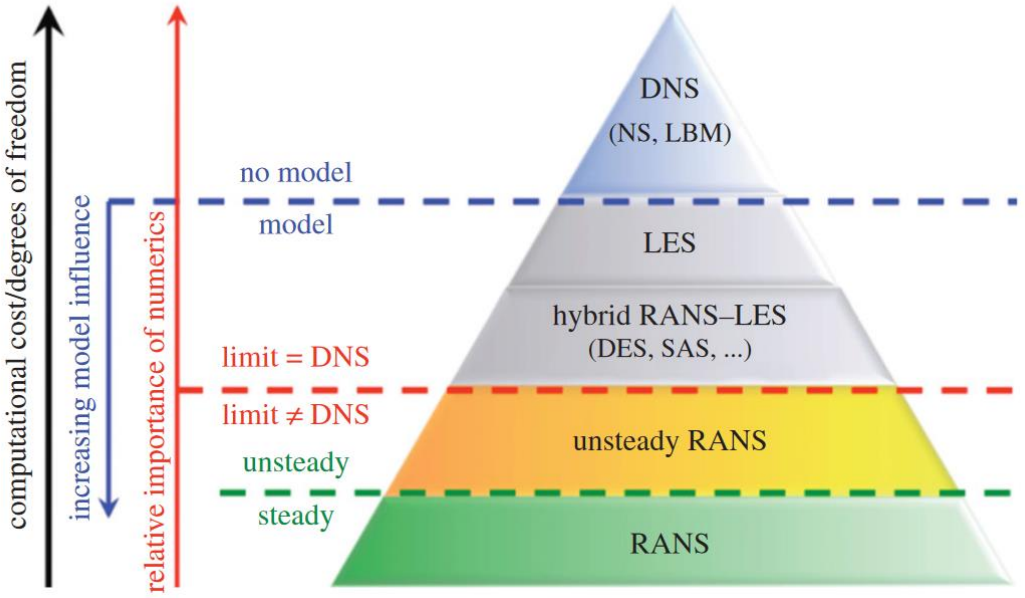

Figure 3.2. Classification of unsteady approaches according to levels of modelling and readiness [27]

Using the Reynolds Averaged Navier Stokes (RANS) methodology, the eddies in the flow field are modeled. Eddies are not directly solvable using this method. Utilizing the mean and the rate of mean change, the scaler values of the magnitudes are calculated. Compared to DNS and LES approach, RANS method offers lower cost in terms of computational resources. The RANS approach is the most commonly used CFD analysis method today and provides valuable information especially during the research and design phases. In the next section, the RANS method is presented in detail.

3.1.2.1. Reynolds Averaged Navier Stokes Equations (RANS)

In the RANS method, instantaneous flow variables in the Navier-Stokes equations are decomposed into two parts, the mean part and the oscillating part, as follows:

$$u_i = \overline{u_i} + u_i' \tag{3.7}$$

where u_i is instantaneous, $\overline{u_i}$ is mean, u_i' is fluctuating velocity components for i = 1,2,3. Likewise, other flow variables in the NS equations can also be decomposed.

The RANS continuity and momentum equations obtained after these processes are given below [34]:

$$\frac{\partial \rho}{\partial t} + \frac{\partial (\rho u_i)}{\partial x_i} = 0 \tag{3.8}$$

$$\frac{\partial (\rho u_i)}{\partial t} + \frac{\partial (\rho u_i u_j)}{\partial x_j} = -\frac{\partial p}{\partial x_i} + \frac{\partial}{\partial x_j}\left[\mu\left(\frac{\partial u_i}{\partial x_j} + \frac{\partial u_j}{\partial x_i}\right) - \frac{2}{3}\delta_{ij}\frac{\partial u_k}{\partial x_k}\right] + \frac{\partial}{\partial x_j}\left(-\rho\overline{u_i' u_j'}\right) \tag{3.9}$$

ρ represents the density of the fluid, t represents time, u represents the velocity vector of the fluid, μ represents the dynamic viscosity of the fluid. An extra term appears in the above RANS momentum equations. This additional $-\rho\overline{u_i' u_j'}$ term is the Reynolds stress terms need to be modelled. Here, u_i' and u_j' are the instantaneous deviations of the velocity in the x and y directions from the average velocity values in x and y directions. This term expresses the convection of mean momentum due to turbulence and is the term that distinguishes turbulent flow from laminar flow. Due to the chaotic nature of the turbulence phenomenon, there is no analytical method for calculating these additional

values. For this reason, turbulence models were developed to calculate deviation values from the mean velocity to calculate this term.

There are different approaches for calculating the Reynolds stress tensor. The Reynolds stress model calculates each component in this tensor, but the high number of equations to be solved creates expensive CFD solution costs. Another approach is the Boussinesq approach, which assumes that all the elements in the tensor are equal to each other, given in Equation 3.10.

$$\left(-\rho\overline{u_i'u_j'}\right) = \mu_t\left(\frac{\partial u_i}{\partial x_j} + \frac{\partial u_j}{\partial x_i}\right) - \frac{2}{3}\left(\rho k + \mu_t\frac{\partial u_k}{\partial x_k}\right)\delta_{ij} \tag{3.10}$$

According to the Boussinesq approximation, the Reynolds stress tensor and viscous stress tensors are expressed similarly for incompressible flows [28]. The expression μ_t in the Reynolds stress tensor equation represents the turbulent viscosity term [29]. In this approach, the turbulent viscosity term, μ_t is solved by turbulence models.

Note that, since the transition flow is examined within the scope of the thesis, the use of turbulence models that based transition flow is the most important factor in solving the problem. However, in order to compare transition models, standard $k-\varepsilon$ turbulence model is also presented.

3.1.2.1.1. $k-\varepsilon$ Turbulence Model

The $k-\varepsilon$ turbulence model is a widely used two equation model for simulating turbulent flows in CFD. The standard $k-\varepsilon$ model was developed by Jones and Launder in 1972 [30]. This model is a type of RANS model that aims to predict the distribution of turbulent kinetic energy and the rate of dissipation of turbulent kinetic energy. The $k-\varepsilon$ model assumes that the turbulent eddies in a flow can be characterized by two distinct length scales: the turbulent kinetic energy scale and the turbulent length scale. These length scales are related to the turbulent Reynolds stresses that arise due to the interaction between the turbulent fluctuations and the mean flow. The $k-\varepsilon$ model solves two transport equations: one for the turbulent kinetic energy and one for the rate of dissipation of turbulent kinetic energy. These equations are coupled and are solved simultaneously with the governing equations of fluid flow. The two transport equations are given below.

$$\frac{\partial(\rho k)}{\partial t} + \frac{\partial(\rho u_j k)}{\partial x_j} = \frac{\partial}{\partial x_j}\left[\left(\mu + \frac{\mu_t}{\sigma_k}\right)\frac{\partial k}{\partial x_j}\right] + P - \rho\varepsilon \tag{3.11}$$

$$\frac{\partial(\rho\varepsilon)}{\partial t} + \frac{\partial(\rho u_j \varepsilon)}{\partial x_j} = \frac{\partial}{\partial x_j}\left[\left(\mu + \frac{\mu_t}{\sigma_\varepsilon}\right)\frac{\partial \varepsilon}{\partial x_j}\right] + C_{\varepsilon 1}\frac{\varepsilon}{k}P - C_{\varepsilon 2}\rho\frac{\varepsilon^2}{k} \tag{3.12}$$

k represents the turbulent kinetic energy, ε represents the rate of loss of turbulent kinetic energy, μ_t is the turbulent viscosity of the fluid.

The model requires two closure assumptions. First assumption is the turbulent viscosity is proportional to k^2/ε. Second assumption is the production of turbulent kinetic energy is proportional to the product of the mean velocity gradients and the turbulent kinetic energy.

Turbulent viscosity is also given in the equation below:

$$\mu_t = \rho C_\mu \frac{k^2}{\varepsilon} \tag{3.13}$$

σ_k, σ_ε, $C_{\varepsilon 1}$, $C_{\varepsilon 2}$, C_μ terms in the equations represent the experimental constants used in the standard k-epsilon model, values are given below:

$$\sigma_k = 1.00, \quad \sigma_\varepsilon = 1.30, \quad C_{\varepsilon 1} = 1.44, \quad C_{\varepsilon 2} = 1.92, \quad C_\mu = 0.09 \tag{3.14}$$

P term is turbulent kinetic energy production rate and as shown by Equation (3.15) is obtained.

$$P = \mu_t\left(\frac{\partial u_i}{\partial x_j} + \frac{\partial u_j}{\partial x_i}\right)\frac{\partial u_i}{\partial x_j} \tag{3.15}$$

The $k - \varepsilon$ turbulence model is often used in engineering applications, such as aerospace and automotive, because of its accuracy and computational efficiency. However, it has some limitations, particularly for flows with strong streamline curvature or separation, where more advanced turbulence models may be required.

3.1.2.1.2. $k-\omega-\gamma$ Transition Model

Firstly, the $k-\omega$ SST turbulence model was developed by Menter and Langtry [32], [33]. $k-\omega$ SST turbulence model consists of using Wilcox's $k-\omega$ turbulence model [31] for regions close to the wall and the standard $k-\varepsilon$ model for free flow regions away from the wall. The $k-\omega-\gamma$ transition model is an extension of the $k-\omega$ SST turbulence model, developed by Menter at ANSYS, Inc [34].

The $k-\omega-\gamma$ transition model uses two transport equations for the turbulence variables; turbulence transport equations for the specific dissipation rate and turbulent kinetic energy [35]. The other transport equation is for transition and named as intermittency equation. The intermittency function is used to switch between laminar and turbulent flow regions based on the local flow conditions. These equations are solved numerically in the simulation to calculate the turbulent viscosity, which is used to determine the turbulent stresses in the flow. The $k-\omega-\gamma$ transition model involves the following set of equations:

The transport equation for intermittency (γ) is described below:

$$\frac{\partial(\rho\gamma)}{\partial t}+\frac{\partial(\rho U_j\gamma)}{\partial x_j}=P_\gamma-E_\gamma+\frac{\partial}{\partial x_j}\left[\left(\mu+\frac{\mu_t}{\sigma_\gamma}\right)\frac{\partial\gamma}{\partial x_j}\right] \tag{3.16}$$

$$P_\gamma=F_{length}\ \rho\,S\,\gamma(1-\gamma)\,F_{onset} \tag{3.17}$$

$$E_\gamma=c_{a2}\,\rho\,\Omega\,\gamma\,F_{turb}\,(c_{e2}\gamma-1) \tag{3.18}$$

$$F_{length}=100,\quad c_{e2}=50,\quad c_{a2}=0.06,\quad \sigma_\gamma=1.0 \tag{3.19}$$

In above equations, P_γ is defined as transition source term and E_γ is defined as destruction or re-laminarization source term. In P_γ equation, S is strain rate magnitude and F_{onset} is for triggering the intermittency production. In E_γ equation, Ω is defined as the magnitude of absolute vorticity rate and F_{turb} is used to disable the destruction or re-laminarization source outside of a laminar boundary layer or in the viscous sublayer. The constants are described in Equation 3.19.

The transport equation for the turbulent kinetic energy (k) is:

$$\frac{\partial(\rho k)}{\partial t} + \frac{\partial(\rho u_j k)}{\partial x_j} = \tilde{P}_k + P_k^{lim} - \widetilde{D}_k + \frac{\partial}{\partial x_j}\left[(\mu + \sigma_k \mu_t)\frac{\partial k}{\partial x_j}\right] \tag{3.20}$$

$$\tilde{P}_k = \gamma P_k \tag{3.21}$$

$$\widetilde{D}_k = \max(\gamma, 0.1) \cdot D_k \tag{3.22}$$

$$\mu_t = \rho \frac{a_1 \cdot k}{\max(a_1 \cdot \omega, F_2 \cdot S)} \tag{3.23}$$

$$P_k = \mu_t S \, \Omega \tag{3.24}$$

$$P_k^{lim} = 5C_k \max(\gamma - 0.2, 0)(1 - \gamma) F_{on}^{lim} \max(3C_{SEP}\, \mu - \mu_t, 0)\, S \, \Omega \tag{3.25}$$

$$F_{on}^{lim} = \min\left(\max\left(\frac{Re_V}{2.2 \cdot Re_{\theta c}^{lim}} - 1, 0\right), 3\right) \tag{3.26}$$

$$Re_{\theta c}^{lim} = 1100 \tag{3.27}$$

$$C_k = 1.0, \; C_{SEP} = 1.0 \tag{3.28}$$

The P_k and D_k are the production and destruction terms for energy equation in the original SST turbulence model and γ is the intermittency. The P_k^{lim} term is for proper generation of k at transition points for arbitrary low Tu levels. In P_k^{lim} term, the $Re_{\theta c}^{lim}$ value limits the term and ensures that the term is only activated for high Reynolds numbers or separating flows, where Re_V becomes larger than this limit. Also, σ_k is the turbulent Prandtl number for k and μ_t is turbulence viscosity.

The transport equation for the specific dissipation rate (omega) is:

$$\frac{\partial(\rho\omega)}{\partial t} + \frac{\partial(\rho u_j \omega)}{\partial x_j} = \alpha \frac{P_k}{\nu_t} - D_\omega + Cd_\omega + \frac{\partial}{\partial x_j}\left((\mu + \sigma_\omega \, \mu_t)\frac{\partial \omega}{\partial x_j}\right) \tag{3.29}$$

In this equation Cd_ω is additional cross diffusion term for turbulent dissipation rate and D_ω is the destructive term for turbulent dissipation rate.

The $k-\omega-\gamma$ transition model has been calibrated against a wide range of external aeronautical and turbomachinery applications. Because $k-\omega-\gamma$ transition model requires three transport equations to solve, it has an advantage in terms of computational cost. However, this model is specifically designed for wall-bounded flows and is not suitable for predicting transition in free shear flows. The model will predict free shear flows as fully turbulent. Thus, the $k-\omega-\gamma$ transition model is useful for classical boundary layer flows and reduces the computational effort in these types of problems.

3.1.2.1.3. Transition $k-kl-\omega$ Model

The $k-kl-\omega$ model is an extension of the standard $k-\omega$ model and is specifically designed to handle flow transition from laminar to turbulent [36]. In this model, the turbulence is modeled using two equations, one for the turbulent kinetic energy and one for the specific turbulent dissipation rate. The additional "kl" in the model name stands for "k-laminar" and refers to an additional variable included in the model to account for the laminar to turbulent transition process.

The equations for the $k-kl-\omega$ model are:

$$\frac{\partial(\rho k)}{\partial t}+\frac{\partial(\rho u_j k)}{\partial x_j}=P_k-\varepsilon+\frac{\partial}{\partial x_j}\left[\left(\mu+\frac{\mu_t}{\sigma_k}\right)\frac{\partial k}{\partial x_j}\right] \tag{3.30}$$

k is turbulent kinetic energy, P_k is the production of turbulence kinetic energy due to mean velocity gradients, ε is the dissipation rate of turbulence kinetic energy, σ_k is the turbulent Prandtl number for k.

$$\frac{\partial(\rho\omega)}{\partial t}+\frac{\partial(\rho u_j \omega)}{\partial x_j}=C_{\omega 1}P_k-C_{\omega 2}\rho\frac{\omega^2}{k}+\frac{\partial}{\partial x_j}\left[\left(\mu+\frac{\mu_t}{\sigma_\omega}\right)\frac{\partial\omega}{\partial x_j}\right] \tag{3.31}$$

ω is the specific turbulent dissipation rate, $C_{\omega 1}$ and $C_{\omega 2}$ are constants and σ_ω is the turbulent Prandtl number for ω.

The $k-kl-\omega$ model also includes an additional equation for the variable kl, which is used to model the laminar-to-turbulent transition process. The equation for kl is:

$$\frac{\partial(\rho kl)}{\partial t} + \frac{\partial(\rho u_j kl)}{\partial x_j} = \max[0, R] - \beta_{kl}\omega_{kl}kl + \frac{\partial}{\partial x_j}\left[\left(\mu + \frac{\mu_t}{\sigma_{kl}}\right)\frac{\partial kl}{\partial x_j}\right] \quad (3.32)$$

kl is the fraction of the flow that is still laminar, R is the rate of change of the turbulence kinetic energy, β_{kl} is a constant, ω_{kl} is the specific turbulent dissipation rate calculated using the laminar viscosity, σ_{kl} is the turbulent Prandtl number for kl.

3.1.2.1.4. Transition SST Model

The Transition SST model also known as the $\gamma - Re_\theta$ model is a four equation model developed by Langtry and Menter [37]. It is based on the coupling of modified $k - \omega$ SST turbulence model transport equations with two other transition related transport equations, one for the intermittency and one for the transition onset criteria, in terms of momentum-thickness Reynolds number.

The transport equation for intermittency is described below:

$$\frac{\partial(\rho\gamma)}{\partial t} + \frac{\partial(\rho U_j\gamma)}{\partial x_j} = P_\gamma - E_\gamma + \frac{\partial}{\partial x_j}\left[\left(\mu + \frac{\mu_t}{\sigma_f}\right)\frac{\partial\gamma}{\partial x_j}\right] \quad (3.33)$$

$$P_\gamma = F_{length}\, c_{a1}\, \rho\, S\, [\gamma\, F_{onset}]^{0.5}(1 - c_{e1}\gamma) \quad (3.34)$$

$$E_\gamma = c_{a2}\, \rho\, \Omega\, \gamma\, F_{turb}\, (c_{e2}\gamma - 1) \quad (3.35)$$

$$c_{a1} = 2\,, \quad c_{e1} = 1.0, \quad c_{e2} = 50\,, \quad c_{a2} = 0.06\,, \quad \sigma_f = 1.0 \quad (3.36)$$

In above equations, P_γ is the transition source term and E_γ is destruction or re-laminarization source term. In P_γ equation, S is the strain rate magnitude. This term is designed to be equal to zero in the laminar boundary layer upstream of transition and active everywhere the local vorticity Reynolds number exceeds the local transition onset criteria. The transition length function (F_{length}) regulates the magnitude of this source term. The presence of density and strain rate ensures that the source term has the correct units. The c_{e1} is constant to limit the maximum value of intermittency and the F_{onset} is used to trigger the intermittency production.

In E_γ equation, vorticity magnitude (Ω) ensures that in the laminar boundary layer, the intermittency is close to zero which helps in re-laminarization prediction. The constant c_{a2} controls the strength of the destruction term and ensures that this term is smaller than the transition source term P_γ. The constant c_{e2} controls the lower limit of intermittency, where the term changes sign. F_{turb} is used to disable the destruction/relaminarization source outside of a laminar boundary layer or in the viscous sublayer. The constants are described in Equation 3.36.

The Reynolds momentum-thickness equation ($Re_{\theta t}$) is described below:

$$\frac{\partial(\rho Re_{\theta t})}{\partial t} + \frac{\partial(\rho u_j \overline{Re_{\theta t}})}{\partial x_j} = P_{\theta t} + \frac{\partial}{\partial x_j}\left[\sigma_{\theta t}(\mu + \mu_t)\frac{\partial \overline{Re_{\theta t}}}{\partial x_j}\right] \tag{3.37}$$

$$P_{\theta t} = c_{\theta t}\frac{\rho}{t}(Re_{\theta t} - \overline{Re_{\theta t}})(1.0 - F_{\theta t}) \tag{3.37}$$

$$t = \frac{500\,\mu}{\rho\, U^2} \tag{3.38}$$

$$c_{\theta t} = 0.03, \quad \sigma_{\theta t} = 0.03 \tag{3.39}$$

In this equation, $P_{\theta t}$ is designed to force the transported scalar $Re_{\theta t}$ to match the local value of $Re_{\theta t}$ calculated from an empirical correlation t is a time scale, which is present for dimensional reasons. The blending function $F_{\theta t}$ is used to turn off the source term in the boundary layer. The constants are described in Equation 3.39.

Modified $k-\omega$ SST transport equation for turbulence kinetic energy is as follows:

$$\frac{\partial(\rho k)}{\partial t} + \frac{\partial(\rho u_j k)}{\partial x_j} = \tilde{P}_k - \widetilde{D}_k + \frac{\partial}{\partial x_j}\left[(\mu + \sigma_k \mu_t)\frac{\partial k}{\partial x_j}\right] \tag{3.40}$$

$$\tilde{P}_k = \gamma_{eff}\, P_k \tag{3.41}$$

$$\widetilde{D}_k = \min\left(\max\left(\gamma_{eff}, 0.1\right), 1.0\right) D_k \tag{3.42}$$

$$\gamma_{eff} = (\gamma, \gamma_{sep}) \tag{3.43}$$

$$\gamma_{sep} = min\left(s_1 \max\left[0, \left(\frac{Re_v}{3.235\, Re_{\theta c}}\right) - 1\right] F_{reattach}, 2\right) F_{\theta t} \tag{3.44}$$

$$s_1 = 2 \tag{3.45}$$

$$F_{reattach} = e^{-\left(\frac{R_T}{20}\right)^4} \tag{3.46}$$

The $\tilde{P}_k$ and $\tilde{D}_k$ are the production and destruction terms for energy equation in the original SST turbulence model and γ_{eff} is the effective intermittency. The effective intermittency is equal to the intermittency from the transport equation everywhere except in the laminar separation bubble where it is allowed to increase beyond one. For a laminar separation the vorticity Reynolds number (Re_v) significantly exceeds the critical momentum thickness Reynolds number ($Re_{\theta c}$). As a result, the ratio between the two (when $Re_v > Re_{\theta c}$) can be thought of as a measure of the size of the laminar separation. The size of the separation bubble can be controlled with the constant s_1. $F_{reattach}$ disables the modification once the viscosity ratio is large enough to cause reattachment. $F_{\theta t}$ is the blending function and confines the modification to boundary layer type flows. Also, R_T represents viscosity ratio and μ_t is turbulence viscosity.

Modified $k-\omega$ SST transport equation for specific turbulent dissipation rate as follows:

$$\frac{\partial(\rho\omega)}{\partial t} + \frac{\partial(\rho u_j \omega)}{\partial x_j} = \alpha \frac{P_k}{\nu_t} - D_\omega + Cd_\omega + \frac{\partial}{\partial x_j}\left[(\mu + \sigma_k \mu_t)\frac{\partial \omega}{\partial x_j}\right] \tag{3.47}$$

In this equation D_ω is the destructive term for turbulent dissipation rate and Cd_ω is additional cross diffusion term for turbulent dissipation rate.

The Transition SST (Shear Stress Transport) model is commonly used in computational fluid dynamics (CFD) simulations for a wide range of applications, especially in engineering and industrial fields where transitional flows are encountered.

Overall, the Transition SST model is a robust transition model that can be applied to a wide range of transitional flow problems, making it a popular transition model choice in many engineering and industrial applications.

3.1.2.2. Strategy for Turbulence Models

In this thesis, for numerical part, $k-\varepsilon$ turbulence model was first used to show the difference between a standard turbulence model and turbulence models which have transition related transport equations. For transition models, in many test cases, $k-\omega-\gamma$ transition model, transition $k-kl-\omega$ model and Transition SST model produce similar results. However, because the $k-\omega-\gamma$ and Transition SST model combined with robust SST turbulence model and Transition SST model solves two additional transport equations, Transition SST model is used in Section 3.3.2 of the thesis. The discrepancies in turbulence models are also investigated in Section 4.2.1 for this specific problem.

3.2. Numerical Determination of Separation, Transition and Reattachment Points

In order to compare the test results with the CFD analysis results, the separation, transition on set and reattachment points should also be determined for the CFD analysis results. It is possible to determine these points with number of methods like flow patterns, pressure distributions and velocity profiles. In this thesis, skin friction coefficient, intermittency and turbulence intensity values were used as is generally the case in the literature. In the following sections, some important definitions are given to define the separation, transition and reattachment points.

3.2.1. Separation and Reattachment Point Determination Method

Skin friction

Skin friction is a result of the interaction between the fluid and the surface of the object, which occurs within the boundary layer. In the below equation, Cf is the skin friction coefficient, ρ_∞ is the density of the free stream, V_∞ is the free stream speed, τ_w is the absolute wall shear stress on the surface, $\frac{1}{2}\rho_\infty V_\infty = q_\infty$ is the dynamic pressure of free stream. In this thesis, wall shear stress magnitude will be used in skin friction relation as shown below:

$$Cf = \frac{|\tau_w|}{\frac{1}{2}\rho_\infty {V_\infty}^2} \tag{3.48}$$

From the above equation, if the wall shear stress increases skin friction coefficient also increases. Since the wall shear stress of the turbulent boundary layer is greater than that of the laminar boundary layer, the turbulent surface friction values will be greater than laminar surface friction values.

The flow within the laminar separation bubble recirculates, causing the flow at the wall surface within the bubble to occur in the opposite direction of the freestream. Therefore, the wall shear stress in laminar separation bubble becomes negative as shown Figure 3.3 [51], [52]. Due to this situation, the separation and reattachment points will correspond to the points where the shear stress is zero, and therefore the Cf values are zero at those points as shown Figure 3.4. Thus, in this thesis, location of separation and reattachment points will be determined where skin friction values are zero in skin friction – chordwise position graph, respectively.

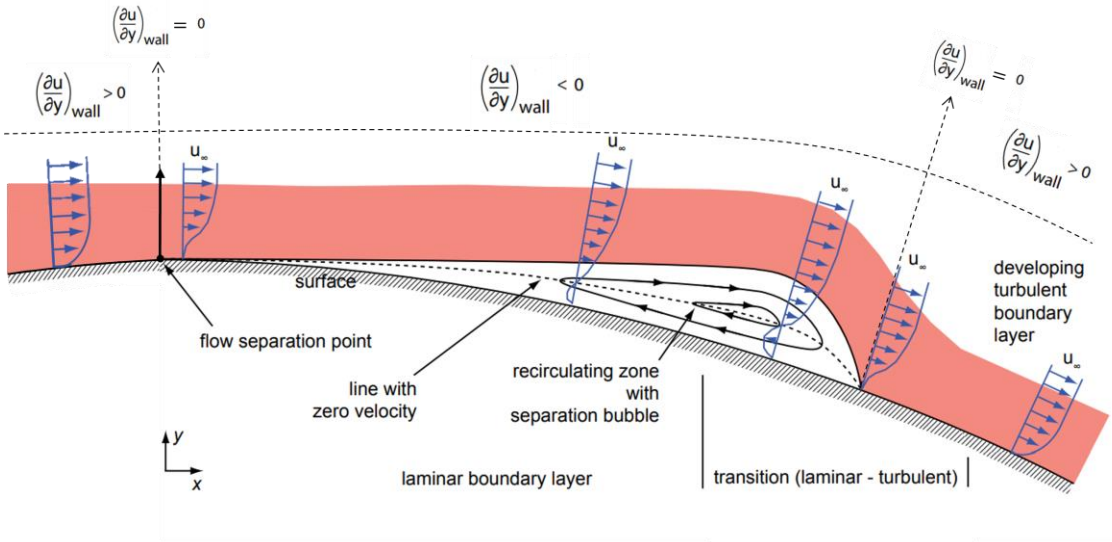

Figure 3.3. Laminar separation bubble and shear stress [51]

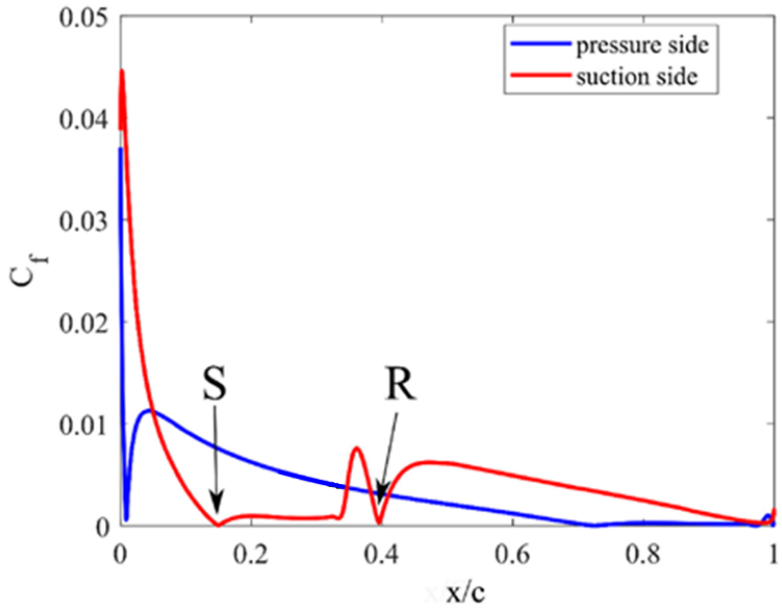

Figure 3.4. Sample skin friction – chordwise position graph (S: Separation, R: Reattachment) [56]

3.2.2. Transition onset Point Determination Method

Turbulence Intensity (Tu) and Turbulence Kinetic Energy(k)

Turbulence intensity is a measure of the turbulence in a fluid flow. Turbulence intensity is calculated by taking the ratio of the root-mean-square velocity fluctuations to the mean velocity of the flow. It is often used in conjunction with other flow parameters, such as Reynolds number and turbulence kinetic energy, to fully characterize the turbulent behavior of a fluid flow.

The relationship between turbulence intensity and turbulence kinetic energy can be expressed mathematically using the following equations:

$$Tu = \frac{V_{RMS}}{V_{mean}} 100\% = \frac{\sqrt{\frac{1}{3}(u_i'^2 + u_j'^2 + u_k'^2)}}{\sqrt{u_i^2 + u_j^2 + u_k^2}} \times 100\% \tag{3.49}$$

Tu is turbulence intensity, V_{RMS} is the root-mean-square velocity fluctuations and V_{mean} is the mean velocity of the flow.

$$k = \frac{1}{2}(u_i'^2 + u_j'^2 + u_k'^2) \tag{3.50}$$

k is turbulence kinetic energy, u_i', u_j', and u_k' are the velocity fluctuations in the x, y, and z directions, respectively.

The turbulence kinetic energy can also be related to the turbulence intensity using the following equation:

$$k = \frac{3}{2}\left(\frac{Tu}{100\%}\right)^2 {V_{mean}}^2 \tag{3.51}$$

Above equation shows that the turbulence kinetic energy is proportional to the square of the turbulence intensity and the mean velocity of the flow. The turbulence kinetic energy is an important parameter in fluid mechanics because it represents the energy associated with the turbulent fluctuations in the flow.

A sudden increase in turbulent kinetic energy indicates the occurrence of transition [50]. Then it maintains at a high level and gradually weakens till the trailing edge due to the inverse pressure gradient. Because of the relationship between turbulence kinetic energy and turbulence intensity, a similar logic can be applied to turbulence intensity. As a result of CFD analysis, the transition can be determined by finding the chordwise position where the turbulence intensity values obtained from the top surface of the airfoil starts to increase dramatically.

Intermittency

The intermittency factor ranges from 0 to 1, with a value of 0 indicating a laminar region and a value of 1 indicating a fully turbulent regime [53]. The results for intermittency are given for intermittency related transition models in Section 4.2.1.

In this study, as a result of CFD analysis, the transition onset point was determined by finding the chordwise position where the intermittency starts to increase [54]. In order to see clearly the transition onset point, intermittency data was taken over an offset that follows the airfoil surface at a height of 0.7 mm as the same approach was applied in reference [55]. The representation is shown in Figure 3.5 for AoA = 0° & Re = 5×10^5 case for transition SST model. In this intermittency contour graph, the white line represents the offset line from which the intermittency values are taken.

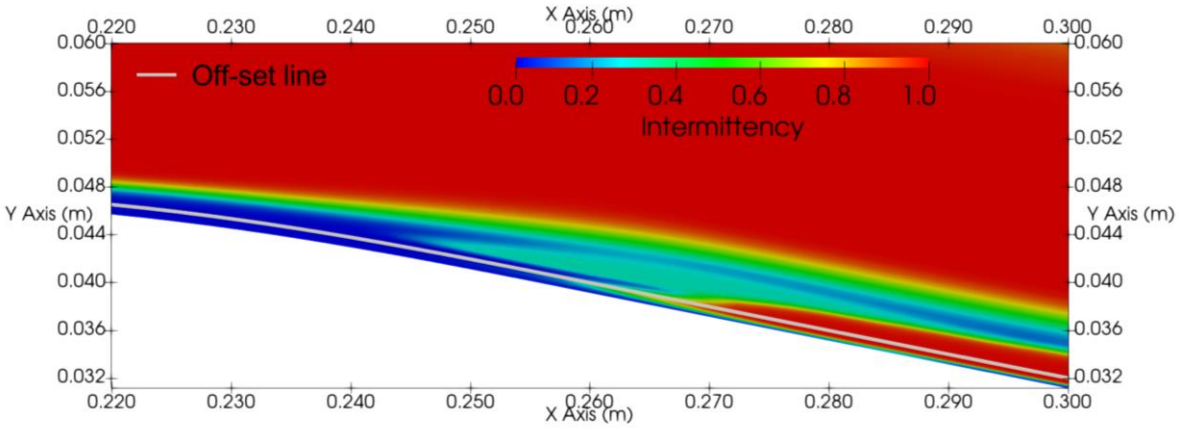

Figure 3.5. The off-set line representation for turbulence intermittency

In this thesis, while the transition onset point is found numerically, it is based on intermittency as described above. However, the results obtained with intermittency and turbulence intensity are very close to each other.

3.3. Computational Fluid Dynamics Study

In this section, pre-process of CFD analyses are examined in detail. Pointwise program for mesh generation, fluid simulation software ANSYS Fluent for solution, open source ParaView software for post processing, MATLAB software for both pre and post processing studies was used in numerical studies.

3.3.1. Geometry and Boundary Conditions

The type of airfoil for which CFD analysis is performed is the NREL's S809 airfoil. Airfoil coordinate data was taken from [41] and scaled to have the desired chord length. The coordinates of the S809 airfoil, which are used as geometry input in CFD analysis, are given in Appendix A1. The geometry is shown in the Figure 3.6.

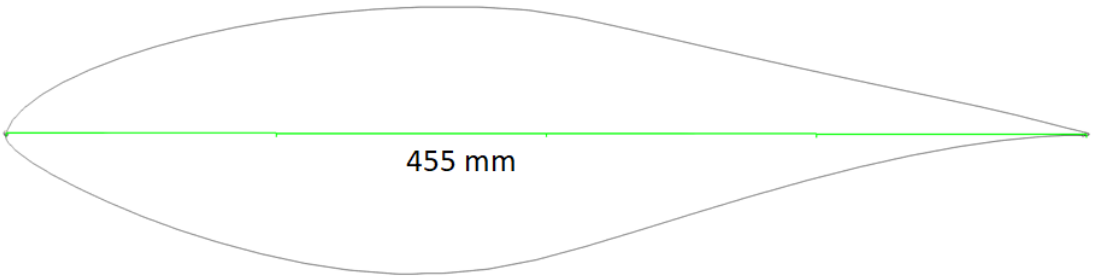

Figure 3.6. S809 airfoil geometry

As seen in the Figure 3.7, O-type domain is used for an optimal cell count compared to other type of domains and is therefore being computationally cost effective [38]. The computational domain radius is adjusted to be 20 times the characteristic length so that it is large enough to minimize the effects of flow between the airfoil model and the boundaries. As boundary conditions, velocity inlet boundary condition, pressure outlet boundary condition and wall boundary condition are used for inlet, outlet and airfoil wall respectively and are shown in Figure 3.7. While performing CFD analysis of each case, velocity and pressure as boundary conditions, density and viscosity values as material properties were taken from Table 2.3. In addition, the model surface was modeled with no-slip condition, simulations were carried out in steady state.

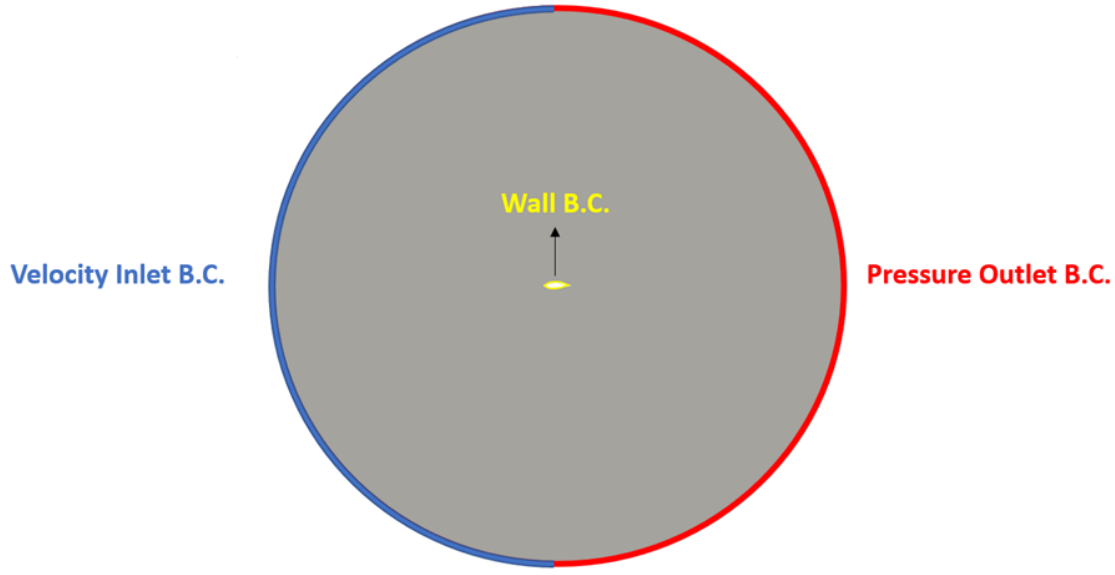

Figure 3.7. Boundary Conditions, not to scale

3.3.2. Mesh Independency Study and Mesh Properties

Grid sensitivity analyzes were performed to obtain grid size independent results before using the mesh for numerical simulation. In this thesis, seven different fluid domain grids are examined to decide the optimum grid size with acceptable accuracy.

Angle of attack 0° and Reynolds number 5×10^5 were determined as the base case of the thesis. Mesh independency studies were made on this main case given in Table 3.1. Moreover, transition SST was used as the turbulence model for this mesh sensitivity study.

Table 3.1. Mesh independency case properties

AoA (◦)	0
Re_desired	500000
Re_actual	500208
Velocity (m/s)	18.8
Mach	0.055
Pressure (Pa)	91741
Density (kg/m^3)	1.06
Dynamic Viscosity (Pa.s)	1.81724E-05

In Table 3.2, mesh properties are given from coarse to fine mesh structure. Change of the mesh structure is achieved by increasing the surface division number of the airfoil model and decreasing the cell thickness growth rate, while the first layer thickness is constant. In addition, for boundary layer grid modelling, the first point of the surface is chosen such that the y+ value is 1.0.

Table 3.2. Mesh size properties for different meshes

Meshes	Total Cell Number	Surface Division	Growth Rate	First Layer Thichness (m)	Desired Yplus
1	7448	50	1.15		
2	11248	75	1.15		
3	22648	150	1.15		
4	45448	300	1.15	**3.71979E-05**	**1**
5	**106786**	**500**	**1.1**		
6	160286	750	1.1		
7	320786	1500	1.1		

The view of the examined mesh 1, 2, 3, 4, 5, 6, 7 from the same point of view is given in Figure 3.8. As clearly seen from these photos, the mesh fineness increases from mesh 1 to 7.

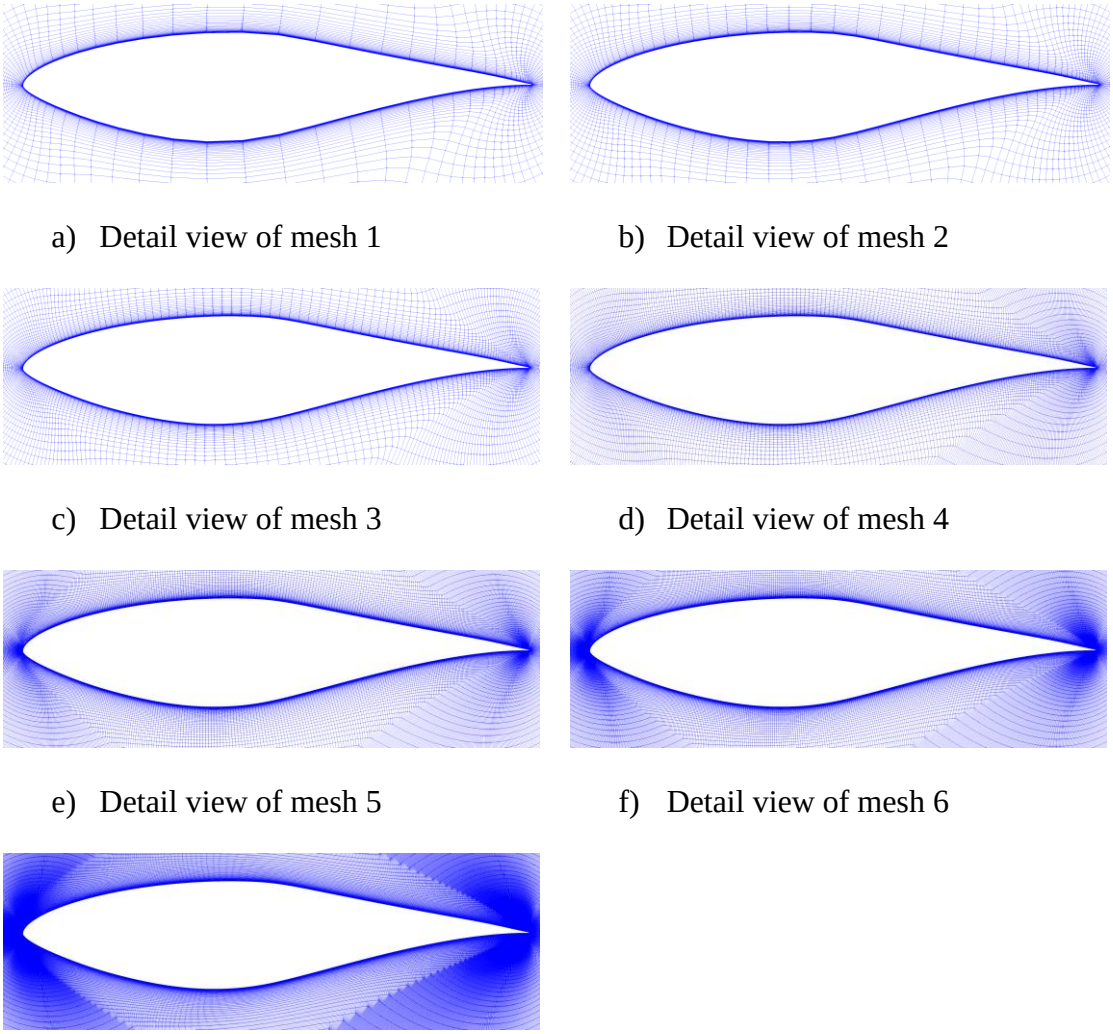

a) Detail view of mesh 1

b) Detail view of mesh 2

c) Detail view of mesh 3

d) Detail view of mesh 4

e) Detail view of mesh 5

f) Detail view of mesh 6

g) Detail view of mesh 7

Figure 3.8. Detail view of meshes

The mesh independency study is conducted for separation point, transition onset point, reattachment point and velocity magnitude for a chosen probe location. For determining these points, as explained in detail in the Section 3.2, skin friction and intermittency values are needed. Thus, these values are plotted against chordwise position of top of the airfoil as shown in Figure 3.9 and Figure 3.10 which represents the skin friction coefficient and intermittency for mentioned meshes respectively.

As the total cell number increases, the results in the following graphs converge. Particularly, it can be observed that the results are approximately the same for mesh 5, mesh 6, and mesh 7.

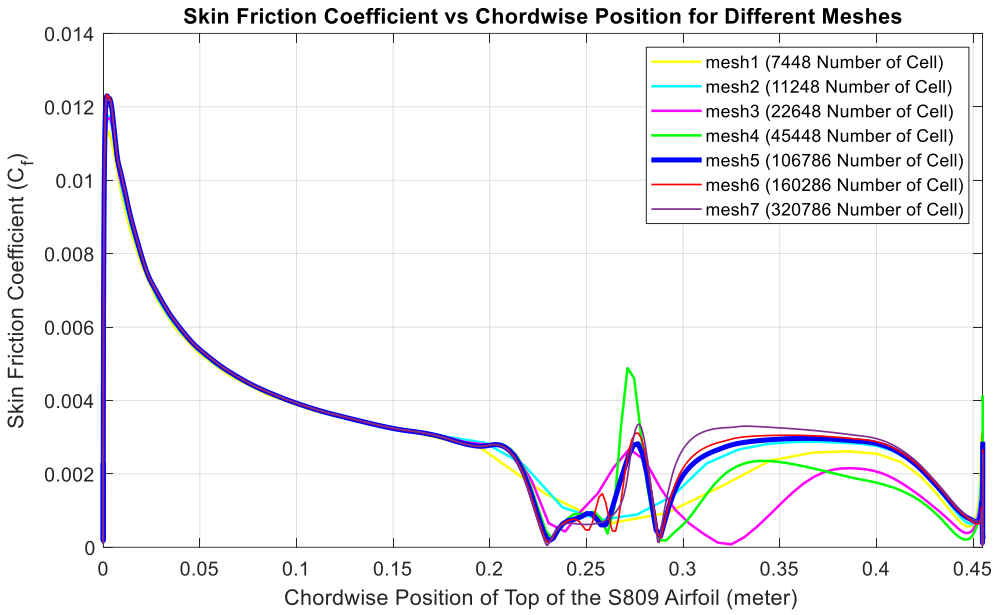

Figure 3.9. Skin friction coefficient vs chordwise position for different meshes for base case (AoA = 0° & Re = 5×10^5)

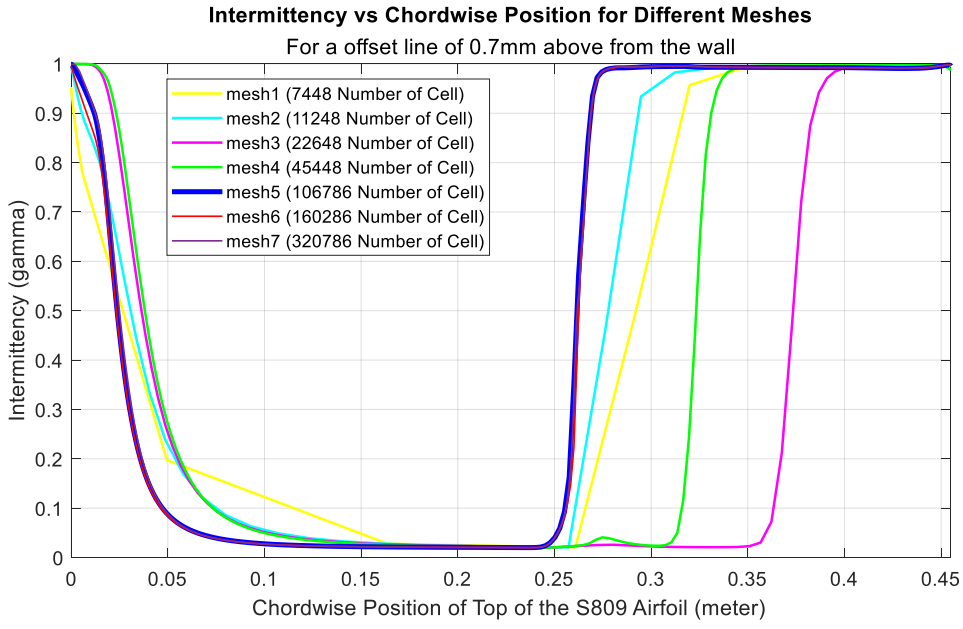

Figure 3.10. Intermittency vs chordwise position for different meshes for base case (AoA = 0° & Re = 5×10^5)

As shown Figure 3.11, it can be observed that for all mesh structures, y+ values are below 1 in critical regions.

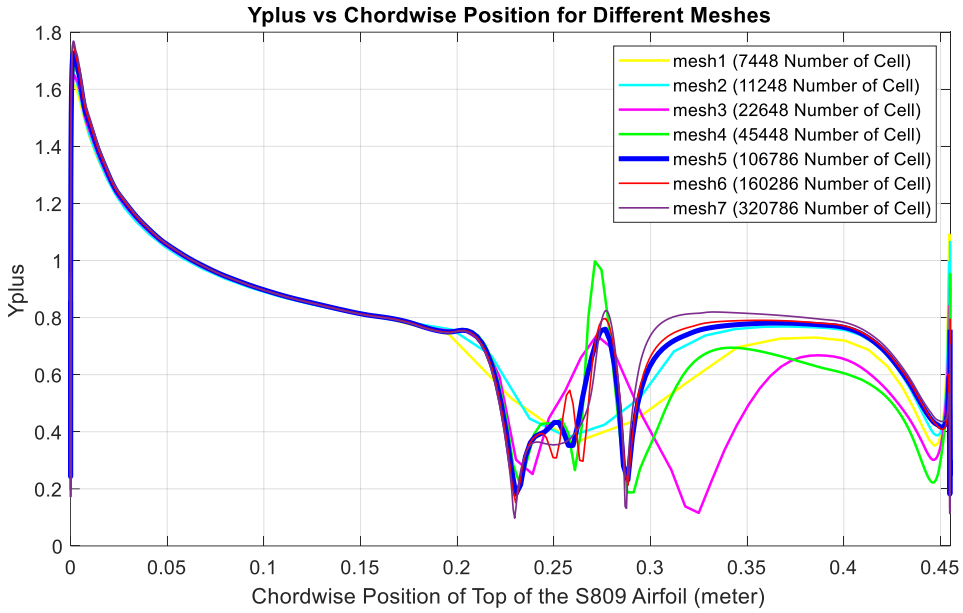

Figure 3.11. Yplus vs chordwise position for different meshes for base case (AoA = 0° & Re = 5×10^5)

In Figure 3.12, graphs of chordwise position of separation, transition, reattachment points are given for different mesh numbers. There is also the velocity magnitude at a point with coordinates [0.2700 m, 0.03825 m] with respect to the leading edge as origin is presented for different meshes. As seen in the graph below, there is not a significant change in the values for mesh 5 and beyond. Therefore, based on the mesh independence study, it has been decided to use mesh 5 as it is advantageous in terms of computational cost.

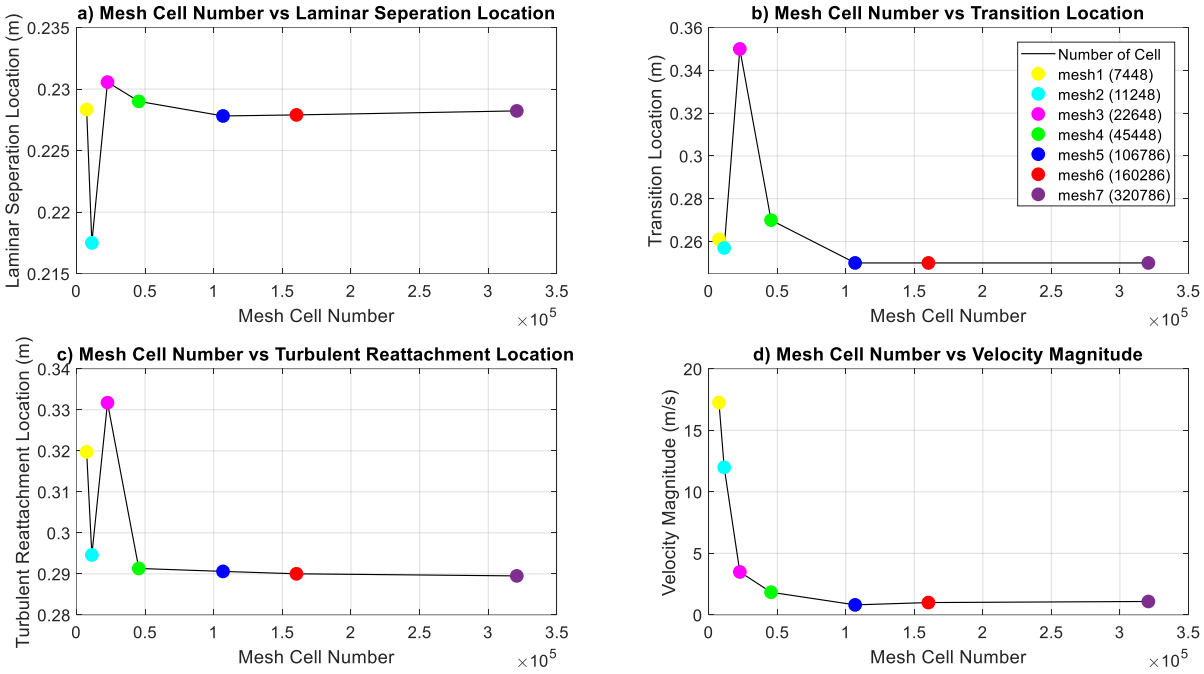

Figure 3.12. Mesh independency graphs

In Figure 3.13 general view of the selected mesh 5 are given. In Figure 3.14 detailed views of LE and TE of the mesh 5 are given.

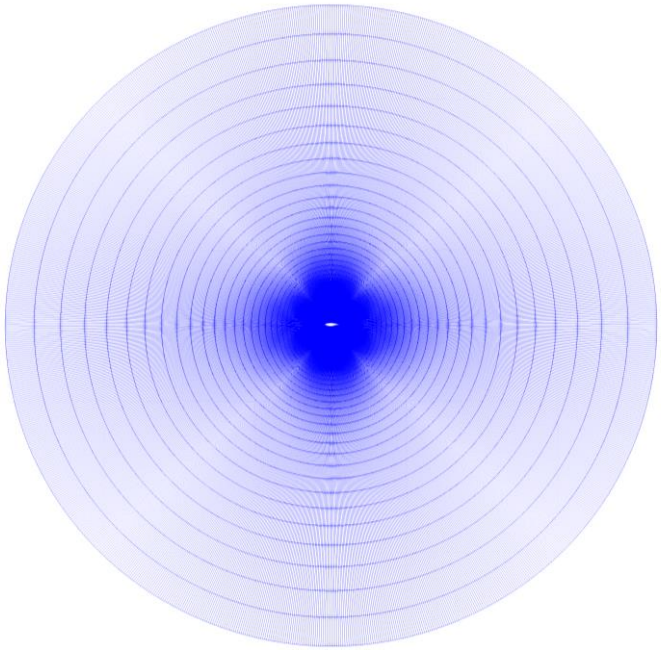

Figure 3.13. General view of selected mesh 5

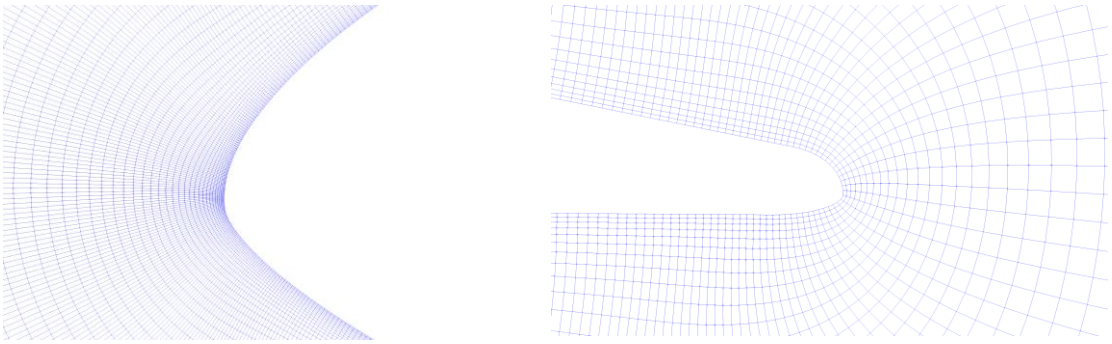

a) LE view of selected mesh 5 b) TE view of selected mesh 5

Figure 3.14. LE and TE view of selected mesh 5

After conducting the mesh independency study for the angle of attack 0° and Reynolds number 5×10^5 base case, meshes created for other cases created with similar mesh properties. Case selection for CFD analysis explained in detail in the Section 2.6.

As given in the Table 3.3 surface division number and growth rate properties for all cases are the same as for mesh 5. Therefore, the total mesh numbers for each case could be different. But the mesh qualities do not differ much for each case. However, since the Reynolds number and angle of attack for the cases are different, mesh structures with different first layer thicknesses emerged for the same desired y+ value. Therefore, the total mesh numbers for each case could be different. But the mesh qualities do not differ much for each case.

Table 3.3. Mesh size properties for different cases

Case	Total Cell Number	Surface Division	Growth Rate	First Layer Thichness (m)	Desired Yplus
3	106786	500	1.1	3.71979E-05	1
5	107784			3.18571E-05	
7	109780			2.70883E-05	
9	106786			3.71979E-05	
10	106786			3.66766E-05	
11	106786			3.66981E-05	
12	106786			3.72544E-05	

4. RESULTS AND DISCUSSIONS

4.1. Experimental Results

The results of the experimental studies, are given in this part. The wind tunnel, wing model, IR camera, experimental setup and test matrix details were already explained in Section 2.

In Figure 4.1, a sample image taken from the FLIR C2 camera used as IR thermography tool is shared. In this image, the incoming hot flow moves from right to left, in other words from LE to TE of the airfoil model. On the right of the image there is a colorbar expressing the surface temperature in °C. Generally, dark colors represent cold areas and light colors represent warm areas.

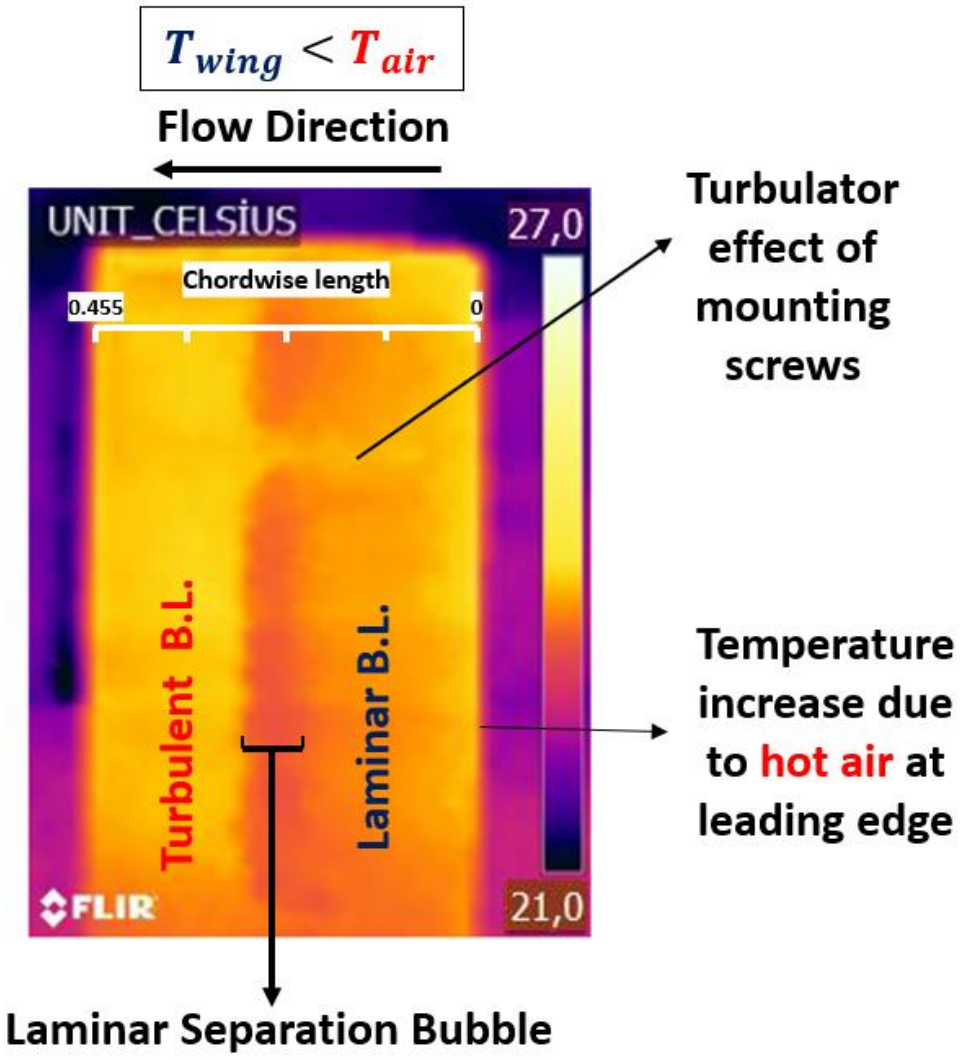

Figure 4.1. General layout in IR thermography images

4.1.1. Effects of Reynolds Number at Constant Angle of Attack

In this section, the results of the experimental studies to examine the effect of the change of the Reynolds number for the fixed 0° angle attack on the chordwise position of the separation, transition and reattachment points on the airfoil are given. In Table 4.1, there are temperature, pressure, density, viscosity information recorded in the tunnel datalog for each case during the experiment. The data was used as input for CFD analysis, as mentioned in the Section 2.6.

Table 4.1. Test conditions for constant angle of attack cases

Case	AoA (°)	Re_desired	Re_actual	Velocity (m/s)
1	0	400000	395860	14.8
2	0	450000	465313	17.5
3	0	500000	500208	18.8
4	0	550000	545235	20.5
5	0	600000	594042	22.3
6	0	650000	653603	24.6
7	0	700000	714120	26.9
8	0	750000	743644	28.1

In Figure 4.2, IR images taken at 50000 intervals from 400000 to 750000 Reynolds numbers for 0° angle of attack are represented. As can be seen from the IR photographs, as the Reynolds number increases, the hot and cold areas become clearer, but it is difficult to see a noticeable change in the locations of these areas. For this reason, the airfoil surface temperature in the chordwise direction and its derivative with respect to chordwise position for Re = 5×10^5, 6×10^5 and 7×10^5 are given in the Figure 4.3, Figure 4.4 and Figure 4.5. In figures, the blue line represents the airfoil surface temperature in the chordwise direction, and the red line represents the derivative of temperature with respect to chordwise position. In these graphs, the points where the temperature gradient is minimum, maximum and local maximum temperature are also indicated.

As a note, the flow direction is from right to left in Figure 4.2, while in the Figure 4.3, Figure 4.4 and Figure 4.5 the flow is from left to right in order to make comparison readily with the CFD results. In Figure 4.3, the square marker represents the separation point, the round marker represents the transition on set point, and the triangular marker represents the reattachment point.

Additionally, the wedge-shaped light-colored area seen in all cases in Figure 4.2 is formed by the turbulator effect created by the mounting screws.

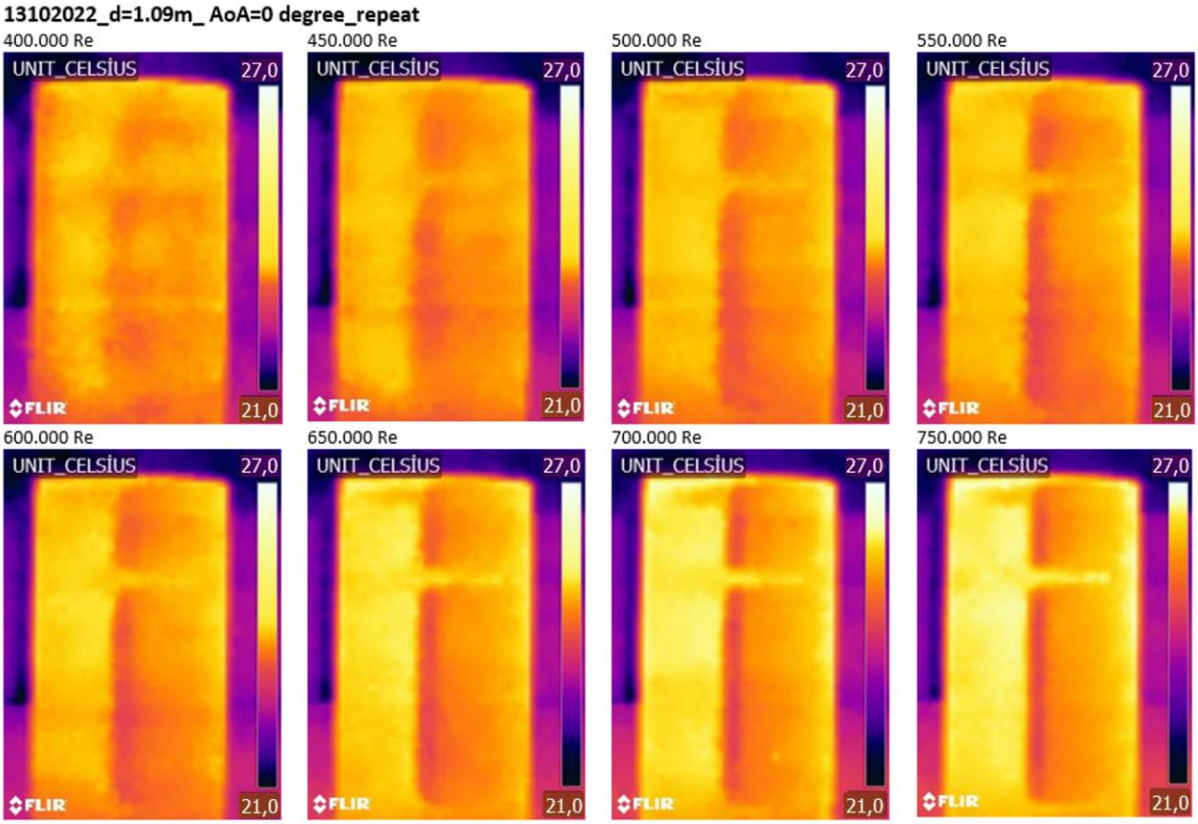

Figure 4.2. IR images for AoA = 0° cases

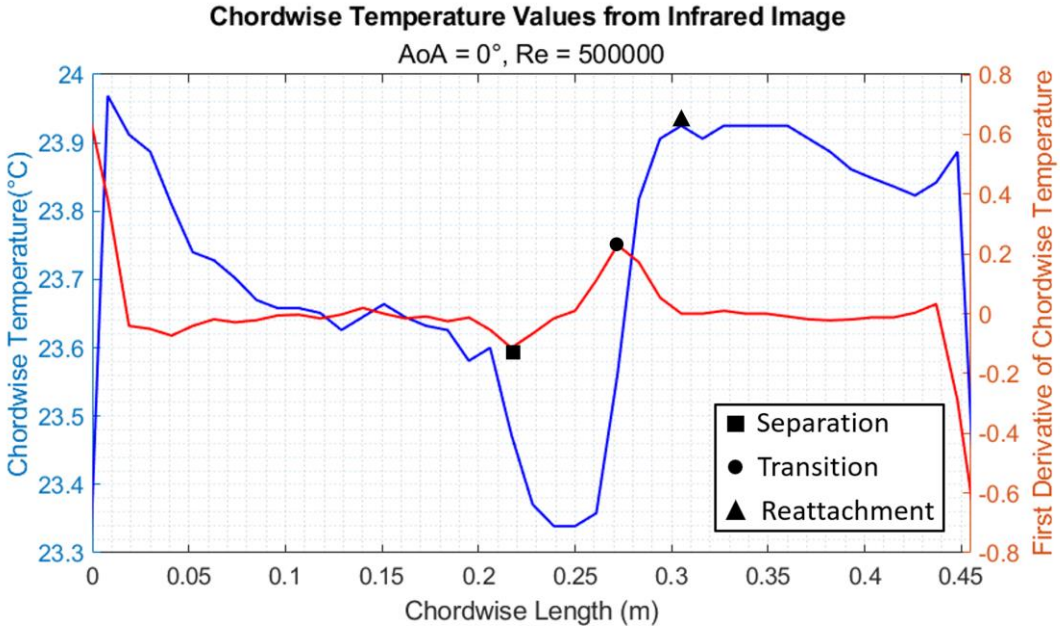

Figure 4.3. Chordwise temperature values for AoA = 0° & Re = 5×10^5 case

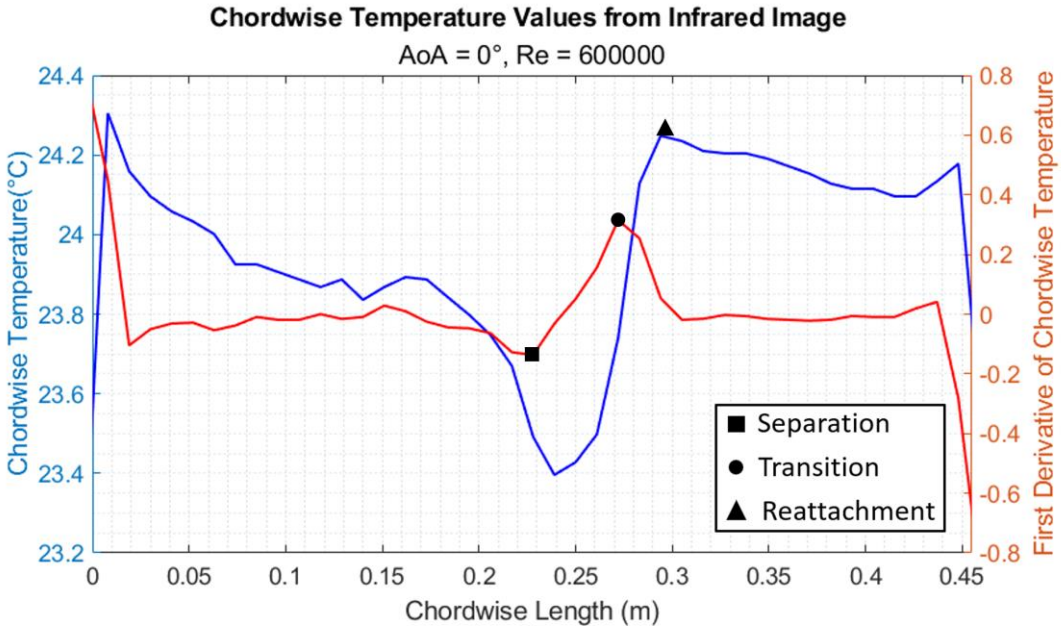

Figure 4.4. Chordwise temperature values for AoA = 0° & Re = 6×10^5 case

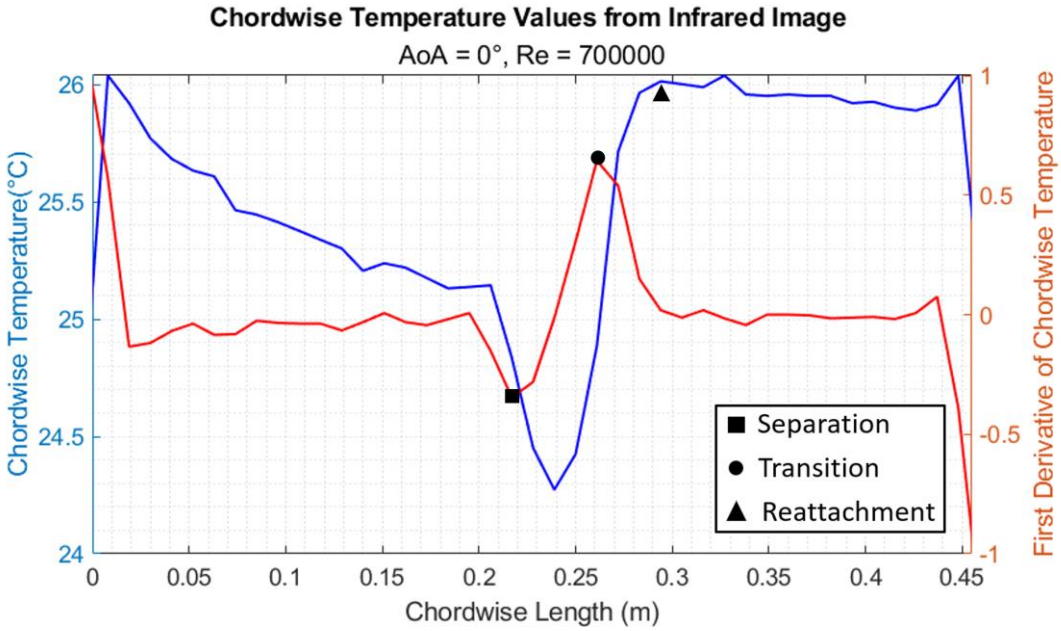

Figure 4.5. Chordwise temperature values for AoA = 0° & Re = 7×10^5 case

Figure 4.3, Figure 4.4 and Figure 4.5 represent the selected cases, i.e., 5×10^5, 6×10^5 and 7×10^5 Reynolds number cases for 0° angle of attack. For all cases, the separation, transition and reattachment point values obtained from the graphs above are given in the Table 4.2.

Table 4.2. Experimental results for AoA = 0° cases

Case	Re_desired	Separation (m)	Transition (m)	Reattachment (m)
1	400000	**	**	**
2	450000	0.206	0.283	0.338
3	500000	0.217	0.272	0.305
4	550000	0.217	0.272	0.294
5	600000	0.217	0.272	0.294
6	650000	0.217	0.272	0.294
7	700000	0.217	0.261	0.294
8	750000	0.217	0.261	0.294

For the first case, since the velocity was very low for the 400000 Reynolds number, there was no significant change in the temperature gradient, so this case can be considered as one in which separation and transition did not occur. In cases with a Reynolds number of 450000 and larger, there are significant changes in temperature and its derivative. An increase in the Reynolds number by the order of 50000 does not cause a significant change in the position of the separation and reattachment point, but causes a little change in the position of the transition point. The expected result is that the position of the transition point gradually approaches the LE of the airfoil with the increase of the Reynolds number. The reason for the undetectably small change could be that the velocity variation is not significantly high.

4.1.2. Effects of Angle of Attack at Constant Reynolds Number

In this section, the results of the experimental studies to examine the effect of the change of the angle of attack for the fixed 5×10^5 Reynolds number on the chordwise position of the separation, transition and reattachment points on the airfoil are given. Similar with the previous section, in Table 4.3, there are temperature, pressure, density, viscosity information recorded in the tunnel datalog for each case during the experiment.

Table 4.3. Test conditions for constant Reynolds number cases

Case	AoA (°)	Re_desired	Re_actual	Velocity (m/s)
9	0	500000	500208	18.8
10	3	500000	499401	18.3
11	6	500000	501544	18.5
12	9	500000	497443	18.6
13	12	500000	503703	18.9

In Figure 4.6, IR images taken at 3° intervals from 0° to 12° angle of attacks for 5×10^5 Reynolds number are represented. During the tests, the environment to which the wing is exposed is highly transient. As a result, experiment conditions, incoming air temperature and airfoil surface temperature distributions are different for different angles of attack. This situation can be understood from scales of the colorbars in Figure 4.6. However, it is possible to examine each case in terms of separation and transition point position in its own temperature range.

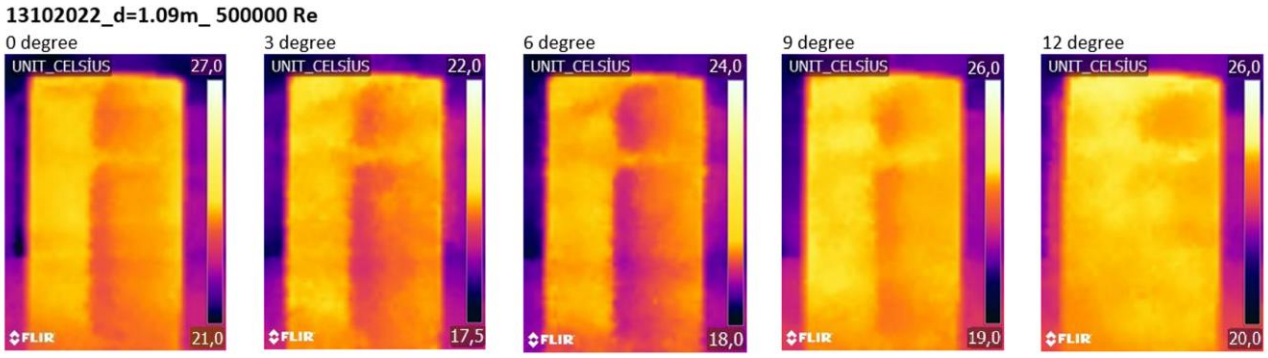

Figure 4.6. IR images for Re = 5×10^5 cases

As can be seen from the above IR photographs, as the angle of attack increases, it is difficult to see a noticeable change in the locations of hot and cold areas. Therefore, again the airfoil surface temperature in the chordwise direction and its derivative with respect to chordwise position for the cases are given in the Figure 4.7, Figure 4.8 and Figure 4.9. In these graphs, the points where the temperature gradient is minimum, maximum and local maximum temperature can be clearly seen.

Nevertheless, since the entire surface of the airfoil color is light yellow, that is, warm, it can be predicted from the IR image that the 12° angle of attack case is directly in turbulent flow.

As a note, the flow direction is from right to left in Figure 4.6, while in the Figure 4.7, Figure 4.8 and Figure 4.9 the flow is from left to right in order to make comparison readily with the CFD results.

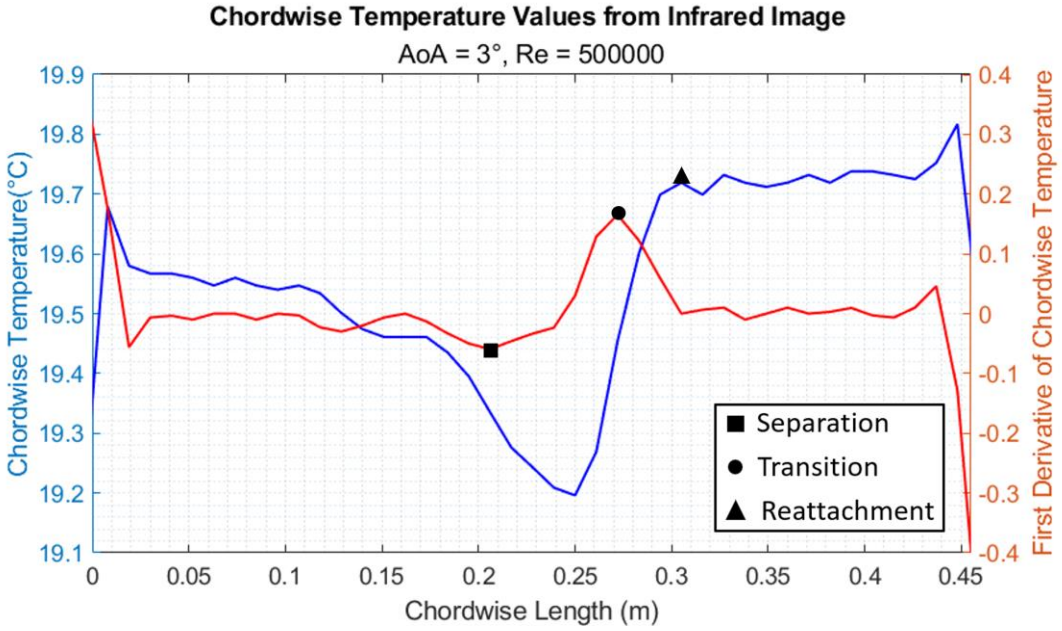

Figure 4.7. Chordwise temperature values for AoA = 3° & Re = 5×10^5 case

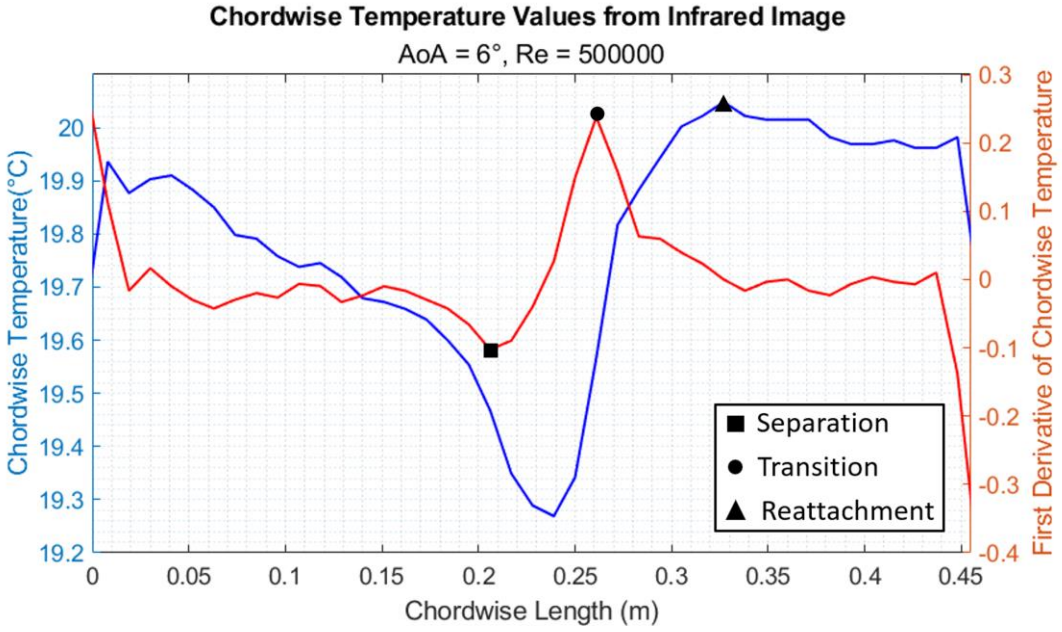

Figure 4.8. Chordwise temperature values for AoA = 6° & Re = 5×10^5 case

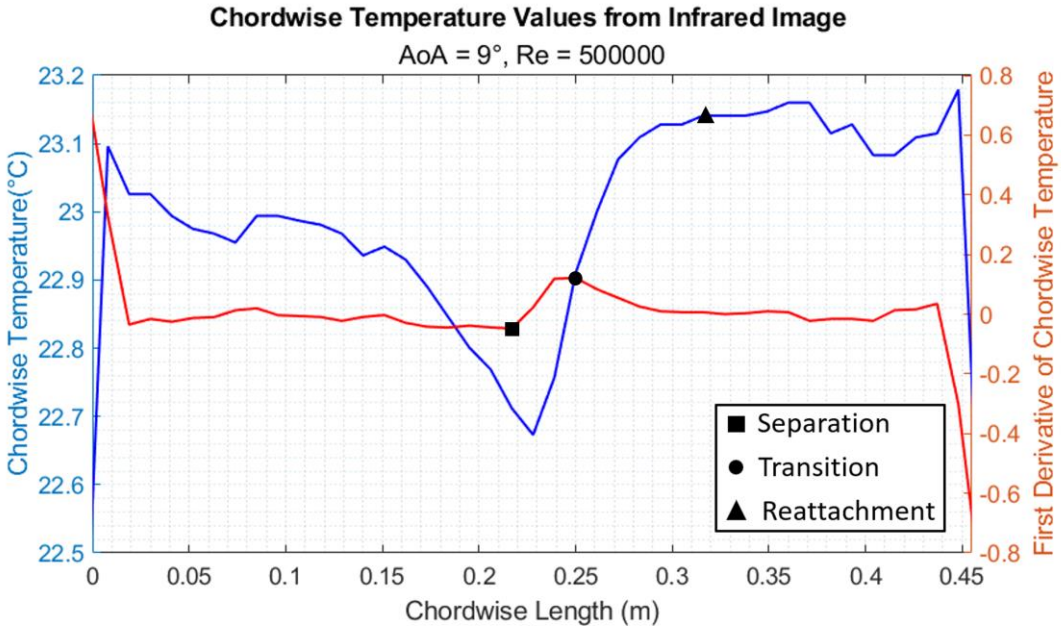

Figure 4.9. Chordwise temperature values for AoA = 9° & Re = 5×10^5 case

Figure 4.3, Figure 4.7, Figure 4.8 and Figure 4.9 represent the selected cases, i.e., 0°, 3°, 6°, 9° angle of attack for 5×10^5 Reynolds number. For all cases, the separation, transition and reattachment point values obtained from the graphs above are given in the Table 4.4.

Table 4.4. Experimental results for Re = 5×10^5 cases

Case	AoA (°)	Separation (m)	Transition (m)	Reattachment (m)
9	0	0.217	0.272	0.305
10	3	0.206	0.270	0.305
11	6	0.206	0.261	0.327
12	9	0.217	0.250	0.338
13	12	**	**	**

As expected, it can be considered that there is no separation bubble and it can be said that turbulent flow occurs immediately after LE of the airfoil, as there is no significant change in temperature gradient in the case of 12° angle of attack.

Re = 5×10^5 and 0°, 3°, 6°, 9° angle of attack cases were examined and it was found that the chordwise position of the transition point approaches the LE of the airfoil respectively as the angle of attack is increased. However, it is difficult to say that there is a change trend for the separation point. On the other hand, as the angle of attack increases, the reattachment point chordwise location gets closer to the TE of the airfoil indicating that separation bubble expands.

4.1.3. Effects of Transition Strip

In this section, the results of the experiments performed by adding the transition strip with constant angle of attack and different Reynolds number cases are given. In aerodynamic experiments, a transition strip refers to a small strip or tape that is attached to the surface of an airfoil. The purpose of using a transition strip is to simulate the natural transition of the boundary layer that occurs in real-world conditions. In certain aerodynamic testing scenarios, maintaining a laminar boundary layer flow is desired to study specific flow characteristics or to achieve better performance. However, in many practical applications, the boundary layer transitions to turbulent flow due to various factors such as surface roughness, pressure gradients, or disturbances.

In this thesis, a paper-thick zigzag tape was used as the transition strip and was mounted approximately 8 cm from the LE of the airfoil. The length of the tape is 13 cm and the width is 1 cm.

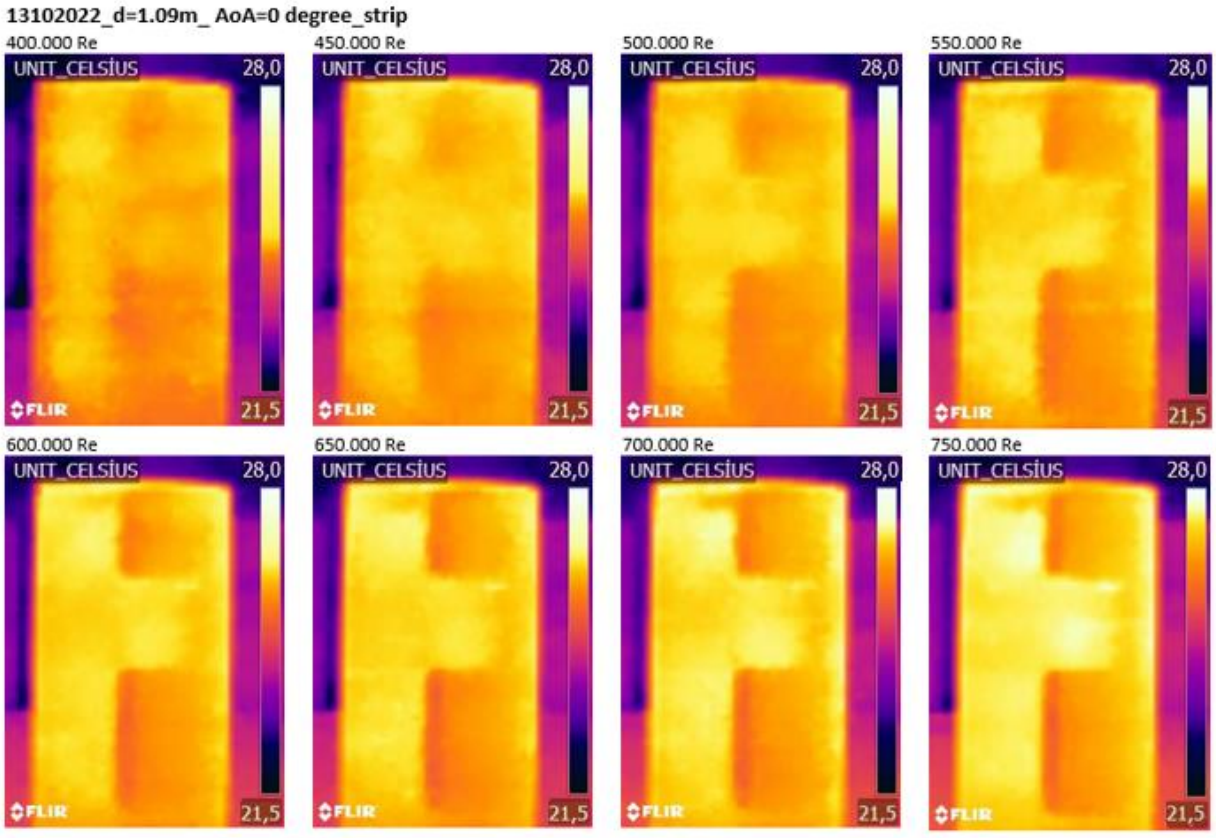

Figure 4.10. IR images for AoA = 0° cases at different Reynolds numbers with transition strip

In Figure 4.10, IR images taken at 50000 intervals from 400000 to 750000 Reynolds numbers for 0° angle of attack with transition strip are presented. As the Reynolds number increases, the hot and cold areas on the surface of the wing appear more clearly.

The effect of the transition strip also increases with Reynolds number. The transition strip acts as a vortex generator, accelerating the transition process, making the flow immediately turbulent.

In order to observe the effect of the transition strip in more detail, the non-tape mounted and mounted cases are given in Figure 4.11 and Figure 4.12 for Reynolds number 5×10^5 and 7×10^5, respectively. As clearly seen in the IR images below in the area where the transition strip is installed, the transition was triggered, and the flow became turbulent. Due to the rapid onset of turbulence in the area where the transition strip is installed, the incoming airflow heated the airfoil more, resulting in that particular area appearing yellow in color. As the Reynolds number increases, this effect becomes more pronounced, and as observed in Figure 4.12, color differences are visually more apparent.

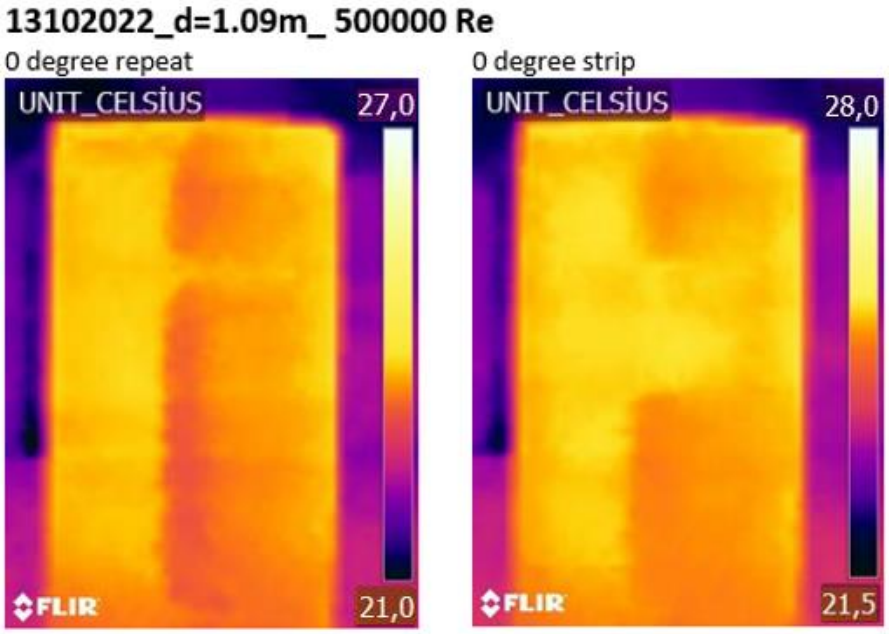

Figure 4.11. IR images for AoA = 0° & Re = 5×10^5 case with transition strip

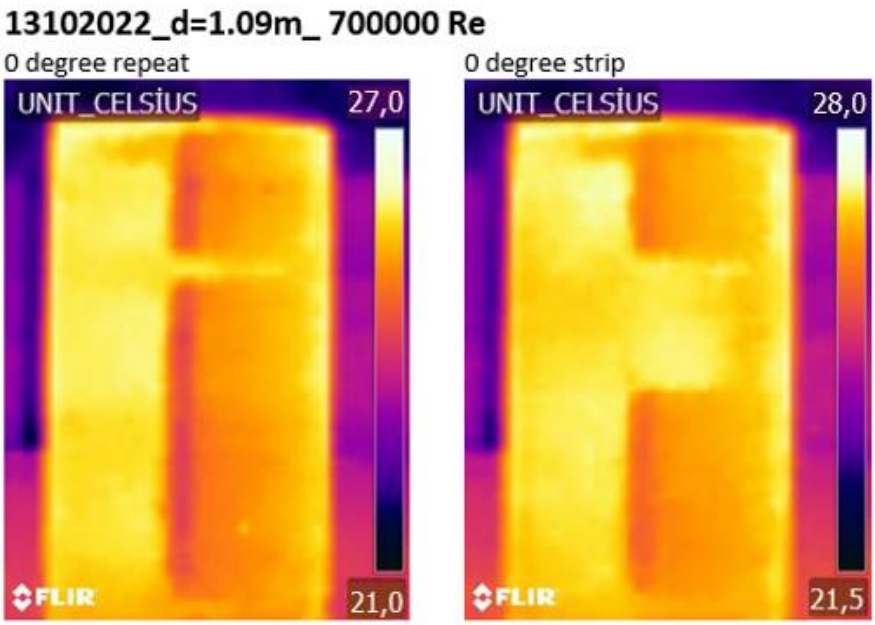

Figure 4.12. IR images for AoA = 0° & Re = 7×10^5 case with transition strip

The visual effects of the transition strip are given in Figure 4.11 and Figure 4.12, and their numerical values are provided in Figure 4.13 and Figure 4.14, respectively.

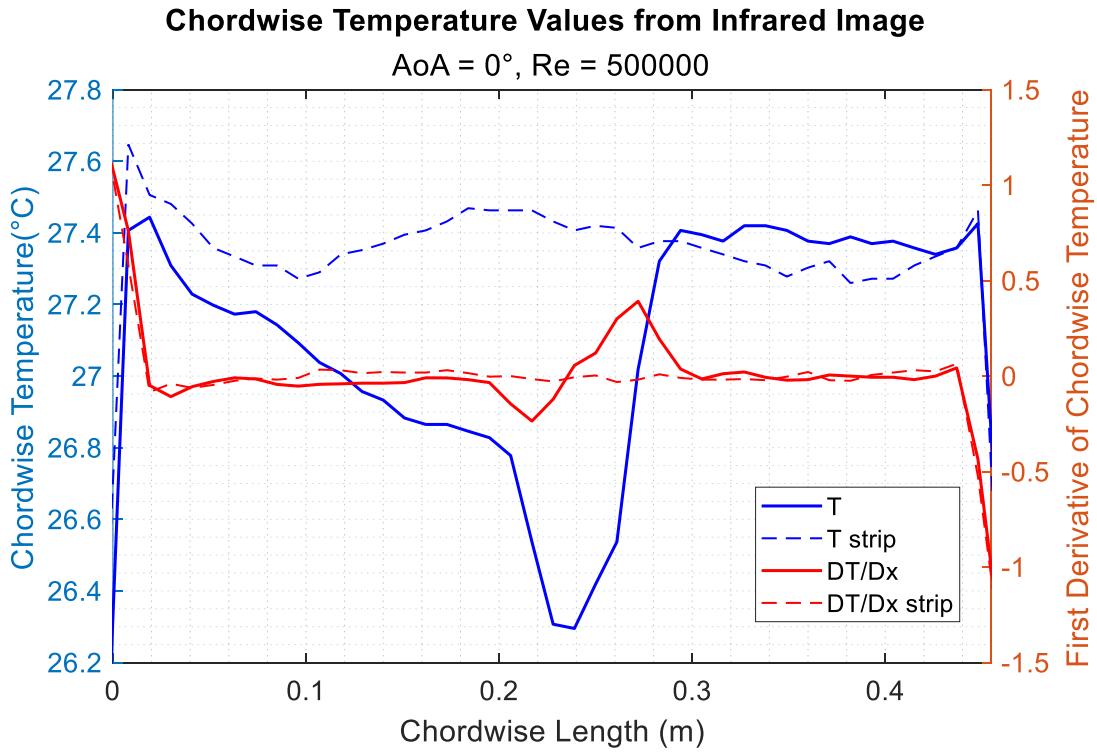

Figure 4.13. Transition strip effect for AoA = 0° & Re = 5×10^5 case

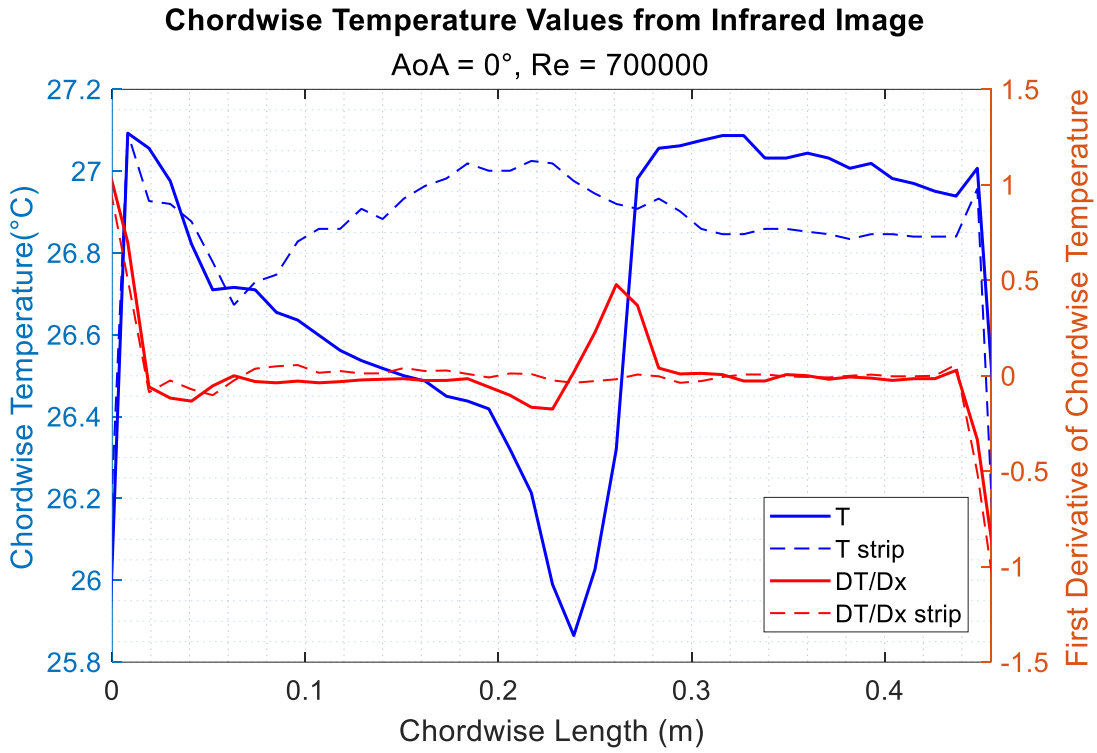

Figure 4.14. Transition strip effect for AoA = 0° & Re = 7×10^5 case

The numerical impact of the transition strip can be observed in the temperature and temperature derivative graphs above. The solid lines in the graphs represent the data obtained from the area without the transition strip, while the dashed lines represent the data obtained from the area with the transition strip installed. In the area without the transition strip, the separation, transition, and reattachment points are clearly observed in the temperature and temperature derivative. However, in the area with the transition strip installed, due to the rapid onset of turbulent flow, these points are not clearly visible.

4.2. Numerical Results

The results of the numerical studies are given in this part. Theorical background of CFD, governing equations, turbulence and transition models are presented in Section 3.1. Pre-process of CFD and preliminary analyzes including mesh independency are also given in Section 3. In this section, turbulence model studies, the CFD analysis of the experimental cases and the results obtained from the post-processing will be discussed.

4.2.1. Turbulence Model Study

In this section, turbulence models embedded in ANSYS Fluent software are examined for the angle of attack 0° and Reynolds number 5×10^5 main case. The equations of the transition and turbulence models are provided in detail in Section 3.1.2. Here, $k-\omega-\gamma$ transition, transition $k-kl-\omega$ and transition SST models are used as transition flow models, which is the main focus. The standard $k-\varepsilon$ model was used as reference turbulence model.

Figure 4.15 presents the variation of the skin friction coefficient with respect to the chordwise position of the airfoil. The detection of separation and reattachment points from the skin friction coefficient graph is explained in Section 3.2.1. According to the graph, transition models effectively capture the separation and reattachment points, while the $k-\varepsilon$ turbulence model provides inconsistent results.

In Figure 4.16 and Figure 4.17, the variation of turbulence intensity and intermittency values with respect to the chordwise position of the airfoil is presented. The detection of transition from the turbulence intensity and intermittency graphs is explained in Section 3.2.2. In the numerical simulations conducted in this thesis, the transition onset point was determined using the intermittency value. However, since the Fluent program does not provide the intermittency value for the $k-\varepsilon$ turbulence model and the transition $k-kl-\omega$ model, the turbulence intensity graph is also included. The Transition SST and $k-\omega-\gamma$ models were compared for both turbulence intensity and intermittency, and it was observed that they yielded similar results for the transition points. Both models provided results for turbulence intensity and intermittency, and the transition points were found to be very close using both methods.

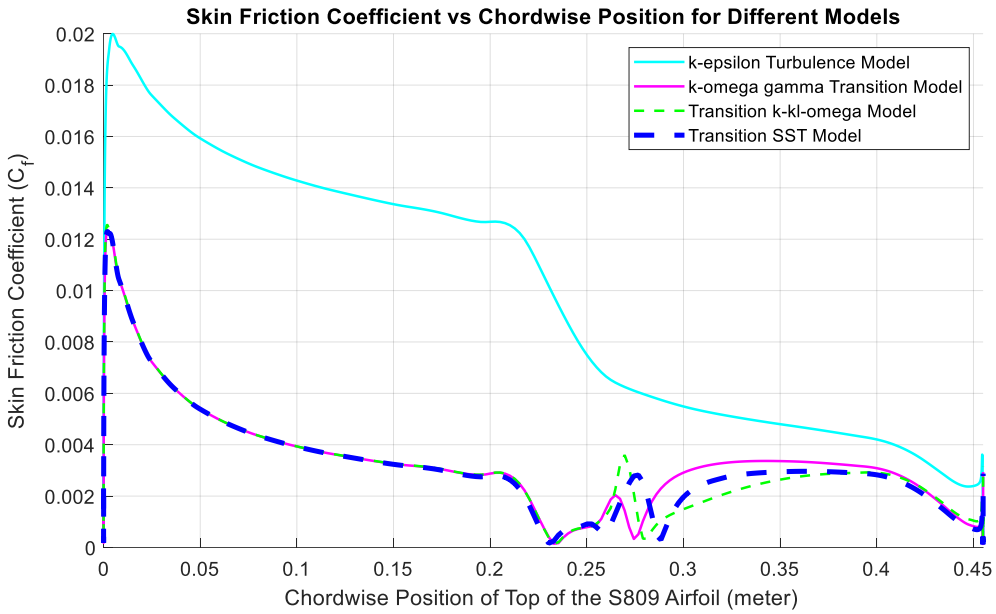

Figure 4.15. Skin friction coefficient vs chordwise position for different turbulence models for AoA = 0° & Re = 5×10^5 case

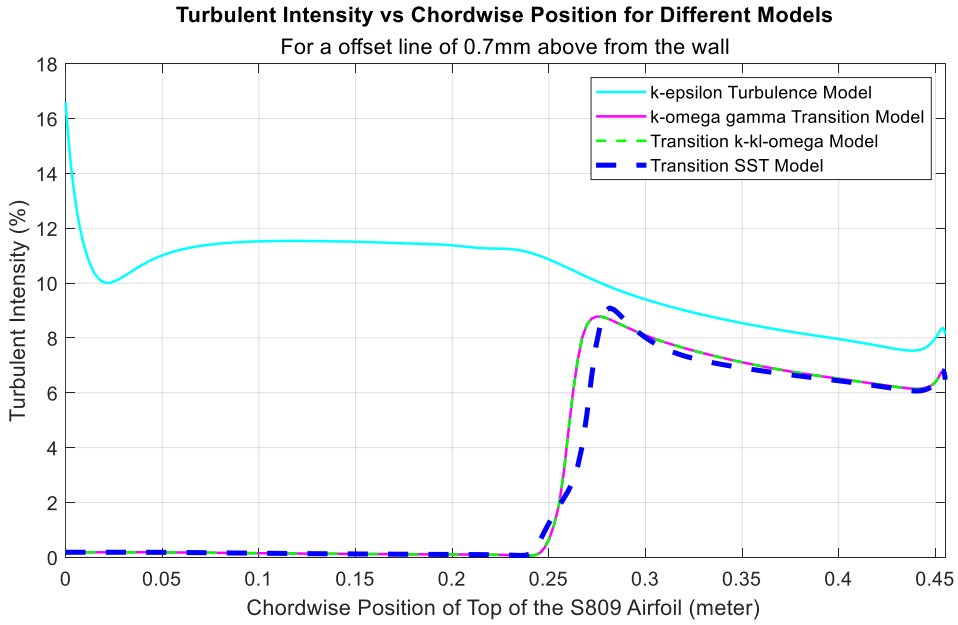

Figure 4.16. Turbulence intensity vs chordwise position for different turbulence models for AoA = 0° & Re = 5×10^5 case

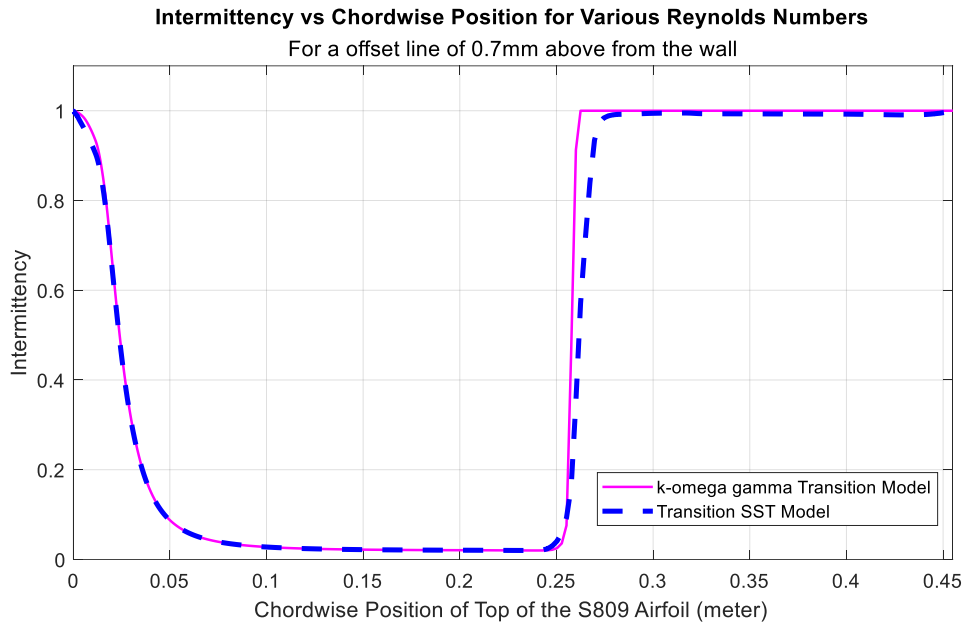

Figure 4.17. Intermittency vs chordwise position for different turbulence models for AoA = 0° & Re = 5×10^5 case

Note that, $k-\varepsilon$ turbulence model cannot predict separation and transition flow observed in the graphs above. In Figure 4.15, Figure 4.16 and Figure 4.17 skin friction coefficient, turbulence intensity and intermittency value changes with chordwise position are given for different turbulence models, respectively. In Table 4.5, the numerical results of these graphs are provided.

Table 4.5. Model selection for AoA = 0° & Re = 5×10^5 case

Transition Models	Separation (m)	Transition (m)	Reattachment (m)
$k-\omega-\gamma$ Transition	0.230	0.250	0.276
Transition $k-kl-\omega$	0.230	0.245	0.281
Transition SST	**0.227**	**0.250**	**0.290**

The positions of the separation, transition and reattachment points on the chord of the airfoil model are given for the models in the table above. It can be noted that the transition models yield similar results for the separation, transition and reattachment points.

In this thesis, it was decided to continue CFD analyses with the transition SST model for comparison with the experimental results, as it utilizes four equations.

4.2.2. Effects of Reynolds Number at Constant Angle of Attack

In this section, the results of the numerical studies to examine the effect of the change of the Reynolds number for the fixed 0° angle attack on the chordwise position of the separation, transition and reattachment points on the airfoil are given. The CFD analysis performed with the Transition SST model and numerical results are given in Table 4.6.

Table 4.6. CFD results for constant angle of attack cases

Test Conditions				Transition SST		
Case	AoA (°)	Re_desired	Re_actual	Separation (m)	Transition (m)	Reattachment (m)
3	0	500000	500208	0.227	0.250	0.290
5	0	600000	594042	0.227	0.250	0.283
7	0	700000	714120	0.227	0.250	0.279

In Figure 4.18 and Figure 4.19 skin friction coefficient and intermittency values are given on the airfoil in the chordwise direction, respectively. In the graphs, the blue color line represents 5×10^5, the green color line represents 6×10^5, and the pink color represents 7×10^5 Reynolds number for 0° angle of attack.

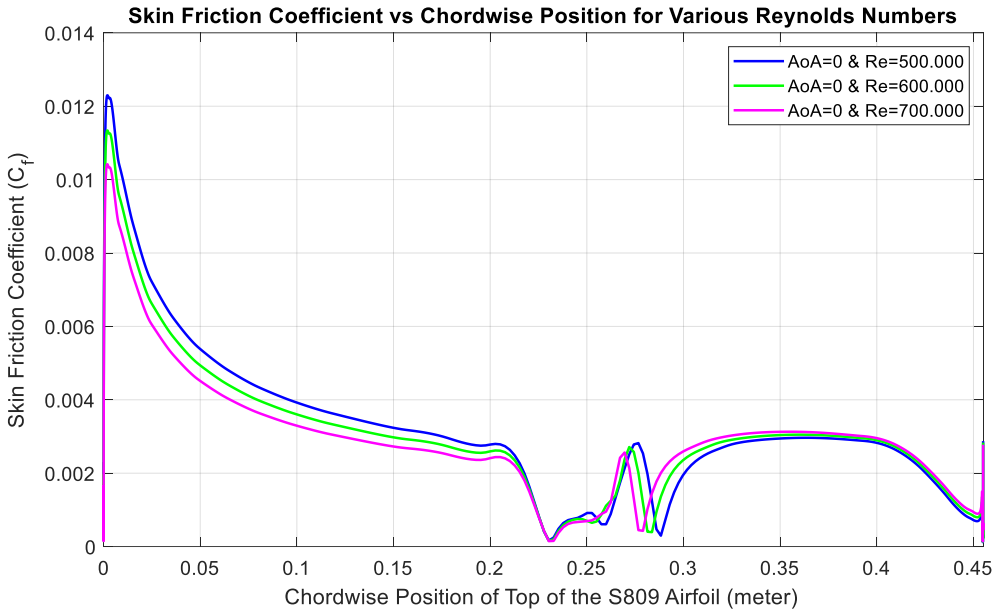

Figure 4.18. Skin friction coefficient vs chordwise position for constant angle of attack cases

The detection of separation and reattachment points from the skin friction coefficient graph is explained in Section 3.2.1. It can be observed from Figure 4.18 and the data in Table 4.6 that the separation points are quite close for Reynolds numbers 5×10^5, 6×10^5, 7×10^5 for 0° angle of attack. On the other hand, it can be said that the reattachment point approaches the LE of the airfoil. From these results, it can be inferred that the size of the separation bubble increases as the velocity increases.

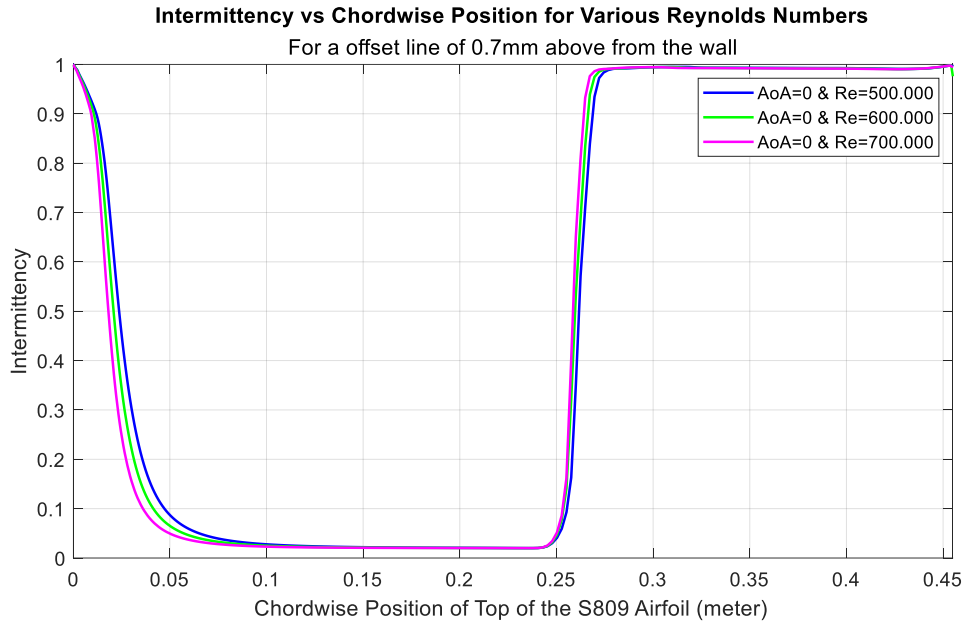

Figure 4.19. Intermittency vs chordwise position for constant angle of attack cases

The detection of transition from the intermittency graphs is explained in Section 3.2.2. It can be observed from Figure 4.19 that the separation points are quite close for Reynolds numbers 5×10^5, 6×10^5, 7×10^5 for 0° angle of attack.

4.2.3. Effects of Angle of Attack at Constant Reynolds Number

In this section, the results of the numerical studies to examine the effect of the change of the angle of attack for the fixed 5×10^5 Reynolds number on the chordwise position of the separation, transition and reattachment points on the airfoil are given. The CFD analysis performed with the Transition SST model and numerical results are given in Table 4.7.

Table 4.7. CFD results for constant Reynolds number cases

Test Conditions				Transition SST		
Case	AoA (°)	Re_desired	Re_actual	Separation (m)	Transition (m)	Reattachment (m)
9	0	500000	500208	0.227	0.250	0.290
10	3	500000	499401	0.224	0.243	0.282
11	6	500000	501544	0.223	0.236	0.274
12	9	500000	497443	0.195	0.227	0.269

In Figure 4.20 and Figure 4.21 skin friction coefficient and turbulent intensity values are given on the airfoil in the chordwise direction, respectively. In the graphs, the blue color line represents 0°, the green color line represents 3°, the pink color represents 6° and the turquoise color line represents 9° angle of attack for 5×10^5 Reynolds number.

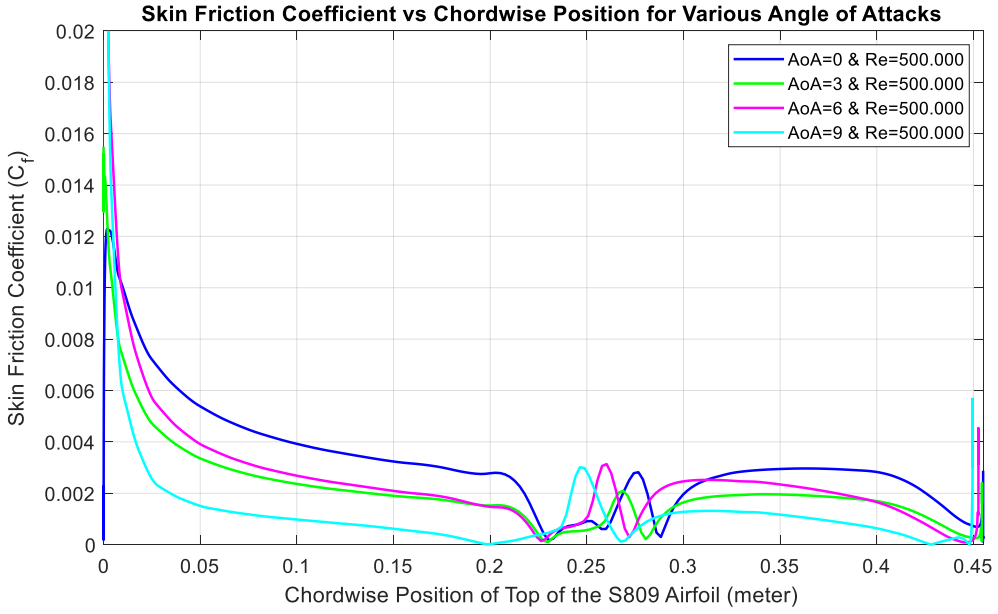

Figure 4.20. Skin friction coefficient vs chordwise position for constant Reynolds number cases

The detection of separation and reattachment points from the skin friction coefficient graph is explained in Section 3.2.1. From the skin friction graph above and the data in Table 4.7, it can be observed that as the angle increases from 0° to 6°, the separation point slightly approaches the LE of the airfoil. However, at 9° angle of attack, the separation point has approached the LE of the airfoil with a larger increase. The same conclusions apply to the reattachment point as well.

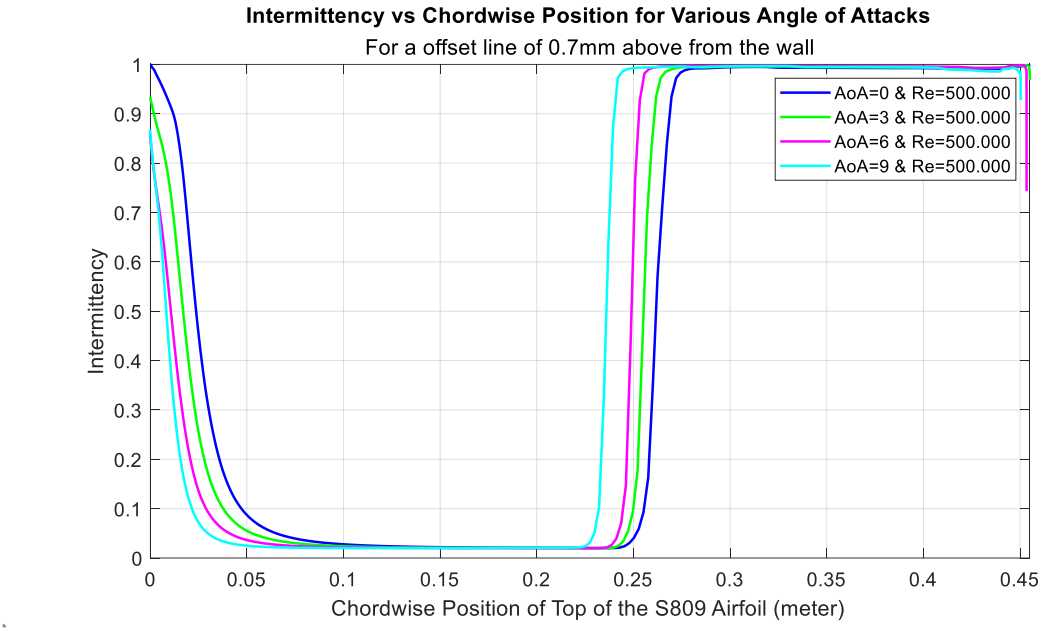

Figure 4.21. Intermittency vs chordwise position for constant Reynolds number cases

The detection of transition from the intermittency graphs is explained in Section 3.2.2. As seen in Figure 4.21, the transition onset point approaches the LE of the airfoil slightly as the angle of attack increases.

4.3. Comparison of Experimental and Numerical Results

In this section, the experimental and numerical results, which are the most important results of the thesis, are summarized in the Table 4.8.

Table 4.8. Experimental vs numerical results

Test Conditions			Experimental Results			CFD Transition SST Results		
Case	AoA	Re_desired	Separation (m)	Transition (m)	Reattachment (m)	Separation (m)	Transition (m)	Reattachment (m)
3	0	500000	0.217	0.272	0.305	0.227	0.250	0.290
5	0	600000	0.217	0.272	0.294	0.227	0.250	0.283
7	0	700000	0.217	0.261	0.294	0.227	0.250	0.279
9	0	500000	0.217	0.272	0.305	0.227	0.250	0.290
10	3	500000	0.206	0.270	0.305	0.224	0.243	0.282
11	6	500000	0.206	0.261	0.327	0.223	0.236	0.274
12	9	500000	0.217	0.250	0.338	0.195	0.227	0.269

For constant 0° angle of attack, different Reynolds number cases, it is clearly seen from Figure 4.22 the separation point does not change much according to the Reynolds number at constant angle of attack. The chordwise position of the separation point is 0.21 m in the experimental results, while it is 0.22 m in the CFD results. Experimental and numeric studies are consistent for the separation point for constant angle of attack, different Reynolds number cases.

For constant 0° angle of attack, different Reynolds number cases the chordwise position of the transition onset point is 0.25 m in the numerical results. Here, again, no significant change was observed at the transition onset point according to the Reynolds number. On the other hand, for the same cases, the chordwise position of the transition onset point is approximately 0.27 m in the experimental results. Although there is a difference of about 0.02 m between the experimental and numeric results in these cases, it follows the same trend. Only for case AoA = 0° & Re = 7×10^5 transition was observed to be 0.26 with little decrease in test results.

For constant 0° angle of attack, different Reynolds number cases the reattachment point slightly approached the LE of airfoil as the velocity increased. In these cases, experimental and numeric results are also quite compatible.

The low magnitude of Reynolds number in this case had a minimal impact on the chordwise position of the separation bubble and transition onset point at 0° fixed angle of attack.

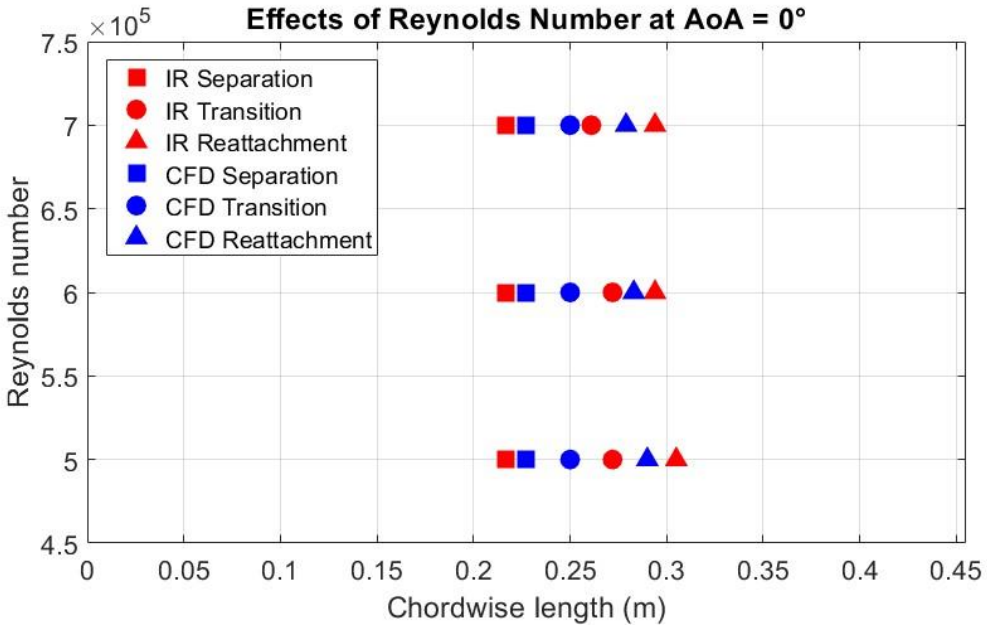

Figure 4.22. Experimental and numerical results for constant angle of attack cases

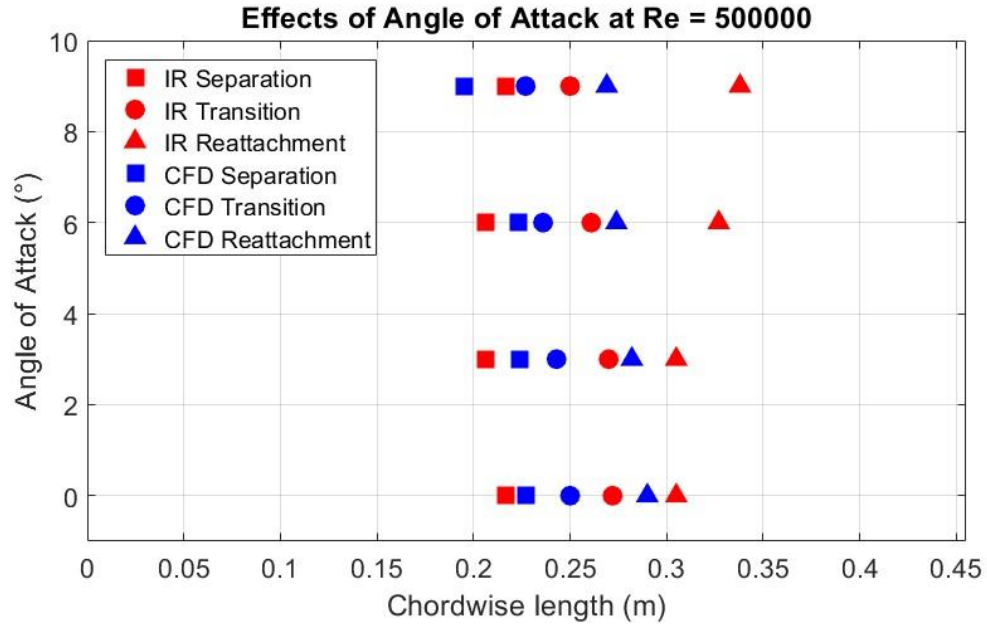

Figure 4.23. Experimental and numerical results for constant Reynolds number cases

For 5×10^5 constant Reynolds number, different angle of attack cases, as seen in the Figure 4.23 separation point gets closer to LE of airfoil as the angle of attack increases in the numerical results. In the experimental results, for the same conditions, it seems that the separation point moves slightly away from the LE for 9° angle of attack, and this result is not very logical. This result is most likely an error due to the measurement during the experiment and this small difference is within the uncertainty limits of the IR camera. The numerical results are more reasonable and it can be said that the separation point gets closer to the LE of airfoil slightly as the angle of attack increases at a constant speed.

For 5×10^5 constant Reynolds number, different angle of attack cases, it is clearly observed in both experimental and numeric results that the transition onset point approaches LE of airfoil as the angle increases. The average difference between the transition onset points in the experimental and numerical results is approximately 0.2 m and the variations with respect to the angle of attack are also consistent with each other.

For 5×10^5 constant Reynolds number, different angle of attack cases, numeric and experimental studies yielded slightly different results for the reattachment point. As the angle of attack increases, it is expected that the separation bubble, and so the reattachment point, will shift towards LE of the airfoil [56]. Therefore, it can be said that numerical results are more reliable in this case. The reason for the inconsistency in the results of IR thermography may be attributed to the methodology [9] used, which might have been specifically designed for different Reynolds numbers and not applicable to different angles of attack.

5. CONCLUSION

5.1. General Conclusions

Within the scope of this thesis, transition flow determination experiments were performed using infrared thermography method. Numerical studies were also carried out, different mesh and turbulence models were used in the analysis. The results of the experimental and numerical studies, which are the two complementary parts of this thesis, are mentioned in detail in the Section 4.

The conclusions reached in the experimental part of this study are:

- IR images were obtained where the areas of separation, transition, and reattachment on the airfoil model could be distinguished using an infrared camera. The infrared images were post-processed to convert them into numerical data, and the chordwise positions of the separation, transition, and reattachment points were determined. The proof was provided that the IR thermography method can be effectively utilized in similar scenarios.
- As the Reynolds number changes within the range of 5×10^5, 6×10^5, 7×10^5 at AoA = 0°; the change in the separation point could not be observed, the transition onset point approached slightly towards the LE of the airfoil, and the reattachment point also approached the LE.
- As the angle of attach changes within the range of 0°, 3°, 6°, 9° at Re = 5×10^5; the chordwise position of the transition onset point approached the LE of the airfoil.

The conclusions reached in the numerical part of this study are:

- The CFD results enabled the identification of separation and reattachment points along with the corresponding skin friction values. When defining the transition onset, the intermittency parameter was used, but similar results were obtained when using turbulence intensity.
- Standard $k-\varepsilon$ turbulence model cannot predict separation, transition onset and reattachment points.

- $k-\omega-gamma$ transition, transition $k-kl-\omega$ and transition SST models provided very close results in determining the chordwise positions of the separation, transition, and reattachment points.
- As the Reynolds number changes within the range of 5×10^5, 6×10^5, 7×10^5 at AoA = 0°; the chordwise position of the separation and transition onset points did not change on the airfoil, while the reattachment point approached the LE of the airfoil
- As the angle of attach changes within the range of 0°, 3°, 6° at Re = 5×10^5; the chordwise position of the separation and transition onset point slightly approaches the LE of the airfoil.
- As the angle of attach changes between the range of 6° and 9° at Re = 5×10^5; the chordwise position of the separation and transition onset point has approached the LE of the airfoil with a larger increase.

In general, experimental and numerical results are compatible. Especially the change trends of the transition onset points are quite compatible. For the constant angle of attack cases, since the order of Reynolds number magnitude does not change much, the chordwise position of the transition onset point also does not change. But the chordwise position of the transition onset point approaches LE of airfoil as the angle of attack increases in the constant Reynolds number cases.

5.2. Recommendations for Further Research

Additional studies are required in order to improve the results obtained within the scope of the thesis and increase their accuracy. First of all, to increase the accuracy of infrared thermography experiments, tests can be performed with a high-tech camera with a higher IR resolution.

The experiments included in this study were performed in test section 2 of METUWIND with a maximum speed of 26 m/s. For this reason, 5×10^5, 6×10^5 and 7×10^5 Reynolds numbers could be tested in this study. Since the orders of these Reynolds numbers are not very high, the effect of the Reynolds number on the variation of separation, transition and reattachment points could not be observed. To examine the effect of Reynolds number over a wider range, a new test set-up can be established in test section 1 of METUWIND with a maximum speed of 80 m/s. The set-up to be used in test section 1 must have structural durability at high speeds.

Another note is that the angle sweep can be performed at more frequent intervals, such as 1°. Thus, it can be observed more clearly at which angle the flow completely separates.

REFERENCES

[1] Cengel Y. and Cimbala, J. (2006). Fluid mechanics: Fundamentals and Applications. McGraw-Hill Education.

[2] Di Pasquale D., Rona A., & Garrett S.J. (2009). A Selective Review of Transition Modelling for CFD. 39th AIAA Fluid Dynamics Conference. doi: 10.2514/6.2009-3812

[3] Gül, M. (2013). An Experimental study on boundary layer separation control over s809 airfoil using synthetic jet actuators [M.S. - Master of Science]. Middle East Technical University.

[4] Jelínek, T. (2018). Experimental Investigation of the Boundary Layer Transition on a Laminar Airfoil Using Infrared Thermography. EPJ Web of Conferences, 180, 02040. doi: 10.1051/epjconf/201818002040

[5] Marinus, B. G., Vercauteren, J., Vandenberghe, R., & Smeulders, J. (2020). Laminar-Turbulent Transition on a Cambered NACA 16-009 Airfoil at Low Speed. International Review of Mechanical Engineering (IREME), 14(6), 351. doi: 10.15866/ireme.v14i6.17788

[6] Munson B.R., Young D.F., Okiishi T.H., Huebsch W.W. (2009). Fundamentals of Fluid Mechanics. McGraw-Hill Education.

[7] Özçakmak, Ö. S., Sørensen, N. N., Madsen, H. A., & Sørensen, J. N. (2019). Laminar-turbulent transition detection on airfoils by high-frequency microphone measurements. Wind Energy, 22(10), 1356–1370. doi: 10.1002/we.2361

[8] Schlichting, H. (1979). Boundary-layer theory. MacGraw-Hill.

[9] Wynnychuk, D. W., & Yarusevych, S. (2020). Characterization of Laminar Separation Bubbles Using Infrared Thermography. AIAA Journal, 58(7), 2831–2843. doi: 10.2514/1.j059160

[10] Wolfe, W., Ochs, S., Wolfe, W., & Ochs, S. (1997). CFD calculations of S809 Aerodynamic Characteristics. 35th Aerospace Sciences Meeting and Exhibit. doi: 10.2514/6.1997-973

[11] Che Sidik, N., Yusuf, S., Asako, Y., Mohamed, S., & Aziz Japa, W. (2020). A Short Review on RANS Turbulence Models. CFD Letters, 12(11), 83-96. doi: 10.37934/cfdl.12.11.8396

[12] Lopes, R., Eça, L., & Vaz, G. (2020). On the Numerical Behavior of RANS-Based Transition Models. Journal Of Fluids Engineering, 142(5). doi: 10.1115/1.4045576

[13] Walters, D., & Cokljat, D. (2008). A Three-Equation Eddy-Viscosity Model for Reynolds-Averaged Navier–Stokes Simulations of Transitional Flow. Journal Of Fluids Engineering, 130(12). doi: 10.1115/1.2979230

[14] Menter, F., Langtry, R., Likki, S., Suzen, Y., Huang, P., & Völker, S. (2006). A Correlation-Based Transition Model Using Local Variables—Part I: Model Formulation. Journal Of Turbomachinery, 128(3), 413. doi: 10.1115/1.2184352

[15] Wilcox, D. C. (2006). Turbulence modeling for CFD. DCW Industries.

[16] Bergman, T. L., & Incropera, F. P. (2011). Fundamentals of heat and mass transfer. J. Wiley.

[17] W. Frei, (2013) "Which turbulence model should i choose for my cfd application?" 2013

[18] Horton, H. P. 1968 Laminar Separation Bubbles in Two and Three Dimensional Incompressible Flow. PhD thesis, University of London.

[19] Gartenberg, E., & Roberts, A. S. (1992). Twenty-five years of aerodynamic research with infrared imaging. Journal of Aircraft, 29(2), 161–171. https://doi.org/10.2514/3.46140

[20] *tunelbilgi.pdf.* Rüzgem (METUWIND) Center for Wind Energy Research. (n.d.). Retrieved January 9, 2023, from https://ruzgem.metu.edu.tr/en/

[21] Rüzgem (METUWIND) Center for Wind Energy Research. Experimental Aerodynamics Laboratory | RÜZGEM (METUWIND) Center For Wind Energy Research. (n.d.). Retrieved January 9, 2023, from https://ruzgem.metu.edu.tr/en/experimental-aerodynamics-laboratory#WTC5

[22] FLIR C2. Support for C2 | Teledyne FLIR. (n.d.). Retrieved October 1, 2022, from https://www.flir.eu/support/products/c2/

[23] Katopodes, N.D. (2019) "Turbulent flow," Free-Surface Flow, pp. 566–650. Available at: https://doi.org/10.1016/b978-0-12-815489-2.00008-3.

[24] Gestione. (2022, April 2). Turbulence models in CFD - rans, DES, Les and DNS. Ideal Simulations. Retrieved January 28, 2023, from https://www.idealsimulations.com/resources/turbulence-models-in-cfd/

[25] Ferziger J.H., Perić M., "Computational Methods for Fluid Dynamics", Springer, 3rd Edition.

[26] Piomelli, U. and Chasnov, J.R. (1996) "Large-eddy simulations: Theory and applications," Turbulence and Transition Modelling, pp. 269–336. Available at: https://doi.org/10.1007/978-94-015-8666-5_7.

[27] Deck, S. et al. (2014) “High-fidelity simulations of Unsteady Civil Aircraft Aerodynamics: Stakes and perspectives. application of zonal detached eddy simulation,” Philosophical Transactions of the Royal Society A: Mathematical, Physical and Engineering Sciences, 372(2022), p. 20130325. Available at: https://doi.org/10.1098/rsta.2013.0325.

[28] Schmitt, F.G. (2007), "About Boussinesq’s turbulent viscosity hypothesis: historical remarks and a direct evaluation of its validity". Comptes Rendus Mecanique, 335 ((9 10)): 617-627.

[29] Boussinesq, J. (1877), "Essai sur la theorie des eaux courantes". Memoires presentes par divers savants a l’Academie des Sciences de l’Institut National de France, Tome XXIII, No 1, Imprimerie Nationale, Paris.

[30] Jones, W.P. and Launder, B.E. (1972), "The Prediction of Laminarization with a Two-Equation Model of Turbulence". International Journal of Heat and Mass Transfer, Vol. 15, pp. 301-314.

[31] Wilcox, D. C. (1994). Simulation of transition with a two-equation turbulence model. AIAA Journal, 32(2), 247–255. https://doi.org/10.2514/3.59994

[32] Menter, F.R. (1993), "Zonal Two Equation k-w Turbulence Models for Aerodynamic Flows". 24th Fluid Dynamics Conference, Orlando.

[33] Menter, F.R. (1994), "Two-Equation Eddy-Viscosity Turbulence Models for Engineering Applications". AIAA Journal, Vol. 32, No. 8, pp. 1598-1605.

[34] ANSYS. (2022), "Ansys Fluent Theory Guide".

[35] Menter, F. R., Smirnov, P. E., Liu, T., Avancha, R. (2015). A one-equation local correlation-based transition model. Flow, Turbulence and Combustion, 95(4), 583–619. https://doi.org/10.1007/s10494-015-9622-4

[36] D. Keith Walters and Davor Cokljat. "A three-equation eddy-viscosity model for reynolds-averaged navier-stokes simulations of transitional flows". Journal of Fluids Engineering. 130. December 2008.

[37] Langtry, R. B. (2006). A correlation-based transition model using local variables for unstructured parallelized CFD codes, PhD Thesis.

[38] Krishnamurthy, R. (2022) The art and science of meshing airfoil, GridPro Blog. Available at: https://blog.gridpro.com/the-art-and-science-of-meshing-airfoil/ (Accessed: 30 May 2023).

[39] Picard, A, Davis, RS, Glaser, M, Fujii, K, 2008, 'Revised formula for the density of moist air (CIPM-2007)', Metrologia, vol. 45, no. 2, pp. 149-155. DOI: http://dx.doi.org/10.1088/0026-1394/45/2/004

[40] Tsilingiris, P, 2008, 'Thermophysical and transport properties of humid air at temperature range between 0 and 100°C', Energy Conversion and Management, vol. 49, no. 5, pp.1098-1110. DOI: https://doi.org/10.1016/j.enconman.2007.09.015

[41] Marshall L. Buhl, J. (n.d.). S809 airfoil shape. NWTC Information Portal. Retrieved January 9, 2023, from https://wind.nrel.gov/airfoils/shapes/s809_shape.html

[42] Spalart, P. R., and Strelets, M. K., "Mechanisms of Transition and Heat Transfer in a Separation Bubble," Journal of Fluid Mechanics, Vol.403, Jan. 2000, pp. 329–349. https://doi.org/10.1017/S0022112099007077

[43] de Luca, L., Carlomagno, G. M., and Buresti, G., "Boundary Layer Diagnostics by Means of an Infrared Scanning Radiometer," Experiments in Fluids, Vol. 9, No. 3, 1990, pp. 121–128. https://doi.org/10.1007/BF00187411

[44] Crawford, B. K., Duncan, G. T.,West, D. E., and Saric,W. S., "Laminar-Turbulent Boundary Layer Transition Imaging Using IR Thermography," Optics and Photonics Journal, Vol. 3, No. 3, 2013, pp. 233–239. https://doi.org/10.4236/opj.2013.33038

[45] Joseph, L. A., Borgoltz, A., and Devenport,W., "Infrared Thermography for Detection of Laminar-Turbulent Transition in Low-SpeedWind Tunnel Testing," Experiments in Fluids, Vol. 57, No. 5, 2016, pp. 1–13. https://doi.org/10.1007/s00348-016-2162-4

[46] Quast, A., "Detection of Transition by Infrared Image Techniques," Technical Soaring, Vol. 30, No. 1, 1987, pp. 33–38.

[47] Dollinger, C., Sorg, M., Balaresque, N., and Fischer, A., "Measurement Uncertainty of IR Thermographic Flow Visualization Measurements for Transition Detection on Wind Turbines in Operation," Experimental Thermal and Fluid Science, Vol. 97, Oct. 2018, pp. 279–289. https://doi.org/10.1016/j.expthermflusci.2018.04.025

[48] Dollinger, C., Balaresque, N., Gaudern, N., Gleichauf, D., Sorg, M., and Fischer, A., "IRThermographic Flow Visualization for the Quantification of Boundary Layer Flow Disturbances Due to the Leading Edge Condition," Renewable Energy, Vol. 138, Aug. 2019, pp. 709–721. https://doi.org/10.1016/j.renene.2019.01.116

[49] Costantini, M., Hein, S., Henne, U., Klein, C., Koch, S., and Schojda, L., "Pressure Gradient and Nonadiabatic Surface Effects on Boundary Layer Transition," AIAA Journal, Vol. 54, No. 11, 2016, pp. 3465– 3480. https://doi.org/10.2514/1.J054583

[50] Ma, D., Zhao, Y., Qiao, Y., Li, G. (2015). Effects of relative thickness on aerodynamic characteristics of airfoil at a low Reynolds number. Chinese Journal of Aeronautics, 28(4), 1003–1015. https://doi.org/10.1016/j.cja.2015.05.012

[51] Sturm, H. et al. (2012) “Boundary layer separation and reattachment detection on airfoils by thermal flow sensors,” Sensors, 12(11), pp. 14292–14306. Available at: https://doi.org/10.3390/s121114292.

[52] Cassandra Konz, S. C. L., Claudia Cornejo Happel, A. D. of C. T. L. E., Dennis Turano, S. A., Greeshma Daniel, S. A., Madison Bigger, S. A., & Leishman, J. G. (n.d.). *Boundary Layers.* Introduction to Aerospace Flight Vehicles. Retrieved April 7, 2023, from https://oer.pressbooks.pub/introductiontoaerospaceflightvehicles/chapter/introduction-to-boundary-layers/

[53] Veerasamy, D. and Atkin, C. (2019) “A rational method for determining intermittency in the transitional boundary layer,” Experiments in Fluids, 61(1). Available at: https://doi.org/10.1007/s00348-019-2856-5.

[54] Walker, G.J., Subroto, P.H. and Platzer, M.F. (1988) “Transition modeling effects on viscous/Inviscid interaction analysis of low Reynolds number airfoil flows involving laminar separation bubbles,” Volume 1: Turbomachinery. Available at: https://doi.org/10.1115/88-gt-32.

[55] Sznajder, J. and Kwiatkowski, T. (2016) “Analysis of effects of shape and location of micro - turbulators on unsteady shockwave - boundary layer interaction in transonic flow,” Proceedings of the VII European Congress on Computational Methods in Applied Sciences and Engineering (ECCOMAS Congress 2016). Available at: https://doi.org/10.7712/100016.1902.12038.

[56] Rogowski, K., Królak, G., Bangga, G. (2021). Numerical Study on the aerodynamic characteristics of the NACA 0018 airfoil at low Reynolds number for Darrieus Wind Turbines using the transition SST model. Processes, 9(3), 477. https://doi.org/10.3390/pr9030477

[57] Sanei, M., & Razaghi, R. (2018). Numerical investigation of three turbulence simulation models for S809 wind turbine airfoil. Proceedings of the Institution of Mechanical Engineers, Part A: Journal of Power and Energy, 232(8), 1037–1048. https://doi.org/10.1177/0957650918767301

[58] Ramsay, R. F., Hoffman, M. J., & Gregorek, G. M. (1995). Effects of Grit Roughness and Pitch Oscillations on the S809 Airfoil. https://doi.org/10.2172/205563

[59] Jonkman, J. M. (2003). Modeling of the UAE Wind Turbine for Refinement of Fast_ad. https://doi.org/10.2172/15005920

APPENDICES

APPENDIX A – S809 Coordinates

45	0	0.009585	-0.08073
44.82914	0.021915	0.047025	-0.15647
44.33355	0.106785	0.05436	-0.16758
43.55298	0.2682	0.10791	-0.23697
42.52829	0.49608	0.419085	-0.51746
41.28696	0.766485	1.04535	-0.91796
39.83819	1.05561	1.9044	-1.36211
38.18048	1.3626	2.964465	-1.83695
36.33615	1.69947	4.20417	-2.33654
34.33689	2.06883	5.584995	-2.83869
32.21784	2.46924	7.094385	-3.31785
30.01788	2.895885	8.71821	-3.76052
27.7799	3.33963	10.43613	-4.15989
25.55235	3.784275	12.21471	-4.49573
23.39244	4.19706	14.03856	-4.73765
21.34094	4.47264	15.90165	-4.86815
19.28075	4.5792	17.78981	-4.8605
17.21754	4.5828	19.72229	-4.70484
15.1767	4.50315	21.6864	-4.38062
13.18365	4.351635	23.75676	-3.8957
11.26112	4.13586	25.9295	-3.32906
9.43092	3.863295	28.17414	-2.72898
7.713405	3.540915	30.45348	-2.13485
6.12783	3.1761	32.7245	-1.5795
4.691835	2.776365	34.93944	-1.08918
3.421575	2.35008	37.04783	-0.68234
2.332035	1.90584	38.99835	-0.36918
1.43595	1.453455	40.74143	-0.15134
0.74655	1.00305	42.23133	-0.02192
0.27117	0.567675	43.42887	0.033435
0.02961	0.167535	44.30151	0.034875
0.00918	0.08739	44.82635	0.01305
0	-0.0009	45	0

APPENDIX B – Experimental Test Matrix

Test Number / Reynolds Number	200.000	300.000	400.000	450.000	500.000	550.000	600.000	650.000	670.000	700.000	750.000
TEST-1.1	Done	Done	Done	-	Done	Done	Done	-	-	-	-
TEST-1.2	Done	Done	Done	Done	Done	Done	Done	-	-	-	-
TEST-1.3	Done	Done	Done	Done	Done	Done	Done	-	-	-	-
TEST-2.1	Done	Done	Done	Done	Done	Done	Done	-	Done	Done	Done
TEST-2.2	-	-	Done	Done	Done	Done	Done	Done	-	Done	Done
TEST-2.3	-	-	Done	Done	Done	Done	Done	Done	-	Done	Done
TEST-2.4	-	-	Done	Done	Done	Done	Done	Done	-	Done	Done
TEST-2.5	-	-	Done	Done	Done	Done	Done	Done	-	Done	Done
TEST-2.1 (repeat)	-	-	Done	Done	Done	Done	Done	Done	-	Done	Done
TEST-2.6	-	-	Done	Done	Done	Done	Done	Done	-	Done	Done
TEST-3.1	-	-	Done	Done	Done	Done	Done	Done	-	Done	Done
TEST-3.2	-	-	Done	Done	Done	Done	Done	Done	-	Done	Done
TEST-3.3	-	-	Done	Done	Done	Done	Done	Done	-	Done	Done
TEST-3.4	-	-	Done	Done	Done	Done	Done	Done	-	Done	Done
TEST-3.5	-	-	Done	Done	Done	Done	Done	Done	-	Done	Done
TEST-3.1 (repeat)	-	-	Done	Done	Done	Done	Done	Done	-	Done	Done

APPENDIX C – Imaging Specifications of FLIR C2 IR Camera

Imaging and Optical Data	
IR sensor	80 × 60 (4,800 measurement pixels)
Thermal Sensitivity	<0.10°C
Field of view	41° × 31°
Minimum focus distance	Thermal: 0.15 m (0.49 ft.) MSX: 1.0 m (3.3 ft.)
Image frequency	9 Hz
Focus	Focus free
Spectral range	7.5–14 µm
3" Display (color)	320 × 240 pixels
Auto orientation	Yes
Touch screen	Yes, capacitive
Image presentation modes	
Thermal image	Yes
Visual image	Yes
MSX	Yes
Gallery	Yes
Measurement	
Object temperature range	–10°C to +150°C (14 to 302°F)
Accuracy	±2°C (±3.6°F) or 2%, whichever is greater, at 25°C (77°F) nominal
Measurement Analysis	
Spotmeter	On/off
Emissivity correction	Yes; matte/semi/glossy + user set
Measurments correction	Reflected apparent temperature Emissivity
Set-up	
Color palettes	Iron, Rainbow, Rainbow HC, Gray
Storage media	Internal memory stores at least 500 sets of images
Image file format	Standard JPEG, 14-bit measurement data included
Video Streaming	
Non-radiometric IR-video streaming	Yes
Visual video streaming	Yes
Digital Camera	
Digital camera	640 × 480 pixels
Digital camera, focus	Fixed focus
Additional Information	
USB, connector type	USB Micro-B: Data transfer to and from PC, iOS and Android
Battery	3.7 V Rechargeable Li-ion polymer battery
Battery operating time	2 h
Charging system	Charged inside the camera
Charging time	1.5 h
External power operation	AC adapter, 90–260 VAC input 5 V output to camera
Power management	Automatic shut-down
Operating temperature range	–10°C to +50°C (14 to 122°F)
Storage temperature range	–40°C to +70°C (–40 to 158°F)
Weight (incl. Battery)	0.13 kg (0.29 lb.)
Size (L × W × H)	125 × 80 × 24 mm (4.9 × 3.1 × 0.94 in.)
System Includes	
Infrared camera Battery (inside camera) Lanyard Power supply/charger with EU, UK, US, CN and Australian plugs Printed Getting Started Guide USB memory stick with documentation USB cable	